

**Expanding the Scope of Thiophene Based Semiconductors:
Perfluoroalkylated Materials and Fused Thienoacenes**

Hayden Thompson Black

A dissertation submitted to the faculty of the University of North Carolina at
Chapel Hill in partial fulfillment of the requirements for the degree of Doctor of
Philosophy in the Department of Chemistry

Chapel Hill
2012

Approved By:

Dr. Valerie Sheares Ashby

Dr. James Cahoon

Dr. Carrie Donley

Dr. Wei You

Dr. Malcolm Forbes

ABSTRACT

HAYDEN THOMPSON BLACK: Expanding the Scope of Thiophene Based Semiconductors: Perfluoroalkylated Materials and Fused thienoacenes
(Under the direction of Valerie Sheares Ashby)

Thiophene based semiconductors with new molecular and macromolecular structures were explored for applications in field effect transistors. Perfluoroalkylation was studied both as a means for controlling the self-assembly properties of polythiophenes, as well as modifying the molecular orbital energies of a series of oligothiophenes. End-perfluoroalkylation of poly(3-hexylthiophene) resulted in interesting self-assembly of the polymer into a bilayer vesicle. Similar fluorophilic assembly may be useful for controlling blend morphologies in heterojunction based devices. On the other hand, perfluoroalkylation of small molecule thiophene semiconductors leads to low lying LUMO levels, and can be used to promote electron injection for n-type transistor devices. This strategy was employed in combination with a π -electron deficient benzothiadiazole to afford a new n-type semiconductor with an exceptionally low LUMO. Monoperfluoroalkylated oligothiophenes were also synthesized and studied in field effect transistors for the first time. In addition, two new fused thienoacene compounds were synthesized and their crystal structures were analyzed. The fused compounds showed exceptional π - π stacking and assembled into well defined one-dimensional microcrystals from the vapor phase. Field effect transistors were fabricated employing the new thienoacenes, showing p-type conductivity with equivalent charge carrier mobilities.

*This dissertation is dedicated to my parents,
for always supporting my endeavors*

ACKNOWLEDGEMENTS

This dissertation would not have been possible without the generous help I received along the way. I would first like to thank my advisor Prof. Valerie Ashby for her support and guidance throughout the years. Her trust in my visions helped make my graduate research a truly wonderful experience. In addition, the Ashby group members helped make the years of research fun and light-hearted.

A number of other people helped make this dream possible. I owe many thanks to Dr. Shubin Liu for his help with density functional calculations throughout the years. I would also like to thank Dr. Peter White for help with x-ray crystallography experiments. I thank Prof. Dmitrii Perepichka at McGill University for accepting me into his laboratory for a collaborative effort focusing on device fabrication of perfluoroalkylated oligothiophenes. It was a pleasure to work with one of his students, Afshin Dadvand, with whom I shared many fruitful discussions.

A large portion of this work was performed within the Chapel Hill Analytical and Nanofabrication Laboratories (CHANL) with help from the wonderful CHANL staff. I owe thanks to Amar Kumbhar for help with SEM and TEM imaging, Bob Geil for help with microfabrication techniques, and Carrie Donley for help with XPS and UPS experiments. Lastly I would like to thank my family and friends for their constant support.

TABLE OF CONTENTS

LIST OF TABLES.....	ix
LIST OF FIGURES.....	x
LIST OF SCHEMES.....	xiii
LIST OF ABBREVIATIONS.....	xiv
LIST OF SYMBOLS	xvi
Chapter 1. An introduction to Organic Semiconductors and Field Effect Transistors	1
1.1 Background	1
1.2 Applications of Organic Field Effect Transistors	2
1.3 OFET Device Fabrication.....	5
1.4 OFET Operation and Electrical Characterization.....	6
1.5 Charge Transport in OFETs.....	8
1.6 Organic Semiconductors Used in OFETs.....	11
1.6.1 Oligomer/Small Molecule Materials	12
1.6.2 Polymeric Materials	18

1.7 Outlook	23
References	25
 Chapter 2. Self-Assembly of Poly(3-hexylthiophene) via End-Group Modification	30
2.1 Introduction	30
2.2 Synthesis	32
2.3 Characterization.....	34
2.4 Thermal Properties	38
2.5 Optical/Electrochemical Properties	40
2.6 Morphological/Self-Assembly Properties.....	41
2.7 Blend Studies	45
2.8 Field Effect Transistor Characterization	48
2.9 Conclusion	50
2.10 Experimental.....	51
References	55
 Chapter 3. Solution Processable Oligothiophenes for Field Effect Transistors.....	57
3.1 Introduction.....	57

3.2 Synthesis and Characterization	58
3.3 Thermal Properties	60
3.4 Optical/Electrochemical Properties	62
3.5 Density Functional Theory Calculations	65
3.6 Morphological Properties	68
3.7 Field Effect Transistor Characterization	72
3.8 Conclusion.....	75
3.9 Experimental.....	76
Appendix	80
References	83
Chapter 4. Tuning Frontier Molecular Orbital Energies via α,ω -Perfluoroalkylation: P-type vs. N-type Conductivity in Perfluoroalkylated Oligothiophenes	85
4.1 Introduction.....	85
4.2 Synthesis	87
4.3 Thermal Properties	89
4.4 Optical Properties	91
4.5 Electrochemical Properties	93
4.6 Density Functional Theory Calculations	95

4.7 Field Effect Transistor Characterization	99
4.8 Conclusion	104
4.9 Experimental	105
Appendix	109
References	114
Chapter 5. Synthesis, Crystal Structures, and Electronic Properties of Nonlinear Fused Thienoacene Semiconductors	116
5.1 Introduction	116
5.2 Synthesis	120
5.3 Crystal Structure Analysis	122
5.4 Optical/Electrochemical Properties	124
5.5 Density Functional Theory Calculations	126
5.6 Thin Film Morphology	127
5.7 Field Effect Transistor Characterization	129
5.8 Conclusion	131
5.9 Experimental	131
Appendix	136
References	142

Chapter 6. Conclusions and Future Work.....	143
6.1 Conclusions	143
6.2 Future Work.....	145
References	148

LIST OF TABLES

2.1 Hole mobilities calculated from the saturation regime (average of ten devices)	48
3.1 Optical /Electrochemical data	64
3.2 Calculated HOMO and LUMO energies.....	67
4.1 Optical properties	93
4.2 Calculated HOMO and LUMO energies.....	97
4.3 Summary of FET device characteristics	99
5.1 Crystallographic data for DTNN and DTNQ	122

LIST OF FIGURES

1.1 Organic active-matrix display on flexible polyester substrate	3
1.2 Bottom-gate OFET devices in top contact (a) and bottom contact (b) geometries	5
1.3 Representative p-type molecular semiconductors	12
1.4 Representative n-type molecular semiconductors	17
1.5 Representative p-type polymeric semiconductors.....	19
1.6 Representative n-type polymeric semiconductors.....	22
2.1 Illustration of semicrystalline morphology of P3HT (top) and the potential morphology of end-substituted P3HT derivatives	31
2.2 MALDI MS spectra of H-P3HT-Br.....	34
2.3 MALDI MS spectra of F-P3HT and 4T-P3HT	35
2.4 Aromatic region of ^1H NMR spectra with end-group peaks (taken in $\text{C}_2\text{D}_2\text{Cl}_4$ at 383 K)	36
2.5 ^{19}F NMR spectrum of F-P3HT (taken in $\text{C}_2\text{D}_2\text{Cl}_4$ at 383 K).....	37
2.6 Polymer GPC traces (THF at 35 $^\circ\text{C}$).....	38
2.7 Second heating thermograms of the polymers (endotherm is down)	39
2.8 UV/vis spectra (left) and oxidative cyclic voltammograms (right) of the polymers.....	41
2.9 Illustration of P3HT lamella with crystallographic indices (left) and an individual P3HT nanowhisker (right)	42

2.10 TEM images of polymer nanowhiskers grown via recrystallization from CH ₂ Cl ₂ (top) and AFM images of spin-cast films from CHCl ₃	43
2.11 TEM images of F-P3HT vesicles dropcast from 0.025 wt% CHCl ₃ solution (a-c) and illustration of bilayer vesicle structure(d).....	44
2.12 TEM image of F-P3HT vesicles showing two vesicles merging	45
2.13 First heating thermograms of α5T and DFH-5T	46
2.14 DSC thermograms of F-P3HT blended with α5T and DFH-5T	47
2.15 Output (left) and transfer (right) characteristics of F-P3HT devices.....	49
2.16 Illustration of potential supramolecular assembly between F-P3HT and a fluorinated fullerene	51
3.1 First heating/cooling DSC thermograms of oligomers (endo is down).....	61
3.2 Polarized optical microscope image of DFH-DD8T at 130 °C	61
3.3 Image of DD8T in THF solution (left) and as powder (right) under 420 nm irradiation.....	62
3.4 UV/vis spectra of the three oligomers in solution (left) and as films (right)	62
3.5 Cyclic voltammograms of DD8T and DFH-DD8T.....	63
3.6 Calculated HOMO geometries for the three oligomers.....	66
3.7 Calculated LUMO geometries for the three oligomers	67
3.8 Powder diffractogram of DD8T	69
3.9 Grazing incidence diffractograms and SEM images of pristine/annealed DD8T films.....	70

3.10 Polarized optical microscope images of DD8T (top) and DFH-DD8T (bottom) as pristine dropcast films (left) and after annealing at 90 °C for 10 min (right). Image c was taken without polarizers crossed.....	71
3.11 Output (left) and transfer (right) characteristics of DD8T devices.....	72
3.12 Transfer characteristics of a fresh DD8T FET and a device stored in air for 30 days.....	73
3.13 Output (left) and transfer (right) characteristics of Bn-DD4T devices	74
4.1 Perfluoroalkylated oligothiophenes incorporating carbonyl functionality.....	86
4.2 Target oligomers studied in this chapter	89
4.3 First heating DSC thermograms of diperfluoroalkylated (left) and monoperfluoroalkylated (right) oligomers.....	90
4.4 Polarized optical images of FH-4T at 230 °C (left) and DFH-4T-BTD at 225 °C (right)	91
4.5 UV/vis spectra of oligomers in THF	92
4.6 Normalized fluorescence spectra in THF	93
4.7 Cyclic voltammograms of thin films of the oligomers	95
4.8 Calculated HOMO and LUMO orbitals for α 5T, FH-5T, and DFH-5T	97
4.9 Calculated HOMO/LUMO orbitals for DFH-5T, 4T-BTD, and DFH-4T-BTD	98
4.10 Energy diagram illustrating the changes in HOMO/ LUMO energies of the oligomers upon chemical substitution	98
4.11 Output (left) and transfer characteristics (right) of 4T-BTD (top) and DFH-4T-BTD (bottom) transistors.....	100
4.12 AFM images of DFH-4T-BTD films grown at room temperature (left) and at 70 °C (right)	101

4.13 AFM image of FH-4T film grown at 50 °C	103
4.14 Output (left) and transfer (right) characteristics of FH-6T transistors.....	103
5.1 Crystal structures and transfer integrals for selected thienoacenes in the literature	117
5.2 Structures and crystal analysis of thienoacene compounds 4 and 5	118
5.3 Crystal structures of tetrathienoacene compounds 6 and 7	119
5.4 Unit cells of DTNN (top) and DTNQ (bottom).....	123
5.5 Herringbone structures of DTNN (top left) and DTNQ (top right) and illustration of δ , P° , and R°	124
5.6 Oxidative cyclic voltammograms (left) and UV/vis spectra in THF solutions (right).....	125
5.7 Calculated frontier molecular orbitals of DTNN and DTNQ	126
5.8 Top: SEM images of DTNN (left) and DTNQ (right) films Lighter regions in top images are the gold source/drain electrodes. Bottom: Illustration of crystal growth along b -axis for DTNQ	128
5.9 Output (top) and transfer (bottom) characteristics of DTNN (left) and DTNQ (right)	130
6.1 Alkylated analog of DTNN for improved solubility	146

LIST OF SCHEMES

2.1 Synthesis of P3HT using the GRIM method	32
2.2 Synthesis of end-functionalized P3HT via post-polymerization Stille coupling	33
3.1 Synthetic route for oligomers DD8T, Bn-DD4T and DFH-DD8T	59
4.1 α,ω -Perfluoroalkylation of quaterthiophene leads to n-type conductivity	86
4.2 Synthesis of oligomers 4T-BTD and DFH-4T-BTD	88
4.3 Synthesis of monoperfluoroalkylated FH-4T and FH-6T	88
5.1 Target thienoacene compounds and retrosynthetic pathway	120
5.2 Synthetic route for compounds DTNN and DTNQ	121
6.1 End-modification of P3HT with red-absorbing chromophore	146

LIST OF ABBREVIATIONS

OFET	Organic field effect transistor
MOSFET	Metal-oxide semiconductor field effect transistor
CMOS	Complementary metal-oxide-semiconductor
RFID	Radio frequency identification
MTR	Multiple trapping and release
P3HT	Poly(3-hexylthiophene)
OTS	Octyltrichlorosilane
SAM	Self-assembled monolayer
HOMO	Highest occupied molecular orbital
LUMO	Lowest unoccupied molecular orbital
OSC	Organic semiconductor
PQT	poly(3,3''-didodecylquaterthiophene)
PBTT	poly(2,5-bis(3-alkylthiophen-2-yl)thieno[3,2- <i>b</i>]thiophene)
PDI	polydispersity index
GRIM	Grignard metathesis
MALDI	Matrix assisted laser desorption ionization
NMR	Nuclear magnetic resonance

GPC	Gel permeation chromatography
DSC	Differential scanning calorimetry
TEM	Transmission electron microscopy
UV/vis	Ultraviolet/visible
AFM	Atomic force microscopy
XRD	X-ray diffraction
SEM	Scanning electron microscopy
POM	Polarized optical microscopy
LC	Liquid crystal
DMF	Dimethylformamide
THF	Tetrahydrofuran
DFT	Density functional theory

LIST OF SYMBOLS

μ	Charge mobility
V_T	Threshold voltage
$I_{\text{on/off}}$	On/off current ratio
δ	Intermolecular spacing
ρ	Density
λ	Wavelength
E_g^{opt}	Optical band-gap
E_g^{CV}	Electrochemical band-gap
Φ_f	Photoluminescence quantum yield

CHAPTER 1

An Introduction to Organic Semiconductors and Field Effect Transistors

1.1 Background

In the 1950s, soon after the development of silicon transistors, German physicist Arthur von Hippel voiced concerns regarding the conventional empirical approach to electronic materials research, and articulated the importance of bottom-up considerations for designing functional electronic materials¹. Through von Hippel and other important researchers the concept of molecular electronics was born, and chemistry was united with electronics research. Later, in the 1960's and 70's, conducting organic polymers such as polypyrrole and polyacetylene were discovered, bringing new meaning to molecular electronics and accelerating research in the field of conducting organic materials. The potential for organic materials to strongly impact the electronics industry has led to a burst of research activity within the field in the past two decades.

For several applications, organic semiconductors provide distinct advantages over conventional inorganic materials. Soluble organic semiconductors enable ink jet printing, an inexpensive patterning technique compatible with high throughput roll to roll processing². This process is easily amenable to fabrication on plastic substrates, enabling flexible electronic technologies³. Other advantages of printed organic circuitry include the low weight and mechanical robustness of such devices. Additionally, from a materials perspective, organic chemistry offers limitless design of materials with unique structures tailored for specific optoelectronic applications.

However, organic semiconductors currently have several drawbacks. Important characteristics of organic electronic devices such as charge carrier mobility, stability, reproducibility, etc. are typically inferior to those employing high performance inorganic semiconductors. For some applications the low cost of organic devices is more important than device performance, and therefore organic semiconductors have become competitive within niche technologies. Organic field effect transistors (OFETs) are a relatively well-developed technology that has seen large improvements in device performance over the past two decades. Today, materials for OFETs are commercially available and many OFET technologies are close to commercialization. The following sections will discuss OFETs in detail, beginning with potential applications and then discussing working principles, device physics, and materials.

1.2 Applications of Organic Field Effect Transistors

Today the most widely used transistor technology for high density applications is the metal-oxide-semiconductor field effect transistor (MOSFET). The MOSFET has become the most popular transistor device due to the low power requirements and ease of incorporation into integrated circuits. Traditional MOSFETs use doped silicon or other inorganics as the semiconductor. Such materials often display high charge carrier mobilities (around 10^2 - 10^3 cm²/Vs)^{4,5}; however, high purity and controlled crystal growth are often necessary for high performance devices, therefore processing conditions can be costly and necessitate high temperatures. For low density applications, for example thin film transistors used in large area displays, amorphous silicon is preferred as a lower performance, lower cost substitute⁶. Today organic semiconductors are in close competition with amorphous silicon for use in large area displays, where transistor size and performance are not as important. Jackson *et al.* recently demonstrated active-

matrix displays utilizing pentacene thin film transistors as switching elements for organic light emitting diodes fabricated on flexible polyester substrates.⁷ Organic displays such as these have received growing interest because of their potential for thin, light-weight, low power, flexible displays. Additionally, organic active-matrix displays such as that pictured in Figure 1.1 possess advantages over similar devices using amorphous silicon

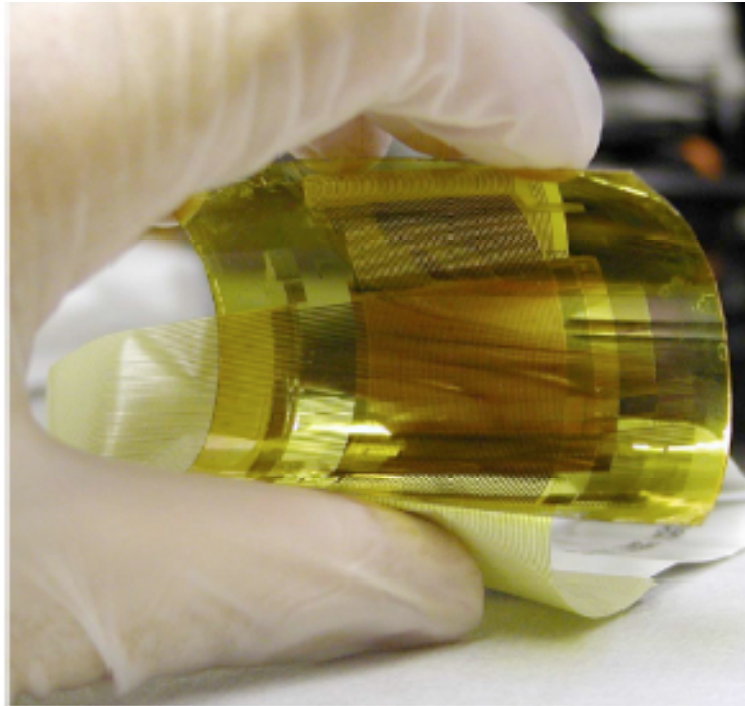


Figure 1.1 Organic active-matrix display on flexible polyester substrate⁷

in that they require lower processing temperatures and may be compatible with high throughput roll-to-roll processing.

OFETs are also important candidates for inexpensive radio frequency identification (RFID) tags that can be used for identification and tracking using radio waves. This technology could provide dramatic improvements in inventory management and checkout/purchasing operations, where an RFID tag would be used as an alternative to a barcode with the advantage of remote communication.⁸ Roll-to-roll

fabrication of RFID technology is expected to provide significant economic advantages over traditional barcode processes; however, the current organic RFID technology is largely limited by operation frequency, which in turn is limited by charge carrier mobility of the employed organic semiconductor. Improvements in semiconductor performance and fabrication techniques will hopefully overcome these current limitations.

The ability to avoid high temperature processing during OFET fabrication has resulted in other creative technologies that employ novel substrates which are otherwise incompatible with traditional transistor technology. For example, OFETs patterned on biodegradable poly(L-lactide-co-glycolide) were recently demonstrated, opening new doors for biocompatible electronics.⁹ Degradation experiments showed that the devices were fully resorbable over a period of 70 days, while maintaining their electrical integrity for the first half of that period. In addition, nature inspired semiconductors such as carotenoids have begun to be studied as the active component in biocompatible OFETs.¹⁰ Biocompatible electronics could bring important advances in biomedical technology such as implantable materials with sensory functions.

While much of the excitement surrounding OFET technologies is based on the use of unique substrates, OFETs may also find future applications in more traditional technologies such as CMOS circuitry. Recently, CMOS-like inverters were constructed using organic semiconductors, demonstrating the possibility for high performance applications of OFETs.^{11,12} Improvements in OFET properties and fabrication/patterning methods will continue to make organic semiconductors more desirable for the electronics industry and open doors for new applications. The following sections will discuss important concepts in the fabrication and operation of OFETs, and will review semiconductor materials used for OFETs to date.

1.3 OFET Device Fabrication

With respect to the source/drain electrodes OFETs can be fabricated in either top contact or bottom contact geometry as shown in Figure 1.2. In both cases the device consists of a gate electrode, an insulating dielectric layer, and a semiconducting layer with source and drain electrode contacts. Most often, heavily doped silicon is used as both the substrate and gate electrode, and the surface oxidized SiO_2 layer acts as the

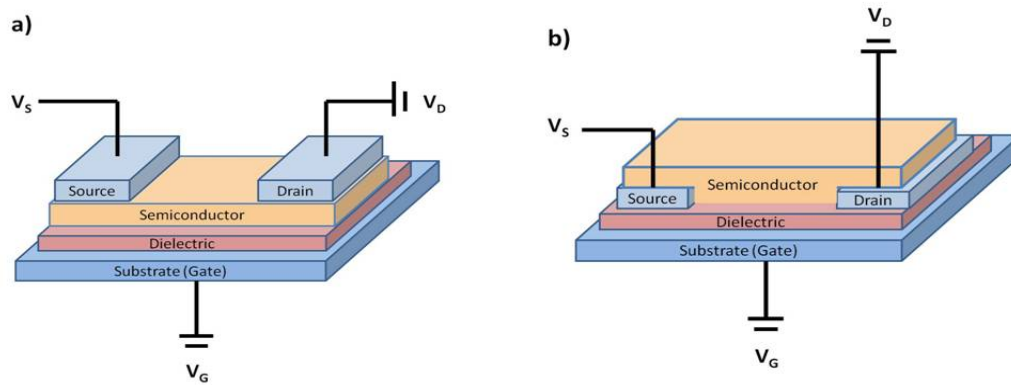


Figure 1.2 Bottom-gate OFET devices in top contact (a) and bottom contact (b) geometries

dielectric. Consistent use of these materials enables device performance comparisons; however, other organic materials are currently under investigation for use as substrate, dielectric, and electrodes in order to realize fully printable, flexible electronics.^{3,13,14,15} Furthermore, while the bottom-gate device geometry shown in Figure 1.2 is more common, devices can also be fabricated in a top-gate configuration.

Top-contact devices (Figure 1.2 a) typically have reduced semiconductor-electrode contact resistance and therefore show improved charge carrier mobility compared to bottom contact devices. However, in this geometry metal electrodes are deposited through a shadow mask, a process which necessitates larger channel lengths (usually greater than $5\ \mu\text{m}$) to prevent shorting.¹⁶ Bottom-contact devices use lithography

to pattern source and drain electrodes directly on top of the dielectric. The organic semiconductor is then deposited either by vacuum sublimation or by solution casting. Using this geometry, semiconductor-electrode contact resistance is usually larger due to difficulties preparing continuous ordered organic films on the non-planar surface.¹⁷ Bottom contact devices are potentially more applicable to large scale fabrication however, and both geometries are still currently reported in the literature.

1.4 OFET Operation and Electrical Characterization

Similar to conventional silicon MOSFETs, organic FETs rely on manipulating charge carriers within the transistor channel in order to control current through the source and drain. The organic semiconductor can behave as an n-type, p-type, or ambipolar charge carrier. When the organic semiconductor is p-type the material is hole transporting, favoring electron extraction from the electrodes. When a negative source-gate voltage is applied to a p-type material, electron extraction will occur at the source electrode allowing a layer of positive charge to form at the semiconductor dielectric interface. This results in a continuous network of charge carriers that bridge the source-drain channel, allowing source-drain current to flow. Thus, the gate electrode acts as a switch to turn source-drain current on and off. When an n-type semiconductor is used electrons are injected under positive gate bias, forming an electron rich layer at the semiconductor-dielectric interface that allows for source-drain current to flow. N-type organic semiconductors have been more elusive than p-type materials, mainly due to the instability of organic anions in the presence of impurities such as oxygen or water.^{16,17} This is a subject that will be discussed further in later sections.

The two most important parameters for OFETs affecting switching speed and amplification are the charge carrier mobility and the I_{on}/I_{off} ratio respectively. The charge carrier mobility represents the average drift velocity per unit electric field and is

expressed by equation 1 where v = drift velocity and F = electric field. Charge carrier mobility can be determined using several techniques such as time-of-flight, diode characterization, pulse-radiolysis time-resolved microwave conductivity, or FET characterization.¹⁸ The most popular method for determining the mobility is by extraction from the current voltage characteristics of an FET. This method is most convenient since it determines the mobility of the semiconductor using working devices. Typically the charge carrier mobility is determined in the saturation regime using equation 2, where I_{SD} = source-drain current, W = channel width, L = channel length, C_i = capacitance of insulator, μ = field-effect mobility, V_G = gate voltage and V_T = threshold voltage.

$$(1) \quad \mu = \frac{v}{F}$$

$$(2) \quad I_{SD} = \frac{W}{2L} \mu C_i (V_G - V_T)^2$$

In order to be acceptable for large area technologies, FETs require charge carrier mobilities $> 0.1 \text{ cm}^2/\text{Vs}$ and an I_{on}/I_{off} ratio $> 10^6$.¹⁹ The threshold voltage, or the gate voltage necessary to turn on the device, should be minimized to limit power consumption. Reported threshold voltages for organic semiconductors have ranged from close to zero volts to as high as 100 volts. Threshold voltage is typically related to the charge injection barrier that results from the energetic difference between source/drain work function and the energy of the semiconductor's conductive orbital. In addition to these commonly assessed parameters, other device characteristics of importance are the processing techniques used, the stability in ambient conditions, the lifetime of the device, and the reproducibility.

1.5 Charge Transport in OFETs

Describing charge transport in organic media has been challenging, and several models have been proposed to elucidate the pertinent mechanisms. For inorganic semiconductors, large crystal lattices comprised of either covalent or ionic bonds lead to largely delocalized electronic states in the solid. Band theory is therefore applicable to inorganic semiconductors and can provide useful insights into charge transport in these materials. On the contrary, organic semiconductors form complex crystal structures comprised of more localized π -conjugated molecular orbitals that are coupled only through relatively weak Van der Waals forces. Furthermore, typical organic films are polycrystalline and thus exhibit disordered regions which are often current-limiting.

Within a single crystal, the rate of electron transfer (hopping) k_{ET} can be described by equation 3.

$$(3) \quad k_{\text{ET}} = \frac{4\pi^2}{h} \frac{1}{\sqrt{4\pi k_{\text{B}}T}} t^2 \exp\left(-\frac{\lambda}{4k_{\text{B}}T}\right)$$

Where λ is the reorganization energy and t is the transfer integral.²⁰ The reorganization energy is related to the relaxation energy of a polaron localized over a single molecule. The transfer integral describes the strength of interaction between two nearest neighbors within a crystal, and is intimately related to the crystal structure as well as the molecular orbital geometry. While equation 3 is useful for modeling transport within pure single crystals, devices often employ thin films with disorder and charge traps (impurities) and therefore require models that take these defects into account.

Among prominent theoretical work, transport in organic thin films has been modeled through delocalized states²¹, variable-range hopping²², Holstein's theory of small polaron motion²³, and multiple trapping and release (MTR).^{24,25,26} The MTR model

has been successfully applied to amorphous silicon, and has emerged as one of the most accepted models for charge transport in organic semiconductors. The MTR model describes the restriction of charge transport in the conduction band of an organic semiconductor by lower lying energy traps, and thermal release from these traps. The charge trap energy distribution and density therefore affect the charge carrier mobility. This model emphasizes the importance of purity for organic semiconductors, as small amounts of impurities can lead to detrimental charge trapping. The following expression describes the effective mobility μ_{eff} relative to the free carrier mobility μ_0 , in the presence of traps. Here E_C is the energy of the conduction band, E_T the trap energy and E_A the activation energy.

$$4) \quad \mu_{eff} = \mu_0 \exp\left(\frac{-(E_C - E_T)}{kT}\right) = \mu_0 \alpha \exp\left(\frac{-(E_A)}{kT}\right)$$

By plotting the $\log(\mu_{eff})$ vs. $1/T$ the activation energy can be calculated from the slope using equation 4. It should be noted that the MTR model is applicable only to charge transport in polycrystalline films, the most common morphology studied in OFETs. Different morphologies require different models, for example, band-like transport has been experimentally observed for single crystal devices.²⁷

Several experimental studies have discovered charge transport anisotropy in both small molecule and polymer organic semiconductors. This behavior can arise from intrinsic transport anisotropy in single crystals^{28, 29, 30} as well as from anisotropic grain boundaries with differing activation energies.^{31,32} X-ray diffraction studies combined with FET analysis on single crystals have demonstrated that intrinsic charge transport in both small molecules and polymers is typically most efficient in the direction of cofacial intermolecular π - π stacking. This is due to the increased overlap of frontier orbital

wavefunctions along this path. In contrast, when the transport properties of directionally oriented polycrystalline films of poly(3-hexylthiophene) (P3HT) were analyzed the results showed that transport was most efficient in the direction parallel to the polymer backbone.³² In this case, grain boundary anisotropy was the determining factor affecting transport efficiency. Grain boundary effects will receive more attention in chapter 2.

Charge transport through an OFET is also highly dependent on the chemistry and physics of the device interfaces. The first interface of importance is that of the semiconductor-electrode (source/drain). In an ideal OFET the semiconductor will form an ohmic contact with the metal electrodes, resulting in linear I-V characteristics. However, forming ohmic contacts at the metal-semiconductor interface is not always trivial. It is generally believed that top-contact devices lead to more intimate semiconductor-electrode contacts that display desirable ohmic behavior, though this can be material dependent.³³

The second important interface is that of the semiconductor-dielectric. Since transport occurs within only $\approx 1\text{-}2$ nm of the semiconductor-dielectric interface³⁴, the observed mobility in OFET's is largely dependent on the energetics of this interface along with the morphology of the semiconductor close to the dielectric. Presence of SiOH groups and other impurities at the SiO_x surface have been found to negatively affect transport by creating charge traps. These problems are now avoided by extensive cleaning of the SiO_x surface followed by formation of a self-assembled monolayer (SAM) on the surface. Typical SAMs used for modifying the silicon oxide surface in OFET's are hexamethyldisilazane and octyltrichlorosilane (OTS). These compounds react with SiOH groups on the SiO_x surface, forming a dense array of surface-grafted insulating alkyl chains. This process carries two purposes; first, the functionalized surface masks the charge trapping SiOH groups, and second, the alkyl functionalized surface can lead to molecular ordering of the organic semiconductor that is more ideal for charge transport.

For example Kline *et al.* showed that for OFET's employing P3HT as semiconductor, treatment of the SiO_x surface with OTS results in P3HT orientation with both the polymer backbone and π - π stacking in the plane of the substrate, leading to higher mobilities.³⁵ Today, SAM formation at the dielectric surface is a common procedure in the preparation of OFET's.

1.6 Organic Semiconductors Used in OFETs

Materials used for OFETs can be divided into two categories, those that are vacuum deposited and those that are solution processed. Vacuum deposition is a processing method that is expensive and can require high temperatures, and is therefore not economically preferential for organic electronics. However, vacuum deposition can afford increased control over important thin film parameters such as film thickness and crystal grain size and can therefore be advantageous for studying fundamental aspects of organic electronic devices. Materials that require vacuum deposition are those that are not soluble in common organic solvents due to molecular rigidity and strong π -orbital interactions. In contrast to these materials, soluble organic compounds can be solution cast onto devices, a low cost processing technique which is the crux of organic electronics. These materials incorporate solubilizing groups that typically result in slightly lower OFET performance due to reduced π - π interactions.

In addition to these categories organic semiconductors can also be classified as p-type, n-type, or ambipolar based on their ability to transport holes, electrons, or both, respectively. This section will first discuss small molecule organic semiconductors, separated by charge carrier type. Polymeric materials will then be addressed, again divided into charge carrier type.

1.6.1 Oligomer/Small Molecule Materials

P-Type Materials

Small molecule semiconductors have been employed since the earliest studies of OFETs. In the field of p-type materials, acenes are among the top performing organic

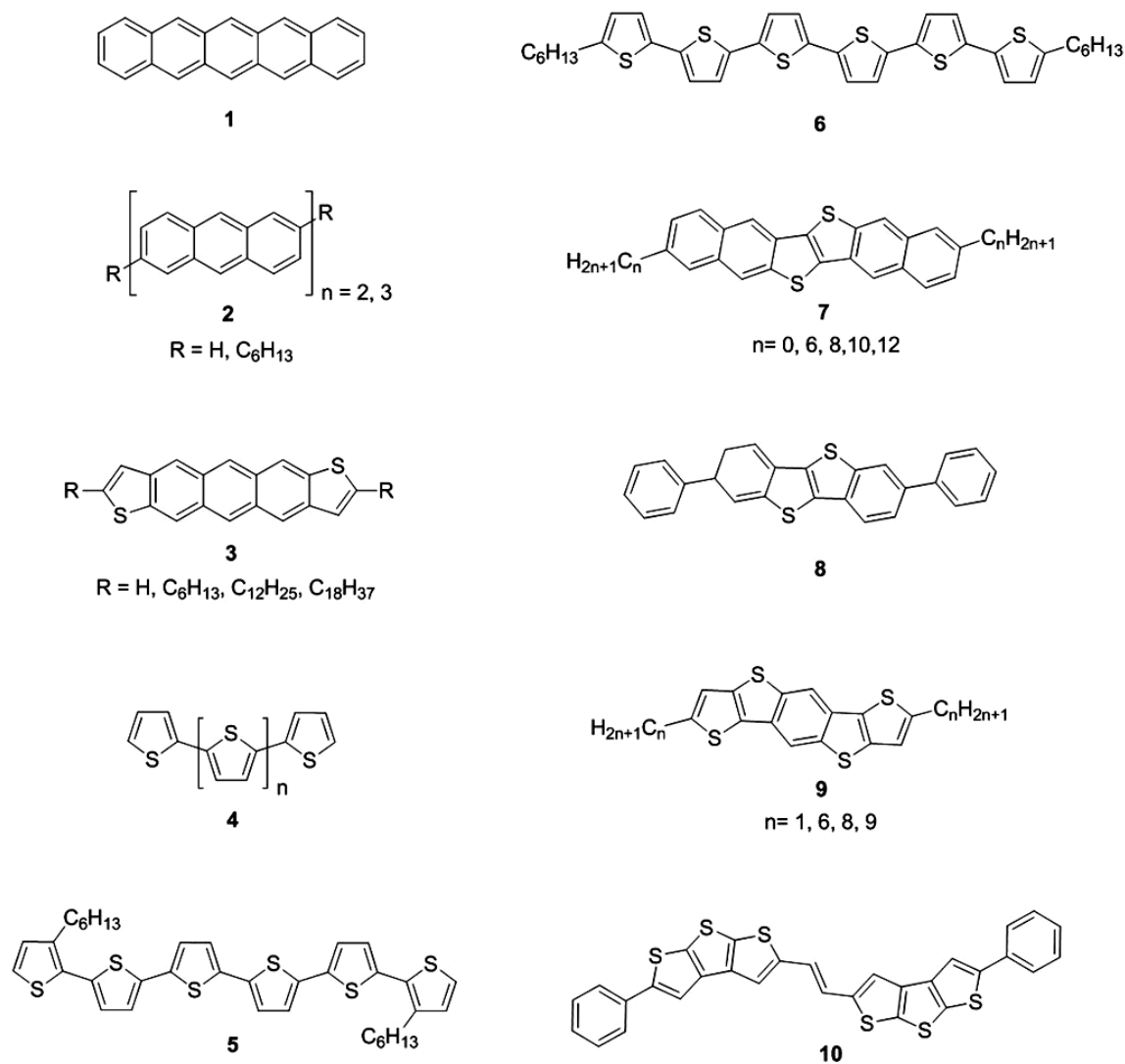


Figure 1.3 Representative p-type molecular semiconductors

semiconductors in terms of charge mobility and on/off current. Very high hole mobilities of greater than $40.0 \text{ cm}^2/\text{Vs}$ with $I_{\text{on}}/I_{\text{off}}$ of 10^6 have been reported for single crystals of pentacene¹⁶ (**1**, Figure 1.3), one of the earliest studied acene semiconductors. The superior electronic properties of pentacene have been attributed to its extended π -orbital system with good π - π overlap in the solid state. For these reasons pentacene is still a common OFET performance standard used for comparison with newly developed materials. A common problem with highly conjugated fused aromatic rings such as pentacene is that the compounds are often relatively unstable toward oxidation as a result of high lying HOMO energies. This can sometimes be avoided by proper encapsulation of the device. A unique solution to this problem was developed by Ito *et al.* who designed a series of linked anthracene units in order to obtain highly conjugated structures similar to pentacene while avoiding the instability issues associated with the fused ring system (**2**, Figure 1.3).³⁶

In 1998, Laquindanum *et al.* synthesized a new class of anthradithiophenes and studied their OFET behavior.³⁷ All of the synthesized compounds showed p-type transport behavior, with relatively high field effect mobilities (0.06 - $0.15 \text{ cm}^2/\text{Vs}$). The dihexyl and didodecyl analogs (**3** Figure 1.3) showed the highest mobilities which was attributed to the better interconnectivity of crystalline grains in their thin films. All of the anthradithiophenes synthesized were mixtures of syn and anti isomers, a synthetic challenge that most likely had negative effects on device morphology and performance.

Another important class of insoluble p-type materials are oligothiophenes. Beginning in the early 1990's α -sexithiophene (**4**, $n=4$, Figure 1.3) was investigated for use in OFET's, showing hole mobilities up to $0.03 \text{ cm}^2/\text{Vs}$.^{38,39,40} This sparked increased interest in oligothiophene based materials resulting in wide synthetic efforts for new oligothiophene semiconductors. Unsubstituted oligothiophenes of varying length have been synthesized and show similar crystal structures defined by a herringbone packing

motif common to many conjugated oligomers.⁴¹ These compounds also exhibit similar hole mobilities that are highly dependent on oligomer purity as well as processing conditions.¹⁶ For example, heating the substrate during evaporation of α -octathiophene had dramatic effects on the semiconductor microstructure leading to greatly improved hole mobility of $0.33 \text{ cm}^2/\text{Vs}$.⁴² The dependence of hole mobility on processing conditions in these materials emphasizes the importance of thin film morphology on charge transport in organic solids.

Substituted oligothiophenes have also been synthesized in order to improve either the solubility or the solid-state ordering.⁴³ Generally, substitution of oligothiophenes at the β position decreases intermolecular interactions and increases solubility due to decreased conjugation of the backbone as a result of steric hindrance. For example, β -hexyl substituted α -sexithiophene (**5**, Figure 1.3) showed increased solubility and a lower melting point than the parent sexithiophene. However, this had no effect on the hole mobility of top contact transistors prepared via vacuum sublimation of **5**.⁴⁴ On the other hand, substitution at the α position (**6**, Figure 1.3) typically has little effect on solubility, but can lead to improved mesoscale ordering and higher mobilities.⁴⁵
⁴⁶ Many other substituted oligothiophenes showing p-type behavior have been synthesized and studied; however, the more simple structures of α -sexithiophene and α,ω -dihexylsexithiophene continue to outperform most others.

More recently several fused aromatic heterocycles were synthesized which showed very good FET properties (**7-10** Figure 1.3). Fused aromatic compounds **7-10** all exhibited air stable OFET performance, with mobilities of $2.0 \text{ cm}^2/\text{Vs}$ or greater.^{47,48,49,50,51} Alkylation of compound **7** was found to improve structural order, and afforded polycrystalline OFETs with hole mobilities as high as $7.9 \text{ cm}^2/\text{Vs}$.⁴⁸ The improved stability of these fused systems arises from their non-linear π -systems, which reduces aromaticity and lowers the HOMO energy.⁴⁷ The high charge mobilities and air

stability of fused thienoacene compounds has brought this class of materials to the forefront of small molecule OEFT research.

N-Type Materials

In theory, all organic semiconductors should exhibit both p-type and n-type transport, where the majority carrier should depend primarily on the work function of the electrodes and the applied potentials during operation. However, electron transport in organic semiconductors is rare in comparison to the more commonly observed p-type behavior. Work done by Chua *et al.* revealed that charge trap sites at the dielectric surface play a large role in electron transport quenching.⁵² Methods for masking surface charge traps, such as formation of SAMs, are therefore beneficial for efficient electron transport. Nevertheless the amount of n-type OSCs in literature remains low compared to p-type materials. This is primarily due to more efficient charge trapping in n-channel OFETs from environmental impurities such as water and oxygen. Compounds with high electron affinity generally show better performance in n-type OFETs due to stabilized LUMO levels which promote electron injection and lie energetically below charge trap sites. Many research groups have therefore focused on the design and synthesis of OSCs with low lying LUMO levels. The most common method for achieving low lying LUMO levels in conjugated organic materials is to incorporate electron withdrawing units directly onto the π -conjugated system. Typically, materials with LUMO levels below -3.2 eV are good candidates for n-channel organic semiconductors. Several materials used in n-channel OFETs are shown in Figure 1.4.

One of the earliest studied n-type organic semiconductors was tetracyanoquinodimethane (**11**, Figure 1.4). While this compound exhibited relatively low electron mobilities, the on/off current was found to increase over time, unlike most p-type semiconductors.⁵³ A cyano substituted quinoidal terthiophene based compound (**15**,

Figure 1.4) showed high electron mobilities up to 0.2 cm²/Vs with I_{on}/I_{off} ratios of 10⁵. This compound was also one of the first to exhibit ambipolar charge transport, albeit with low charge mobilities.⁵⁴ Both of these quinoidal compounds benefited from incorporation of the strong electron withdrawing cyano groups, which stabilized the LUMO and allowed electron transport in OFETs.

Perfluoroalkyl groups are another class of electron withdrawing substituents that have been successfully incorporated into conjugated organics, resulting in increased electron affinity and efficient electron transport. Facchetti *et al.* synthesized a large library of perfluorohexyl substituted oligothiophenes with varying π -conjugated core length and substituent regiochemistry. The highest electron mobilities were observed for α,ω -diperfluorohexyl substituted quaterthiophene (**12**, Figure 1.4), with a maximum electron mobility of 0.22 cm²/Vs and I_{on}/I_{off} ratios of 10⁶ in optimized devices.^{44,55} Several trifluoromethyl substituted conjugated oligomers have also been prepared and have shown high electron mobilities. Compound **16** incorporating thiazole units into the conjugated backbone exhibited very high electron mobility of 1.83 cm²/Vs with an I_{on}/I_{off} ratio of 10⁴, though exhibited a very high threshold voltage of 78 V.⁵⁶

Recently, π -deficient pentacenequinones were synthesized and showed good electron transport in n-channel FETs.⁵⁷ All of the pentacenequinones studied showed crystal structures with face-to-face π - π stacking, a packing motif which is believed to promote frontier molecular orbital overlap and could aid in charge transport. The *N*-heteropentacenequinone **13** had a very low lying LUMO at -3.78 eV and afforded FETs with electron mobility as high as 0.12 cm²/Vs. Compound **17** also showed a reduction in LUMO compared to the unsubstituted 6,13-pentacenequinone, and gave electron mobilities up to 0.18 cm²/Vs.

More recently naphthalene and perylene diimides have come to the forefront of n-type semiconductors. These compounds consist of a highly fused aromatic system

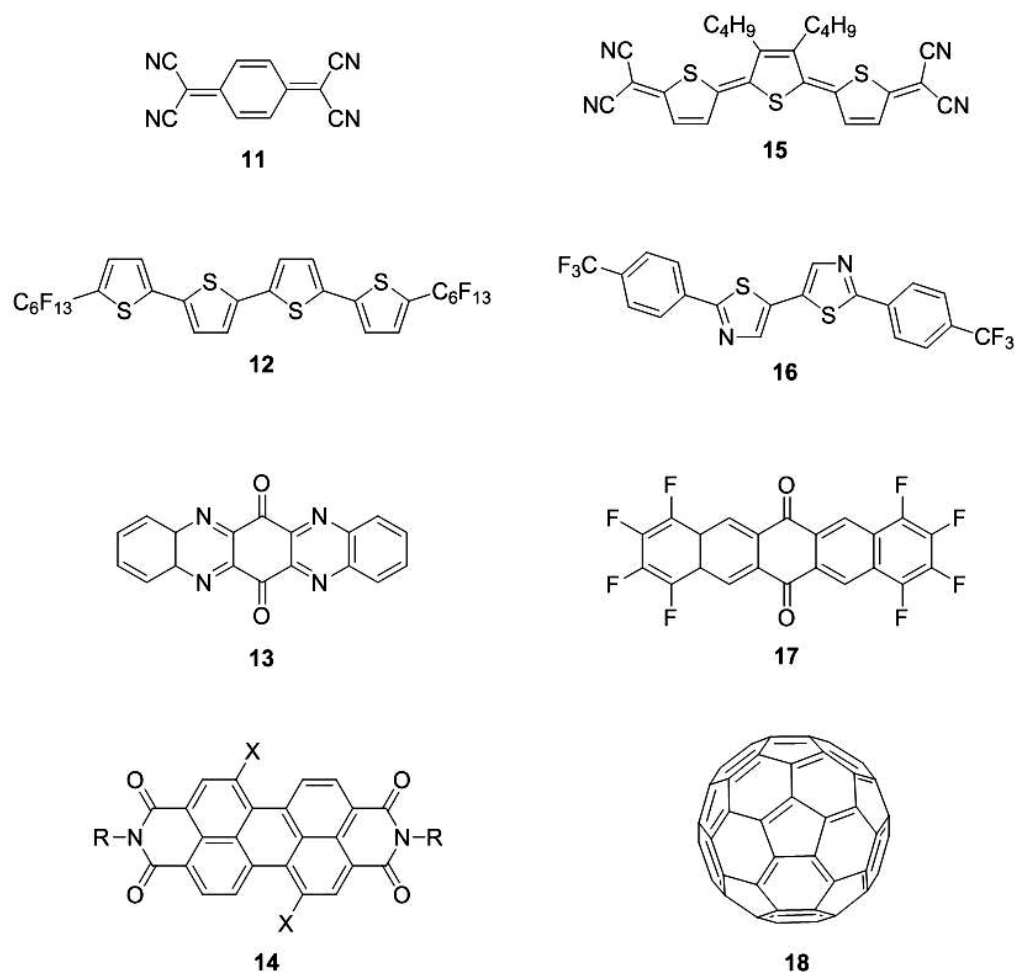


Figure 1.4 Representative n-type molecular semiconductors

incorporating the strong electron withdrawing diimide group. The general structure of a perylene diimide is shown in Figure 1.4 (compound **14**). Very high electron mobilities up to $0.64 \text{ cm}^2/\text{Vs}$ were recently reported for core cyanated perylene diimides ($X = \text{CN}$) with N-perfluoroalkyl chains ($R = \text{CH}_2\text{C}_3\text{F}_7$)^{58,59,60} In this case the cyano group reduced the LUMO level while the perfluoroalkyl group led to tighter packing and better π - π overlap in the solid state.

Fullerene compounds (**18**, Figure 1.4) possess low lying LUMO levels around -3.7 eV as a result of their highly conjugated spherical structure, and have thus been widely used as n-type semiconductors for various electronic applications. The most common

application of fullerenes is in organic solar cells, though fullerenes have been used for OFETs as well. Functionalized fullerenes were used for solution processed n-channel OFETs, giving electron mobilities up to $0.078 \text{ cm}^2/\text{Vs}$.⁶¹ Perfluoroalkyl substituted fullerenes have also been studied in n-channel OFETs, and showed electron mobilities up to $0.067 \text{ cm}^2/\text{Vs}$.⁶²

1.6.2 Polymeric Materials

P-Type Materials

Compared to molecular semiconductors, polymeric materials offer an alternative with both advantages and disadvantages. In general, the synthesis and purification of conjugated polymers is less cumbersome than for small molecules, an important aspect for practical applications of organic semiconductors. In addition, polymers are too heavy to be evaporated and thus typically incorporate solubilizing groups which enable solution processing. However, while conjugated small molecules are often highly crystalline, dispersity of the chain length in conjugated polymer samples results in semicrystalline thin films with reduced order. This property of polymeric semiconductors prevents growth of single crystals and therefore limits their electrical properties in OFETs. Polydispersity does however have the advantage of better morphological reproducibility and often greater device stability.

Early investigations of conjugated polymers dating to the early 1980's relied on electrochemical preparations of conductive thin films.^{63,64} These experiments attracted much attention to the field of conjugated polymers; however, the insoluble products of electrochemical synthesis limited the possible experiments and applications of the materials. To increase processability of conjugated polymers, new monomers incorporating solubilizing groups, often alkyl chains, were synthesized and polymerized. Over the past three decades thousands of conjugated polymers have been synthesized

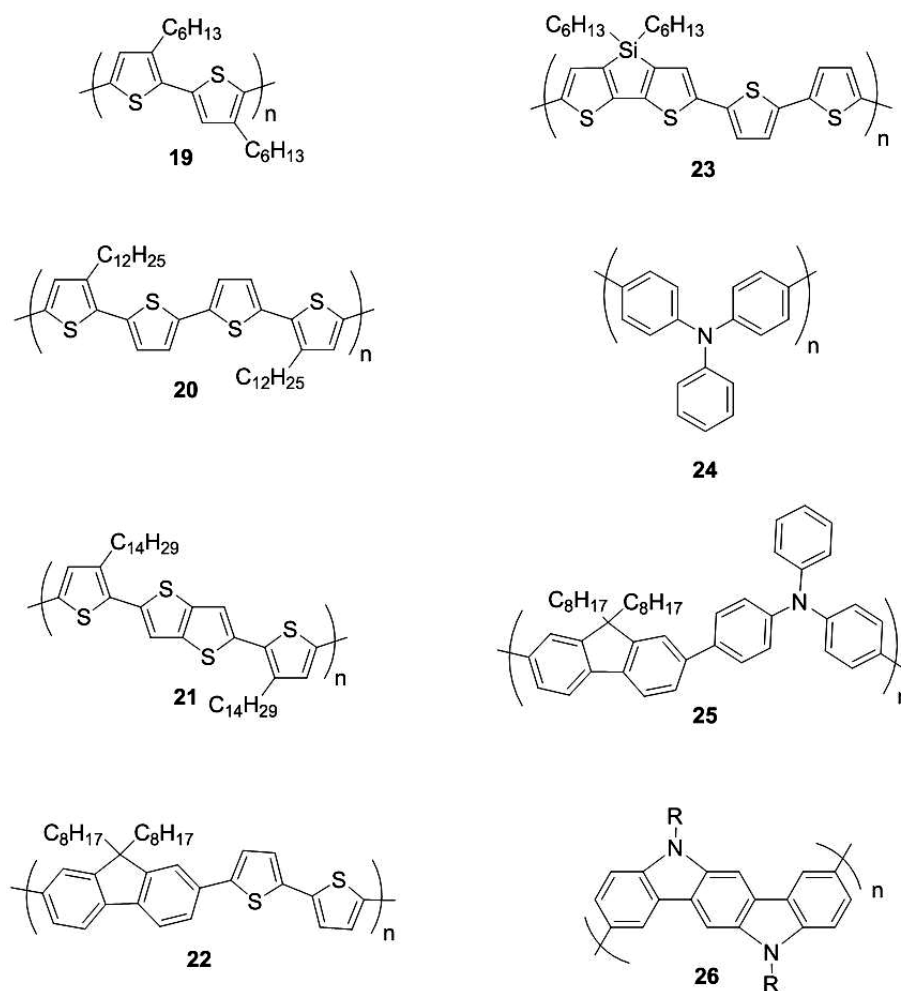


Figure 1.5 Representative p-type polymeric semiconductors

with steady improvements in critical material properties such as solubility, optical properties, MO energetics, stability, morphology, etc. To date, the majority of conjugated polymers used in OFETs have been p-type semiconductors. Several p-type conjugated polymers exhibiting good OFET performance are shown in Figure 1.5. Poly(3-hexylthiophene) (P3HT, **19**, Figure 1.5) is one of the most widely studied conjugated polymers for use in both OFETs and photovoltaics due to its refined synthesis, good solubility, and hole mobility around $0.1 \text{ cm}^2/\text{Vs}$.^{65,66,67,68} The hexyl chain of P3HT endows good solubility of the polymer in solvents such as chloroform, tetrahydrofuran, and

halogenated benzenes. Regioregularity of P3HT has been shown to have significant effects on thin film morphology and charge transport,⁶⁹ and structural regularity is now an important consideration in the design of conjugated polymers in general. Today regioregular head-to-tail P3HT (**19**, Figure 1.5) is the most commonly used form of P3HT.

A related material, poly(3,3''-didodecylquaterthiophene) (PQT, **20**, Figure 1.5) which utilized dodecyl chains for solubility was synthesized by Ong *et al.* in 2004.⁷⁰ Polymer PQT incorporates one alkyl chain for every two thiophene rings, while using longer dodecyl chains to maintain solubility of the polymer. This led to a mesophase for PQT between ~120-140 °C which could be used for increasing order in films of the conjugated polymer. In addition, the reduced number of electron donating alkyl chains along the polymer backbone led to a more stable HOMO level which led to increased ambient stability of FET devices using PQT compared to P3HT. Transistors fabricated using PQT gave hole mobilities up to 0.14 cm²/Vs.

A similar polymer incorporating a fused thieno[3,2-*b*]thiophene repeat unit (**21**, Figure 1.5) also exhibited a liquid crystalline phase and afforded OFETs with mobility as high as 0.6 cm²/Vs after annealing through the mesophase.⁷¹

Conjugated materials incorporating fluorene units have been widely used in light emitting devices as well as transistors.^{72,73} Polyfluorenes typically exhibit larger band-gaps than polythiophenes and often possess better solubility due to reduced planarity of the conjugated backbone and because of the sp³ bridge on the fluorene unit. A representative example of hole transporting polyfluorenes is shown in Figure 1.5 (**22**) which showed hole mobilities of 0.02 cm²/Vs in transistors after optimization of the dielectric material.⁷⁴

Semiconducting polymers incorporating silole groups have also been investigated for use in OFETs. Silole groups that formed bridges between conjugated

biphenyl or bithiophene repeat units were studied, where silicon-bound alkyl chains were utilized for solubility. Experiment and theory both showed an increase in both ionization potential and electron affinity for polymers incorporating the silole groups, leading to greater ambient stability of OFETs. Polymer **23** (Figure 1.5) showed high hole mobilities of up to $0.08 \text{ cm}^2/\text{Vs}$ after annealing the film at 250°C under N_2 .⁷⁵

Triarylamine (TA) units are electron rich and have thus found use in donor-acceptor polymers for photovoltaics and in p-channel OFETs.^{74,76} The triarylamine unit deviates from planarity which leads to increased solubility and reduced crystallinity of TA incorporating materials. Polytriarylamine **24** was utilized as an amorphous semiconductor for p-channel OFETs, giving hole mobilities around $0.01 \text{ cm}^2/\text{Vs}$.⁷⁴ Amorphous semiconductors are an interesting alternative to crystalline materials because of their isotropic morphology and thus more reproducible electrical properties; however, such materials typically afford lower charge mobilities in OFETs due to reduced intermolecular interactions. The hole mobility of polymer **25** incorporating electron rich fluorene and triarylamine units was analyzed via time of flight measurements showing mobilities around $10^{-3} \text{ cm}^2/\text{Vs}$.⁷⁷ Carbazole units, similar to triarylamine materials, are electron rich and have been incorporated into many different conjugated polymers. Polymer **26** was investigated for use in OFETs, and showed hole mobilities up to $0.02 \text{ cm}^2/\text{Vs}$.⁷⁸ The material was found to exhibit moderate crystallinity and showed ambient FET stability due to a relatively low HOMO level around -5.2 eV . to exhibit moderate crystallinity and showed ambient FET stability due to a relatively low HOMO level around -5.2 eV .

N-Type Materials

Compared to p-type polymers, far less conjugated polymers have been found to perform as n-channel semiconductors. Ground breaking work done by Chua *et al.*

demonstrated that many conjugated polymers typically used for p-channel OFETs were able to act as n-type materials after appropriate surface treatment of the dielectric. This was explained by the presence of electron trapping silanol sites at the surface of the commonly employed SiO₂ dielectric which must be masked in order to avoid electron trapping during OFET operation. N-channel devices were even fabricated using P3HT which showed an electron mobility of $6 \times 10^{-4} \text{ cm}^2/\text{Vs}$.⁵² However, all of the materials tested gave electron mobilities below $0.01 \text{ cm}^2/\text{Vs}$, and in some cases the FET devices were not stable.

Low lying LUMO levels are desirable for n-channel OFETs in order to improve electron injection and to prevent charge transfer from polymer to low lying trap sites. Thus, strong electron withdrawing substituents have been employed for the synthesis of some n-type conjugated polymers. In addition, optimized materials for n-channel OFETs should exhibit good crystallinity with significant molecular orbital overlap in the solid state in order to produce efficient charge percolation networks. The three most notable n-type polymeric semiconductors are depicted in Figure 1.6. Ladder type polymer **27** was

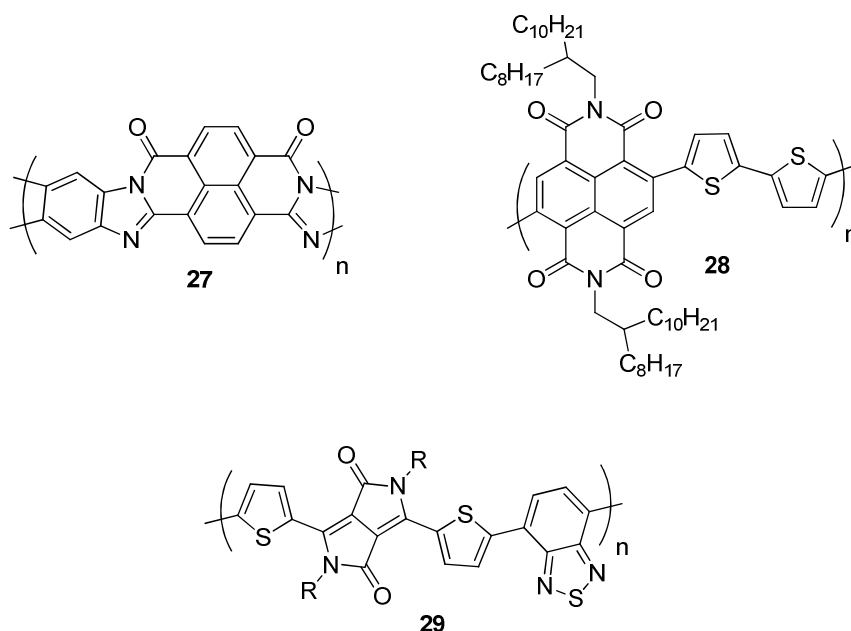


Figure 1.6 Representative n-type polymeric semiconductors

synthesized by Babel *et al.* and showed electron mobility as high as $0.1 \text{ cm}^2/\text{Vs}$ during OFET operation.⁷⁹ Polymer **27** benefited from a very low LUMO around 4.0 eV ⁸⁰ and good crystallinity when cast from methanesulfonic acid solutions. Interestingly, a very similar polymer without the ladder-type structure showed reduced crystallinity and very low electron mobility while possessing an equivalent LUMO level. Thus the ladder-type structure of **27** was believed to afford an optimal morphology with good π - π stacking. More recently, Yan *et al.* synthesized polymer **28** incorporating a naphthalene diimide into the polymer backbone, affording a novel n-type polymer with a LUMO of circa 4.0 eV .⁸¹ N-channel OFETs fabricated in a top-gate bottom-contact geometry showed electron mobilities as high as $0.85 \text{ cm}^2/\text{Vs}$ under ambient conditions. Furthermore, devices were found to be stable for more than 20 weeks under ambient conditions. Polymer **28** was also used in combination with P3HT to form complementary inverters which showed voltage gains of up to 60, demonstrating the potential for the material to be used in functional logic circuits.

Poly(diketopyrrolopyrrole-benzothiadiazole) **29** was found to exhibit ambipolar FET characteristics with well balanced hole and electron mobilities close to $0.1 \text{ cm}^2/\text{Vs}$.⁸² This was the first example of an ambipolar polymer with well matched charge mobilities. The polymer exhibited a low band gap of only 1.2 eV , leading to low injection barriers for both holes and electrons.

1.7 Outlook

The performance of organic semiconductors has improved tremendously over the past few decades; however, there are still challenges that require new materials and processing methods in order to fully realize the capabilities of organic electronics. One of the most important ongoing issues is morphology control. The morphology of organic semiconductors is intimately linked to the molecular structure as well as the processing

methods used for film deposition. Film morphology can have significant affects on charge mobility and is thus extremely important for optimizing field effect transistors. For small molecules, finding methods that allow for controlled crystallization in a low cost, high-throughput manner are sought after.^{31,83} Furthermore, materials which are both highly soluble and highly crystallizable are of interest. Similarly, for polymers finding processing methods that can alleviate the negative effects of grain boundaries are desirable. This often relies on materials which exhibit ordering on the mesoscale, for example liquid-crystalline conjugated polymers.⁷¹

Finding materials that exhibit a combination of desirable properties is an ongoing quest. The ideal organic semiconductor for field effect transistors should be ambipolar, exhibit stable device operation in air, have high charge mobilities and a low threshold voltage. The discovery of such materials requires fine tuning of the molecular structure in order to control orbital energies, π - π communication, and film forming ability. Further understanding of structure property relationships within organic semiconductors will lead the way to better molecular design and improved device performance.

References

- 1) Choi, H.; Mody, C. C. M. *Soc. Stud. Sci.* **2009**, 39, 11
- 2) Sirringhaus, H.; Kawase, T.; Friend, R. H.; Shimoda, T.; Inbasekaran, M.; Wu, W.; Woo, E. P. *Science* **2000**, 290, 2123
- 3) Kim, T.; Son, S. J.; Seo, S. *Appl. Phys. Lett.* **2008**, 93, 013304
- 4) Kim, J. I.; Choi, J. W.; Choi, W.; Mativenga, M.; Jang, J.; Williams, C. K.; Wang, C. C.; Mozdy, E.; Cites, J.; Lai, J.; Tredwell, T. J. *Solid State Electron.* **2010**, 54, 299
- 5) Thomas, S. M.; Whall, T. E.; Parker, E. H. C.; Leadley, D. R.; Lander, R. J. P.; Vellianitis, G.; Watling, J. R.; *Solid State Electron.* **2009**, 53, 1252
- 6) Shah, A.; Meier, J.; Buechel, A.; Kroll, U.; Steinhauser, J.; Meillaud, F.; Schade, H.; Dominé, D. *Thin Solid Films* **2006**, 502, 292
- 7) Zhou, L.; Wanga, A.; Wu, S.-C.; Sun, J.; Park, S.; Jackson, T. N. *Appl. Phys. Lett.* **2006**, 88, 083502
- 8) Subramanian, V.; Fréchet, J. M. J.; Chang, P. C.; Huang, D. C.; Lee, J. B.; Molesa, S. E.; Murphy, A. R.; Redinger, D. R.; Volkman, S. K. *Proc. IEEE* **2005**, 93, 1330
- 9) Bettinger, C. J.; Bao, Z. *Adv. Mater.* **2010**, 22, 651
- 10) Irimia-Vladu, M.; Sariciftci, N. S.; Bauer, S. *J. Mater. Chem.* doi: 10.1039/c0jm02444a
- 11) Meijer, E. J.; De Leeuw, D. M.; Setayesh, S.; Veenendaal, E. V.; Huisman, B.-H.; Blom, P. W. M.; Hummelen, J. C.; Scherf, U.; Klapwijk, T. M. *Nat. Mater.* **2003**, 2, 678
- 12) Walser, M. P.; Kalb, W. L.; Mathis, T.; Brenner, T. J.; Batlogg, B. *Appl. Phys. Lett.* **2009**, 94, 053303
- 13) Li, L.; Hirtz, M.; Wang, W.; Du, C.; Fuchs, H.; Chi, L. *Ad. Mater.* **2010**, 22, 1374
- 14) Cho, J. H.; Lee, J.; Xia, Y.; Kim, B.; He, Y.; Renn, M. J.; Lodge T. P.; Frisbie, C. D. *Nat. Mater.* **2008**, 7, 900
- 15) Lee, S. W.; Lee, H. J.; Choi, J. H.; Koh, W. G.; Myoung, J. M.; Hur, J. H.; Park, J. J.; Cho, J. H.; Jeong, U. *Nano Lett.* **2010**, 10, 347
- 16) Jurchescu, O. A.; Popinciuc, M.; van Wees, B. J.; Palstra, T. T. M. *Adv. Mater.* **2007**, 19, 688
- 17) Dimitrakopoulos, C. D.; Malenfant, P. R. L. *Adv. Mater.* **2002**, 14, 99

- 18) Coropceanu, V.; Cornil, J.; da Silva Filho, D. A.; Olivier, Y.; Silbey, R.; Brédas, J. *Chem. Rev.* **2007**, 107, 926
- 19) Katz, H. E.; Bao, Z. *J. Phys. Chem. B* **2000**, 104, 671
- 20) Brédas, J. L.; Calbert, J. P.; da Silva Filho, D. A.; Cornil, J. *Proc. Natl. Acad. Sci.* **2002**, 99, 5804
- 21) Koh, S. E.; Delley, B.; Medvedeva, J. E.; Facchetti, A.; Freeman, A. J.; Marks, T. J.; Ratner, M. A. *J. Phys. Chem. B* **2006**, 110, 24361
- 22) Vissenberg, M. C. J. M.; Matters, M. *Phys. Rev.* **1998**, 57, 12964
- 23) Torsi, L.; Dodabalapur, A.; Rothberg, L. J.; Fung, A. W. P.; Katz, H. E. *Science* **1996**, 272, 1462
- 24) Letizia, J. A.; Rivnay, J.; Facchetti, A.; Ratner, M. A.; Marks, T. J. *Adv. Funct. Mater.* **2010**, 20, 50
- 25) Horowitz, G. *Adv. Mater.* **1998**, 10, 365
- 26) Le Comber, P. G.; Spear, W. E. *Phys. Rev. Lett.* **1970**, 25, 509
- 27) Liu, C.; Minari, T.; Lu, X.; Kumatani, A.; Takimiya, K.; Tsukagoshi, K. *Adv. Mater.* **2010**, doi: 10.1002/adma.201002682
- 28) Fraboni, B.; Femoni, C.; Mencarelli, I.; Setti, L.; Di Pietro, R.; Cavallini, A.; Fraleoni-Margera, A. *Adv. Mater.* **2009**, 21, 1835
- 29) Guo, D.; Sakamoto, K.; Miki, K. *Appl. Phys. Lett.* **2007**, 90, 102117
- 30) Sirringhaus, H.; Brown, P. J.; Friend, R. H.; Nielsen, M. M.; Bechgaard, K.; Langevel-Voss, B. M. W.; Spiering, A. J. H.; Jannssen, R. A. J.; Meijer, E. W.; Herwig, P.; de Leeuw, D. M. *Science* **1999**, 401, 6754
- 31) Rivnay, J.; Jimison, L. H.; Northrup, J. E.; Toney, M. F.; Noriega, R.; Lu, S.; Marks, T. J.; Facchetti, A.; Salleo, A. *Nat. Mater.* **2009**, 8, 952
- 32) Jimison, L. H.; Toney, M. F.; McCulloch, I.; Heeney, M.; Salleo, A. *Adv. Mater.* **2009**, 21, 1568
- 33) Scheinert, S.; Paasch, G. *J. Appl. Phys.* **2009**, 105, 014509
- 34) Horowitz, G.; Hajlaoui, M. E.; Hajlaoui, R. *J. Appl. Phys.* **2000**, 87, 4456
- 35) Kline, R. J.; McGehee, M. D.; Toney, M. F. *Nat. Mater.* **2006**, 5, 222
- 36) Ito, K.; Suzuki, T.; Sakamoto, Y.; Kubota, D.; Inoue, Y.; Sato, F.; Tokito, S. *Angew. Chem., Int. Ed.* **2003**, 42, 1159

- 37) Laquindanum, J. G.; Katz, H. E.; Lovinger, A. J. *J. Am. Chem. Soc.* **1998**, 120, 664
- 38) Garnier, F.; G. Horowitz, Peng, X.; Fichou, D. *Solid State Commun.* **1990**, 72, 381
- 39) Horowitz, G.; Deloffre, F.; Garnier, F.; Hajlaoui, R.; Hmyene, M.; Yassar, A. *Synth. Met.* **1993**, 54, 435
- 40) Garnier, F.; Yassar, A.; Hajlaoui, R.; Horowitz, G.; Deloffre, F.; Servet, B.; Ries, S.; Alnot, P. *J. Am. Chem. Soc.* **1993**, 115, 8716
- 41) Katz, H. E. *J. Mater. Chem.* **1997**, 7, 369
- 42) Hajlaoui, M. E.; Garnier, F.; Hassine, L.; Kouki, F.; Bouchriha, H. *Synth. Met.* **2002**, 129, 215
- 43) Fichou, D. *Handbook of Oligo – and Polythiophenes; Wiley-VCH, New York, 1998*
- 44) Facchetti, A.; Mushrush, M.; Yoon, M.; Hutchison, G. R.; Ratner, M. A.; Marks, T. J. *J. Am. Chem. Soc.* **2004**, 126, 13859
- 45) Fichou, D. *J. Mater. Chem.* **2000**, 10, 571
- 46) Garnier, F.; Yassar, A.; Hajlaoui, R.; Horowitz, G.; Deloffre, F.; Servet, B.; Ries, S.; Alnot, P. *J. Am. Chem. Soc.* **1993**, 115, 8716
- 47) Takimiya, K.; Shinamura, S.; Osaka, I.; Miyazaki, E. *Adv. Mater.* **2011**, 23, 4347
- 48) Takimiya, K.; Ebata, H.; Sakamoto, K.; Izawa, T.; Otsubo, T.; Kunugi, Y. *J. Am. Chem. Soc.* **2006**, 128, 12604
- 49) Kang, M. J.; Doi, I.; Mori, H.; Miyazaki, E.; Takimiya, K.; Ikeda, M.; Kuwabara, H. *Adv. Mater.* **2010**, doi: 10.1002/adma.201001283
- 50) Gao, P.; Beckmann, D.; Tsao, H. N.; Feng, X.; Enkelmann, V.; Baumgarten, M.; Pisula, W.; Müllen, K. *Adv. Mater.* **2009**, 21, 213
- 51) Zhang, L.; Tan, L.; Wang, Z.; Hu, W.; Zhu, D. *Chem. Mater.* **2009**, 21, 1993
- 52) Chua, L. L.; Zaumseil, J.; Chang, J. F.; Ou, E. C. W.; Ho, P. K. H.; Sirringhaus, H.; Friend, R. H. *Nature* **2005**, 434, 194
- 53) Brown, A. R.; De Leeuw, D. M.; Lous, E. J.; Havinga, E. E. *Synth. Met.* **1994**, 66, 257
- 54) Chesterfield, R. J.; Newman, C. R.; Pappenfus, T. M.; Ewbank, P. C.; Haukass, M. H.; Mann, K. R.; Miller, L. L.; Frisbie, C. D. *Adv. Mater.* **2003**, 15, 1278

- 55) Facchetti, A.; Yoon, M. H.; Stern, C. L.; Hutchison, G. R.; Ratner, M. A.; Marks, T. J. *J. Am. Chem. Soc.* **2004**, 126, 13480
- 56) Ando, S.; Murakami, R.; Nishida, J.; Tada, H.; Inoue, Y.; Tokito, S.; Yamashita, Y. *J. Am. Chem. Soc.* **2005**, 127, 14996
- 57) Liang, Z.; Tang, Q.; Liu, J.; Li, J.; Yan, F.; Miao, Q. *Chem. Mater.* **2010**, doi: 10.1021/cm102681p
- 58) Jones, B. A.; Ahrens, M. J.; Yoon, M.-H.; Facchetti, A.; Marks, T. J.; Wasielewski, M. R. *Angew. Chem. Int. Ed.* **2004**, 43, 6363
- 59) Piliago, C.; Cordella, F.; Jarzab, D.; Lu, S.; Chen, Z.; Facchetti, A.; Loi, M. A. *Appl. Phys. A* **2009**, 95, 303
- 60) Weitz, R. T.; Amsharov, K.; Zschieschang, U.; Villas, E. B.; Goswami, D. K.; Burghard, M.; Helmut, D.; Jansen, M.; Kern, K.; Klauk, H. *J. Am. Chem. Soc.* **2008**, 130, 4637
- 61) Tiwari, S. P.; Namdas, E. B.; Rao, V. R.; Fichou, D.; Mhaisalkar, S. G.; *IEEE Electr. Device Lett.* **2007**, 28, 880
- 62) Wang, X.; Guo, Y.; Xiao, Y.; Zhang, L.; Yu, G.; Liu, Y. *J. Mater. Chem.* **2009**, 19, 3258
- 63) Kaneto, K.; Kohno, Y.; Yoshino, K.; Inuishi, Y. *J. Chem. Soc., Chem. Commun.* **1983**, 7, 382
- 64) Glenis, S.; Horowitz, G.; Tourillon, G.; Garnier, F. *Thin Solid Films*, **1984**, 111, 93
- 65) Sirringhaus, H.; Tessler, N.; Friend, R. H. *Science*, **1998**, 280, 1741
- 66) Bao, Z.; Dodabalapur, A.; Lovinger, A. J. *Appl. Phys. Lett.* **1996**, 69, 4108
- 67) Cho, S.; Lee, K.; Yuen, J.; Wang, G.; Moses, D.; Heeger, A. J.; Surin, M.; Lazzaroni, R. *J. Appl. Phys.* **2006**, 100, 114503
- 68) Osaka, I.; McCullough, R. D. *Acc. Chem. Res.* **2008**, 41, 1202
- 69) Kim, Y.; Cook, S.; Tuladhar, S. M.; Choulis, S. A.; Nelson, J.; Durrant, J. R.; Bradley, D. D. C.; Giles, M.; McCulloch, I.; Ha, C.-S.; Ree, M. *Nat. Mater.* **2006**, 5, 197
- 70) Ong, B. S.; Wu, Y.; Liu, P.; Gardner, S. *J. Am. Chem. Soc.* **2004**, 126, 3378
- 71) McCulloch, I.; Heeney, M.; Bailey, C.; Genevicius, K.; MacDonald, I.; Shkunov, M.; Sparrowe, D.; Tierney, S.; Wagner, R.; Zhang, W.; Chabinyc, M. L.; Kline, R. J.; McGehee, M. D.; Toney, M. F. *Nat. Mater.* **2006**, 5, 328
- 72) Leclerc, M. *J. Polym. Sci., Part A: Polym. Chem.* **2001**, 39, 2867

- 73) Bernius, M.; Inbasekaran, M.; Woo, E.; Wu, W.; Wujkowski, L. *J. Mater. Sci.-Mater. Electron.* **2000**, 11, 111
- 74) Veres, J.; Ogier, S.; Lloyd, G.; de Leeuw, D. *Chem. Mater.* **2004**, 16, 4543
- 75) Lu, G.; Usta, H.; Risko, C.; Wang, L.; Facchetti, A.; Ratner, M. A.; Marks, T. J. *J. Am. Chem. Soc.* **2008**, 130, 7670
- 76) Tu, G.; Massip, S.; Oberhummer, P. M.; He, X.; Friend, R. H.; Greenham, N. C.; Huck, W. T. S. *J. Mater Chem.* **2010**, 20, 9231
- 77) Redecker, M.; Bradley, D. D. C.; Inbasekaran, M.; Wu, W. W.; Woo, E. P. *Adv. Mater.* **1999**, 11, 241
- 78) Li, Y.; Wu, Y.; Ong, B. S. *Macromolecules* **2006**, 39, 6521
- 79) Babel, A.; Jenekhe, S. A. *J. Am. Chem. Soc.* **2003**, 125, 13656
- 80) Jenekhe, S. A.; Yi, S. *Appl. Phys. Lett.* **2000**, 77, 2635
- 81) Yan, H.; Chen, Z.; Zheng, Y.; Newman, C.; Quinn, J. R.; Dötz, F.; Kastler, M.; Facchetti, A. *Nature* **2009**, 457, 679
- 82) Cho, S.; Lee, J.; Tong, M.; Seo, J. H.; Yang, C. *Adv. Mater.* **2011**, 21, 1910
- 83) Nakyama, K.; Hirose, Y.; Soeda, J.; Yoshizumi, M.; Uemura, T.; Uno, M.; Li, W.; Kang, M. J.; Yamagishi, M.; Okada, Y.; Miyazaki, E.; Nakazawa, Y.; Nakao, A.; Takimiya, K.; Takeya, J. *Adv. Mater.* **2011**, 23, 1626

CHAPTER 2

Self-Assembly of Poly(3-hexylthiophene) via End-Group Modification

2.1 Introduction

The realization of ink-jet printing for low cost organic circuitry has opened the door for practical applications of organic field effect transistors (OFETs) such as in active-matrix displays.^[1,2,3] Additionally, the ability to pattern organic devices on sensitive substrates such as degradable polyesters has led to research efforts towards unconventional applications such as biocompatible electronics.⁴ However, the hole mobility of solution processed organic semiconductors remains near that of amorphous silicon, which limits practical applications of OFETs. Several studies have shown that the charge carrier mobility of organic transistors is greatly affected by the number and nature of grain boundaries in the thin film.^[5,6,7] Therefore, control of the solid state ordering of conjugated polymers is of utmost importance for improving their electrical properties.

Among the various solution processable organic semiconductors, regioregular poly(3-hexylthiophene) (P3HT) has become a performance standard for OFETs due to its refined synthesis, good solubility, and high hole mobility ($0.1\text{-}0.3\text{ cm}^2/\text{Vs}$).^[8-11] Brinkmann and Rannou recently studied the microstructure of directionally crystallized P3HT films and found that samples of higher molecular weight (and slightly higher PDI) afforded films with reduced local order, but better lamellar interconnectivity due to the presence of tie chains.^[12] This offered a refined explanation for why higher molecular weight P3HT generally exhibits higher hole mobility. More recently, Jimison *et al.* studied

charge transport anisotropy in directionally crystallized films of P3HT.^[5] These studies found that transport through low angle grain boundaries is most efficient in the direction parallel to the polymer backbone due to increased crystallite interconnectivity in this direction, consistent with the hypothesis of Brinkmann and Rannou.

A related polymer, poly(2,5-bis(3-alkylthiophen-2-yl)thieno[3,2-*b*]thiophene (PBTT) studied by McCulloch *et al.* afforded OFETs with very high mobilities of up to 0.6 cm²/Vs as a result of better ordering of crystalline grains due to the presence of a mesophase. Dark-field transmission electron microscopy was later used to characterize the morphology of PBTT, which depicted a nematic like in-plane texture with quasi domains comprised of several adjacent highly oriented crystalline grains.^[6]

These studies have highlighted the importance of grain boundaries in conjugated polymer films and demonstrate the need for novel approaches to crystalline grain interconnectivity. Towards this goal, end-group functionalization was explored as a method for improving charge percolation in P3HT thin films. It was hypothesized that polymer end-groups with strong intermolecular interactions might lead to enhanced tie-chain formation as depicted in Figure 2.1. This could be a useful method for improving

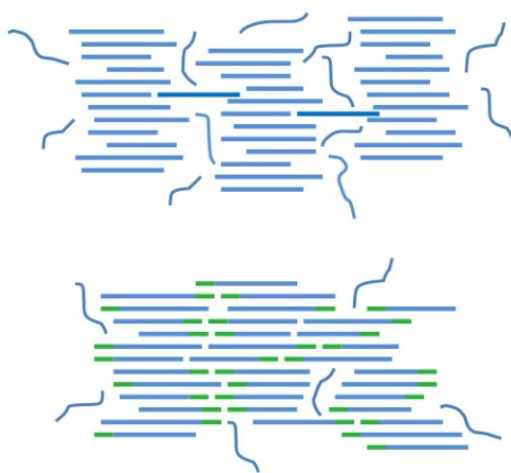
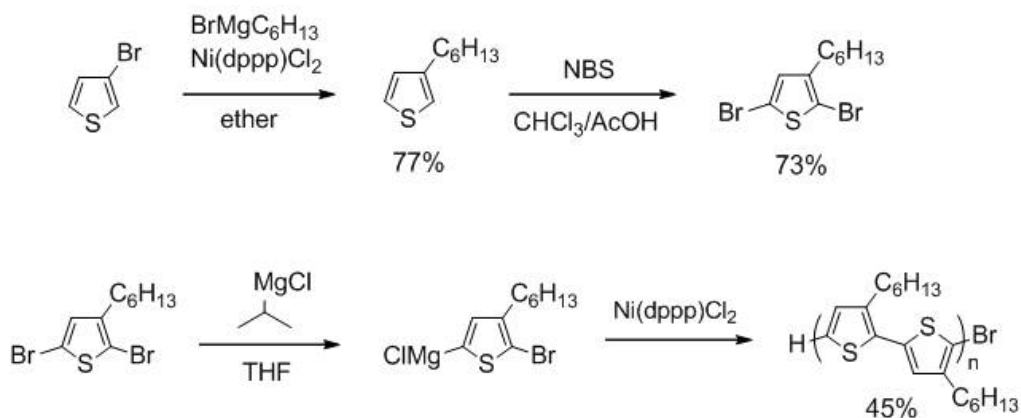


Figure 2.1 Illustration of semicrystalline morphology of P3HT (top) and the potential morphology of end-substituted P3HT derivatives

percolation networks in conjugated polymer thin films. First an unsubstituted quaterthiophene end-group was explored for improving π - π stacking at the polymer ends. In addition a perfluoroalkyl end-substituted P3HT derivative was explored for fluorophilic assembly at the polymer ends.

2.2 Synthesis

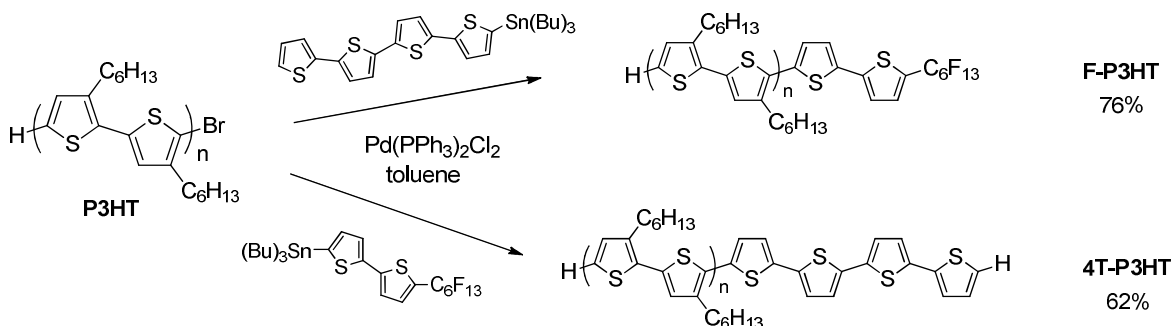
The synthesis of P3HT has matured over the years, and can now be polymerized by highly controlled methods that afford highly regioregular polymer.¹¹ The most common method for achieving head-to-tail (H-T) P3HT is the Grignard Metathesis (GRIM) method which utilizes 2,5-dibromo-3-hexylthiophene as monomer. This route is convenient because the dibrominated monomer is easily accessible and affords a selective magnesium exchange at the 5-position of the thiophene ring. Interestingly, while this method affords about 85% magnesium exchange at the 5-position and 15% magnesium exchange at the 2-position, the overall H-T coupling is typically greater than 95%.¹¹ The GRIM method affords P3HT with an end-group distribution that is typically > 85% H-Br and < 15% H-H. This allows for coupling reactions involving the bromine end-group for further end-functionalization. Polymerization of 2,5-dibromo-3-hexylthiophene



Scheme 2.1 Synthesis of P3HT using the GRIM method

thus afforded the P3HT used in these studies with a H-T coupling of $\approx 96\%$ (Scheme 2.1). The P3HT was first purified via precipitation into methanol and then fractionated by washing with hexanes in a soxhlet and finally extracting with chloroform from the soxhlet. The high molecular weight chloroform fraction was used for subsequent reactions.

Several methods have been developed for the end-functionalization of P3HT including in-situ kumada end-capping¹² as well as post-polymerization negishi end-capping.¹³ Both methods have advantages and disadvantages. Post-polymerization functionalization allows for a consistent precursor batch to be used for the synthesis of different end-substituted polymers, allowing for an analysis of polymers with identical molecular weight. For this reason a post-polymerization method was chosen for the polymers in the following studies. Initially, α,ω -disubstituted P3HT was desired in order to study the effects of complete end-group conversion. Attempts to dilithiate both polymer end-groups were unsuccessful due to limited solubility of the polymer, resulting in incomplete deprotonation. Thus, metallation of both polymer end-groups was not possible. Instead the bromine end-group was used in a Stille coupling reaction to afford ω -end-substituted P3HT (Scheme 2.2). Stille coupling was found to be ideal since the reaction could be carried out under high temperatures in toluene, conditions favorable



Scheme 2.2 Synthesis of end-functionalized P3HT via post-polymerization Stille coupling

for the dissolution of P3HT. Furthermore the highly soluble tributylstannyl compounds were easily separated from the polymer via precipitation, affording a product that did not require further purification.

2.3 Characterization

Polymer molecular weights and end-group identity were characterized using matrix-assisted laser desorption ionization time of flight (MALDI-TOF) mass spec. MALDI is an important tool for characterization of P3HT since it can give absolute molecular weight and unambiguous end-group characterization.¹⁴ The MALDI spectra of the as synthesized P3HT is shown in Figure 2.2.

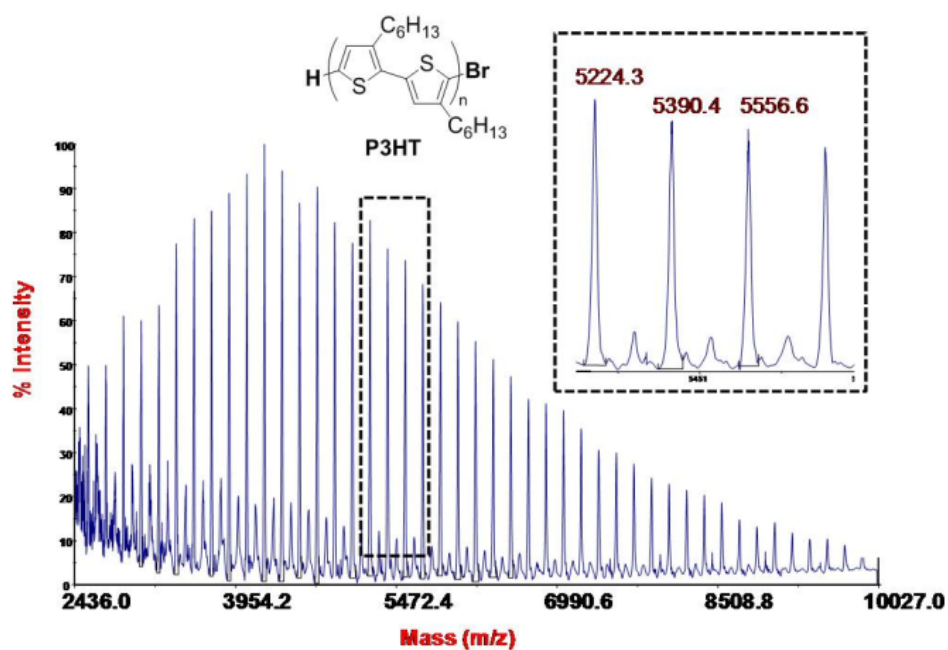


Figure 2.2 MALDI MS spectra of H-P3HT-Br

The number average molecular weight of the P3HT was found to be $\approx 4,000$ g/mol, with an end-group distribution of approximately 85% H-Br and 15% H-H end groups. End-

group identity can be determined by subtracting potential end group masses from the observed peaks in the spectrum and dividing by the repeat mass to check for an integer value. For example in the P3HT spectra peak 5,390.4 g/mol matches closely to $1 \times \text{H}$ (1.008) + $1 \times \text{Br}$ (79.9) + $32 \times \text{repeat unit}$ (166.3) = 5,402.5.

The MALDI spectra for the end-substituted polymers is shown in Figure 2.3. For perfluoroalkylated F-P3HT the MALDI shows full conversion of the bromine end group to

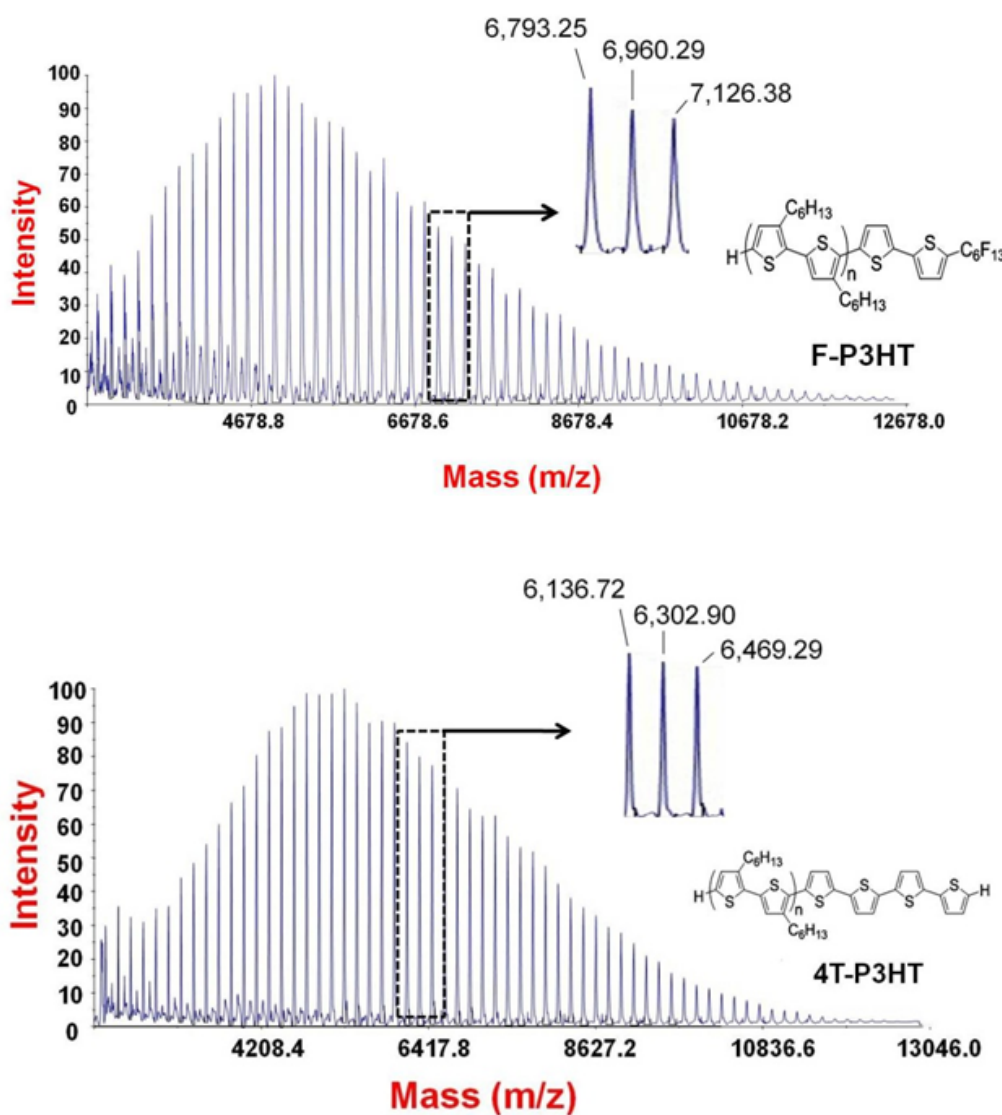


Figure 2.3 MALDI MS spectra of F-P3HT and 4T-P3HT

the new perfluorohexyl end group. For example peak 6,302.9 g/mol closely matches $1 \times \text{H}$ (1.008) + $1 \times \text{end-group}$ (483.4) + $35 \times \text{repeat unit}$ (166.3) = 6304.9. Some peaks corresponding to H-H end groups can be observed at lower molecular weights. In contrast to F-P3HT, 4T-P3HT can not be confidently identified solely using MALDI mass spec since the mass of the quaterthiophene end group is very close to twice the mass of one repeat unit, and thus can not be distinguished from polymer with H-H end groups. However, assuming dehalogenation did not occur the MALDI spectra is consistent with full conversion of the bromine end groups to the quaterthiophene end groups.

Proton and fluorine NMR were used for further characterization of the new polymers. Spectra were taken in $\text{C}_2\text{D}_2\text{Cl}_4$ in order to avoid overlap between aromatic protons and the solvent, and to allow for high temperature experiments to give better solubility and higher signal to noise. The aromatic region of the ^1H NMR spectra for the three polymers are shown in Figure 2.4. The P3HT spectra shows only a single peak at 6.41 ppm corresponding to the aromatic

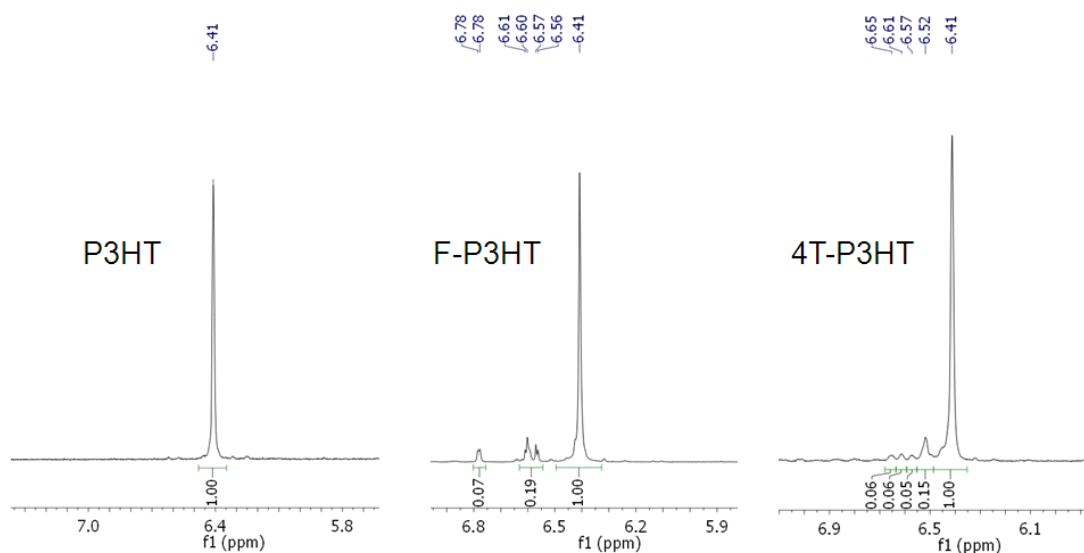


Figure 2.4 Aromatic region of ^1H NMR spectra with end-group peaks (taken in $\text{C}_2\text{D}_2\text{Cl}_4$ at 383 K)

proton of the repeat unit. The spectra of F-P3HT and 4T-P3HT both show new aromatic peaks that result from the aromatic protons on the end-groups. Calculating molecular weight from the end-group peaks is difficult because the end-group resonances are hard to assign for F-P3HT and 4T-P3HT. However, comparing integration of one end-group peak observed in the 4T-P3HT spectrum to the repeat unit peak, a molecular weight of $\approx 3,000$ g/mol is determined, in relatively close agreement with the MADLI data. The ^{19}F NMR spectra of F-P3HT (Figure 2.5) showed the six expected signals of the perfluorohexyl end-group, further verifying the purity of the polymer.

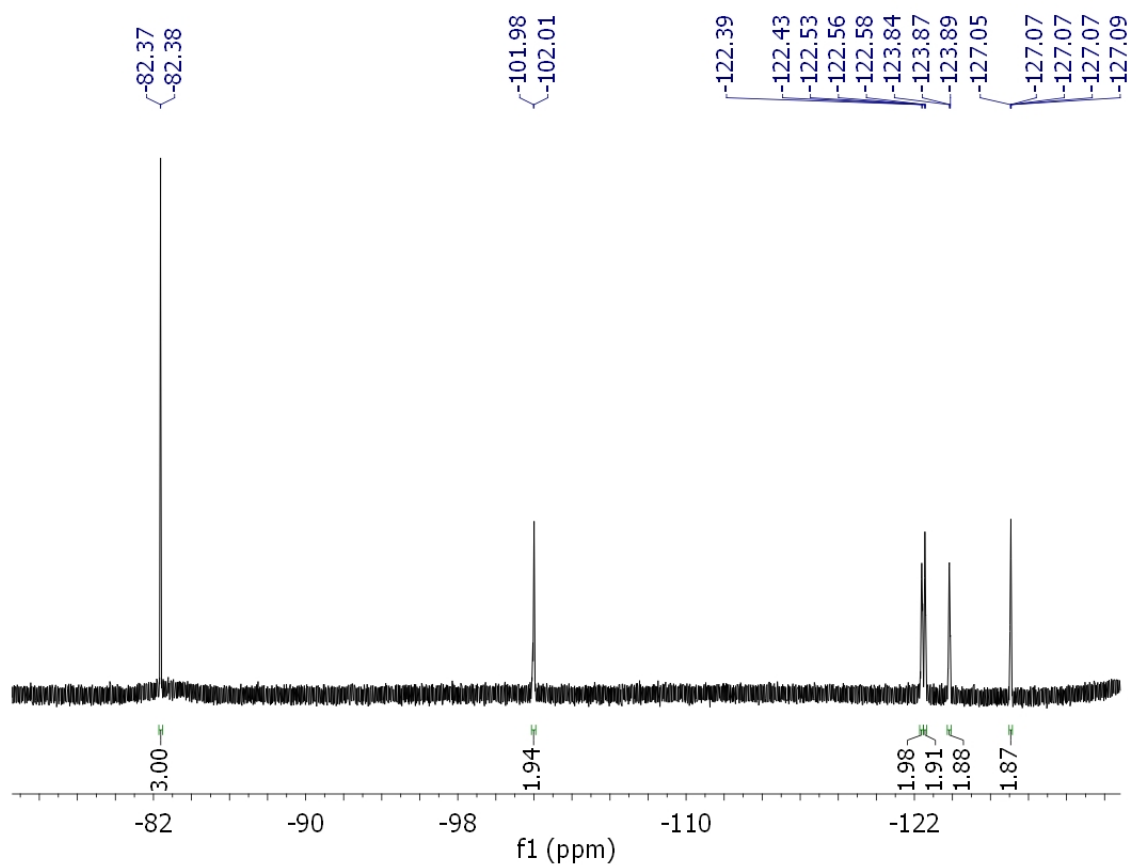


Figure 2.5 ^{19}F NMR spectrum of F-P3HT (taken in $\text{C}_2\text{D}_2\text{Cl}_4$ at 383 K)

Finally, gel permeation chromatography (GPC) was used in order to evaluate any differences in polydispersity that may rise from the end-group functionalization. Monomodal distributions were observed for all three polymers, which all had polydispersion indices (PDI) of 1.4 (Figure 2.6). The molecular weight of P3HT determined by GPC (relative to polystyrene standards) was 35,000 g/mol. The large discrepancy between the MALDI determined $\langle M_n \rangle$ and the GPC determined $\langle M_n \rangle$ exemplifies the limitation of GPC for determining molecular weight of rigid-rod conjugated polymers using a polystyrene reference. The molecular weights of F-P3HT and 4T-P3HT were identical at 37,500 g/mol, further evidence of the successful end-functionalization.

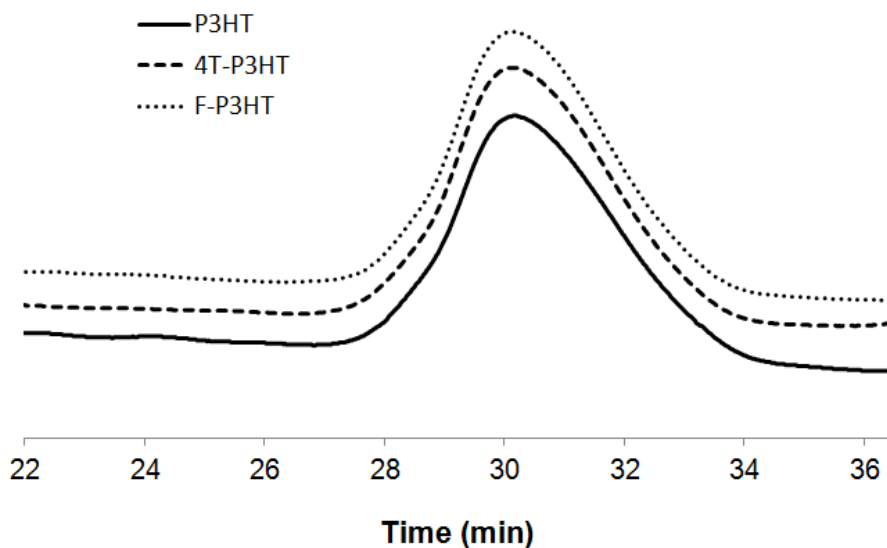


Figure 2.6 Polymer GPC traces (THF at 35 °C)

2.4 Thermal Properties

In order to understand how the polymer end-group affects intermolecular forces within the series of polymers, thermal transitions were evaluated using differential

scanning calorimetry (DSC). The end-perfluoroalkylated F-P3HT showed interesting differences compared to P3HT. First, a sharp melting peak was observed at 208 °C for F-P3HT, separate from the melting point of the polymer backbone (Figure 2.7). Impurities were ruled out as a potential cause for this peak considering the clean ^1H and ^{19}F NMR spectra as well as the MALDI spectrum. This peak was attributed to melting of the perfluoroalkyl-bithiophene end group. There is little precedence in the literature for such a sharp high temperature melting of a polymer end group. In the case of F-P3HT the end group is conjugated with the π -system and lacks lateral substitution, allowing for efficient packing. Such a high melting point of the end-group must be a result of unique crystallization that includes the end group but also propagates into the polymer repeat units to some extent. No morphological changes could be observed using polarized optical microscopy when heating through the initial end-group melting. F-P3HT also showed a high temperature shoulder at the polymer melting point which was attributed to the slightly higher molecular weight of the end-substituted polymer.

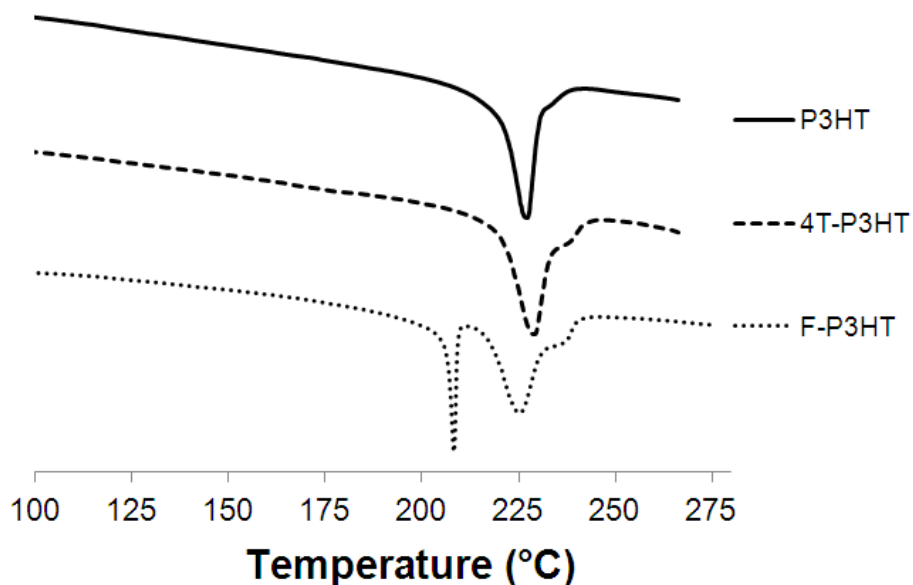


Figure 2.7 Second heating thermograms of the polymers (endotherm is down)

Compared to P3HT the thermogram of 4T-P3HT showed very similar characteristics. The melting point of 4T-P3HT was identical to that of P3HT but also showed a high temperature tail similar to F-P3HT. This was again attributed to the higher molecular weight fraction of polymer after end-functionalization.

2.5 Optical/Electrochemical Properties

The influence of the polymer end-group on the electronic states of P3HT was examined through UV/vis, fluorescence, and cyclic voltammetry measurements. The polymer end-group had little effect on the UV/vis spectra (Figure 2.8). The maximum for the π - π^* transition of F-P3HT (442 nm) was slightly blueshifted compared to P3HT and 4T-P3HT (450 nm). This may be due to unique absorption of the conjugated region located at the perfluoroalkylated end-group. However, the shift is very small and the onset of absorption is identical for all polymers, indicating identical band gaps. No other differences could be observed in the optical properties of three polymers. UV/vis spectra of polymer films all showed the vibrational structure typical of P3HT, a result of planarization of the polymer backbone in the film as well as intermolecular coupling of the electronic states. Similarity in the solid state spectra indicates similar morphologies and intermolecular interactions.

Previous studies found that α,ω perfluoroalkylation greatly increased fluorescence quantum yields of oligothiophenes.¹⁵ Fluorescence quantum yields were calculated for P3HT and F-P3HT using rhodamine B as standard. Both polymers had a calculated quantum yield of 0.29 in THF solutions. Thus ω -perfluoroalkylation does not affect the fluorescence properties of P3HT. Overall the three polymers showed almost identical optical properties dominated by the polymer backbone.

Perfluoroalkyl substitution is also known to significantly lower the frontier molecular orbitals of oligothiophenes.⁸ In the case of F-P3HT this could affect both hole

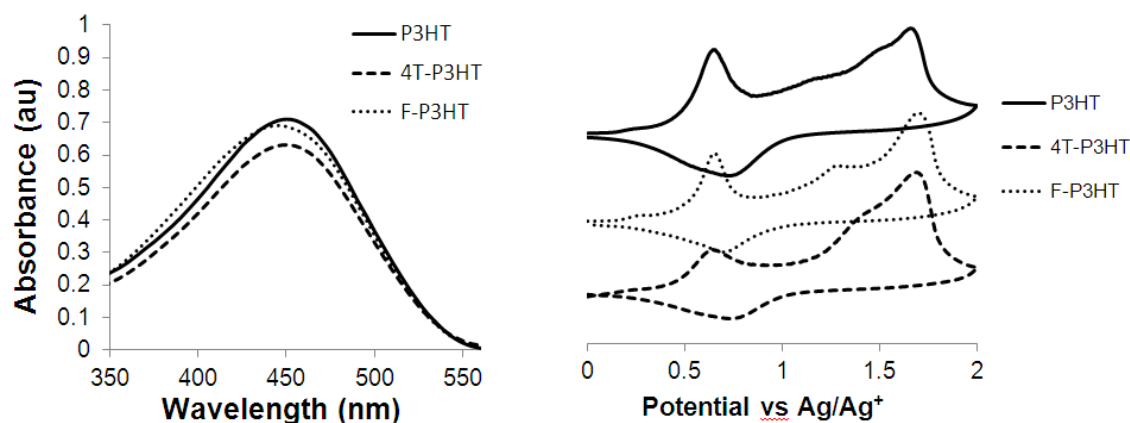


Figure 2.8 UV/vis spectra (left) and oxidative cyclic voltammograms (right) of the polymers

injection as well as the oxidative stability of the polymer. However, the cyclic voltammograms of the three polymers showed indistinguishable oxidation potentials, with calculated HOMO levels of -4.9 eV. This further demonstrates the similarity of electronic states for the three polymers.

2.6 Morphological/Self Assembly Properties

P3HT is known to assemble into 1-dimensional lamella consisting of π -stacks, separated by layers of alkyl side-chains. These structures can be isolated as 'nanowhiskers' by recrystallizing the polymer from a poor solvent.¹⁶ A simplified schematic of this lamellar morphology is depicted in Figure 2.9 along with an illustration of a P3HT nanowhisker. A comparison of the self-assembly behavior of the three polymers was conducted by recrystallizing each polymer from methylene chloride and imaging the resulting structures using TEM (Figure 2.10). The resulting nanowhiskers were indistinguishable from each other. The width of each nanowhisker is defined by the length of the polymer backbone and is therefore dependent on molecular weight as well

as the degree of chain folding.¹⁷ The average width of the nanowhiskers were: 17.0 nm (± 2.0 nm) for P3HT, 16.8 nm (± 2.0 nm) for 4T-P3HT, and 18.1 nm (± 2.5 nm) for F-P3HT. The small differences between nanowhisker widths reveals the similar self-assembly properties of all three polymers. The end-group identity does not appear to significantly affect the degree of chain folding.

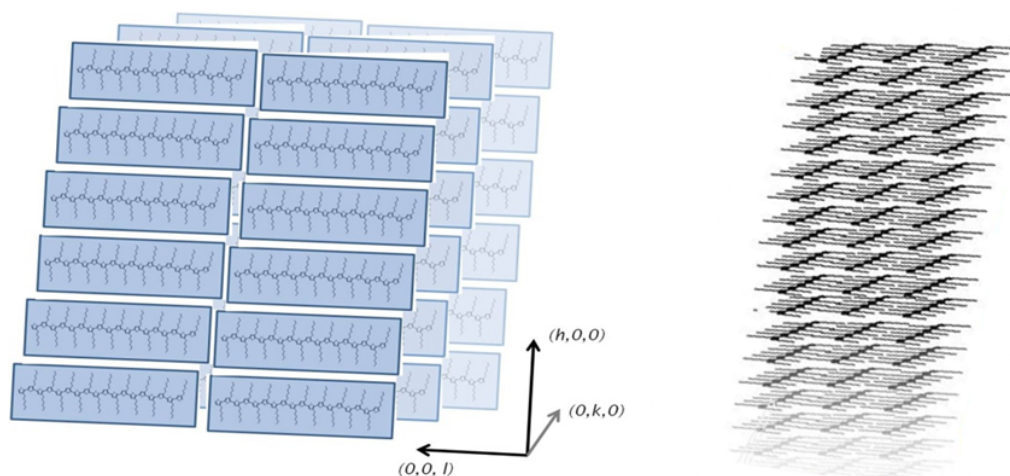


Figure 2.9 Illustration of P3HT lamella with crystallographic indices (left) and an individual P3HT nanowhisker (right)

Film morphologies that arise from spincoating from chloroform solutions were also analyzed using AFM (Figure 2.10). In these experiments the imaging only captures the surface of the film and gives information limited to the meso and macroscale ordering of the polymers. Again, no significant differences were observed in the morphologies; however, the surface roughness of both 4T-P3HT (2.6 nm) and F-P3HT (2.7 nm) was more than twice that of P3HT (1.1 nm). This is likely due to increased aggregation of the end-substituted polymers as a result of the reduced solubility near the end-group.

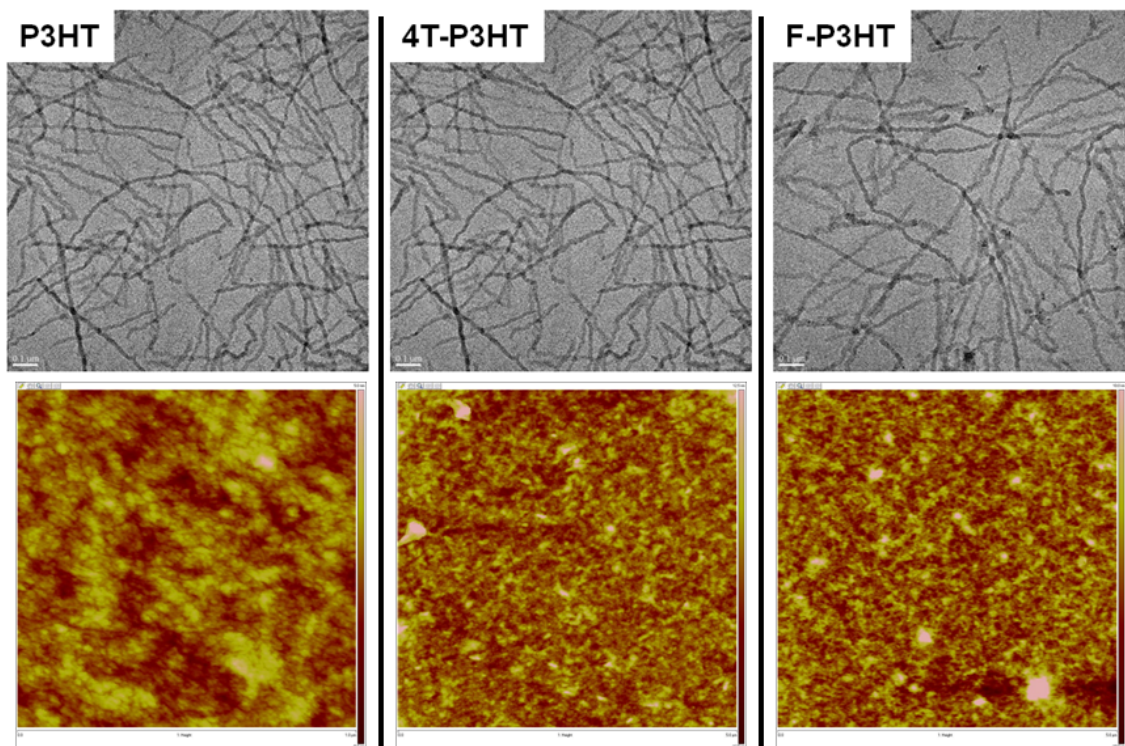


Figure 2.10 TEM images of polymer nanowhiskers grown via recrystallization from CH_2Cl_2 (top) and AFM images of spin-cast films from CHCl_3

The good solubility of F-P3HT in chloroform would presumably allow for end-group interactions in solution as a result of solvophobic assembly of the perfluoroalkyl tail. Fluorophilic assembly of F-P3HT was therefore studied by dropcasting a dilute solution of the polymer in chloroform onto a TEM grid (Figure 2.11). Interestingly the films were comprised entirely of flat circles on the order of 1-7 μm . The polymer was found almost entirely in the ring of the circle, with very little material elsewhere. The width of the rings defining the circles was between 35-40 nm, approximately twice the length of the previously observed F-P3HT nanowhiskers. The circular structures can therefore be attributed to a bilayer vesicle as a result of the fluorophilic tail of F-P3HT. Interestingly the vesicles are much larger than would be expected from the size of the polymer, most likely due to vesicle combination as the solution dries and the

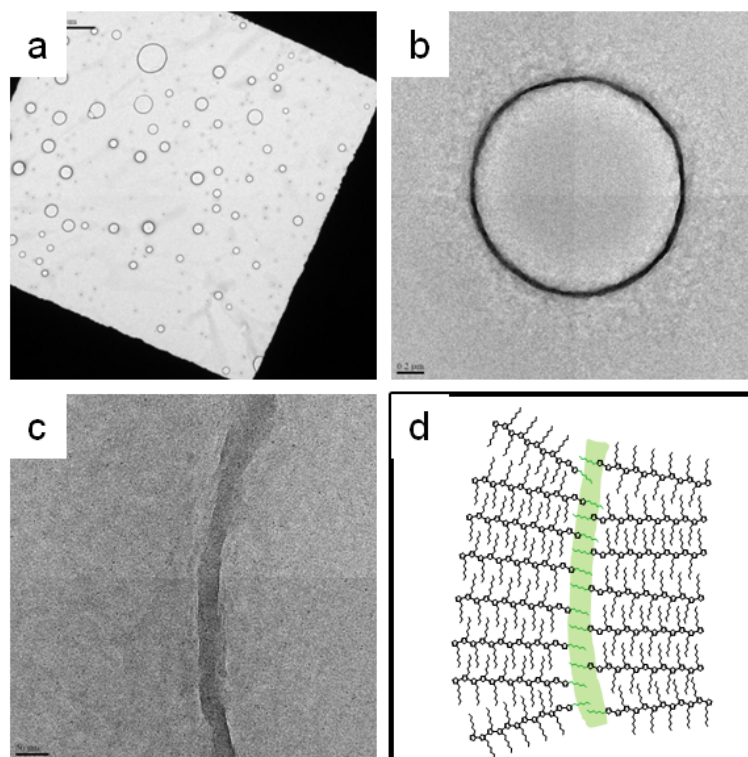


Figure 2.11 TEM images of F-P3HT vesicles dropcast from 0.025 wt% CHCl_3 solution (a-c) and illustration of bilayer vesicle structure (d)

concentration of vesicles increases. In fact, vesicle combination is observed in some TEM images where two vesicles appear to be joined together. Figure 2.12 shows two vesicles which have merged, where the vesicle membrane can be seen to have ruptured to incorporate the new segment. This is the first example of a bilayer vesicle formed from a conjugated polymer. Furthermore the formation of a vesicle was induced by a small molecule end-group, thus providing new P3HT assembly behavior without disrupting the materials' properties.

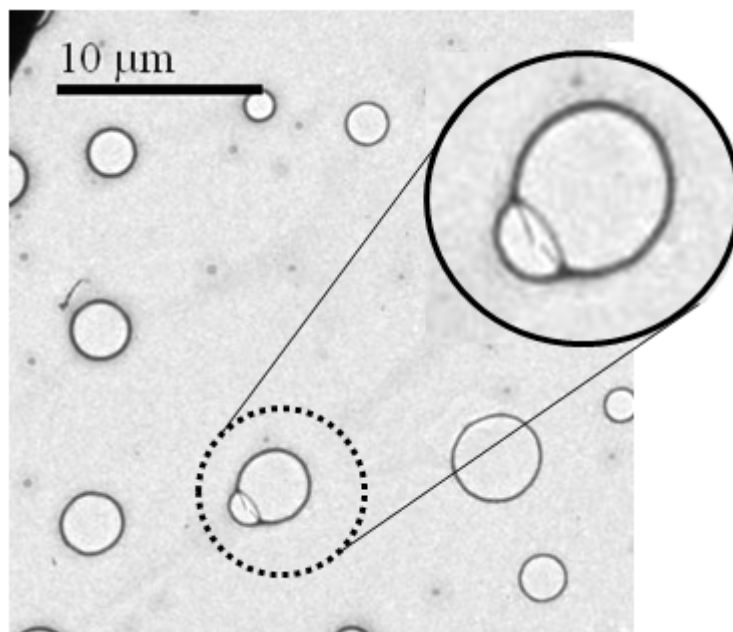


Figure 2.12 TEM image of F-P3HT vesicles showing two vesicles merging

2.7 Blend Studies

In the field of organic photovoltaics a blend of p-type semiconductor and n-type semiconductor is used in order to dissociate excitons at the p-n junction and ultimately collect charge to generate power. The p-n interface and morphology in these devices is thus crucial for efficient conversion of light to electricity. An intimate contact between p and n semiconductors is necessary for efficient exciton dissociation, while pure p and n regimes that percolate between electrodes is ideal for charge extraction. Methods that have been used to control the p-n interface/morphology include ball-and-socket joints¹⁸ and 'double-cable' polymers.¹⁹ To date, fluorophilic interactions have not been utilized for controlling blend morphologies.

The observed self-organization of F-P3HT into vesicles through fluorophilic assembly prompted studies of cross assembly between F-P3HT and other fluorophilic materials. To investigate this issue, blends of F-P3HT with other semiconductors, both unsubstituted and perfluoroalkylated, were studied using DSC. Figure 2.13 shows the

small molecules α 5T and DFH-5T that were blended with F-P3HT, along with their first heating thermograms. Both compounds are crystalline with melting temperatures near 250 °C. First F-P3HT was blended with α 5T (1:1 molar) and the mixture was taken through a heat-cool-heat series. The first heating of the mixture clearly shows the melting of the F-P3HT end-group followed by the polymer melting (Figure 2.14). The melting peak of α 5T is diminished, most likely because of premature melting induced by the liquid polymer. When the blend was cooled a single exotherm is observed. The second heating again shows the end-group melting followed by the polymer melting. The melting peak for α 5T is not present in the second heating, probably due to inhibited crystallization of the oligomer as a result of the similarity in molecular structures of α 5T and the polymer.

Significantly different behavior was observed when DFH-5T was blended with F-P3HT. The first heating shows the polymer end-group melting followed by the polymer

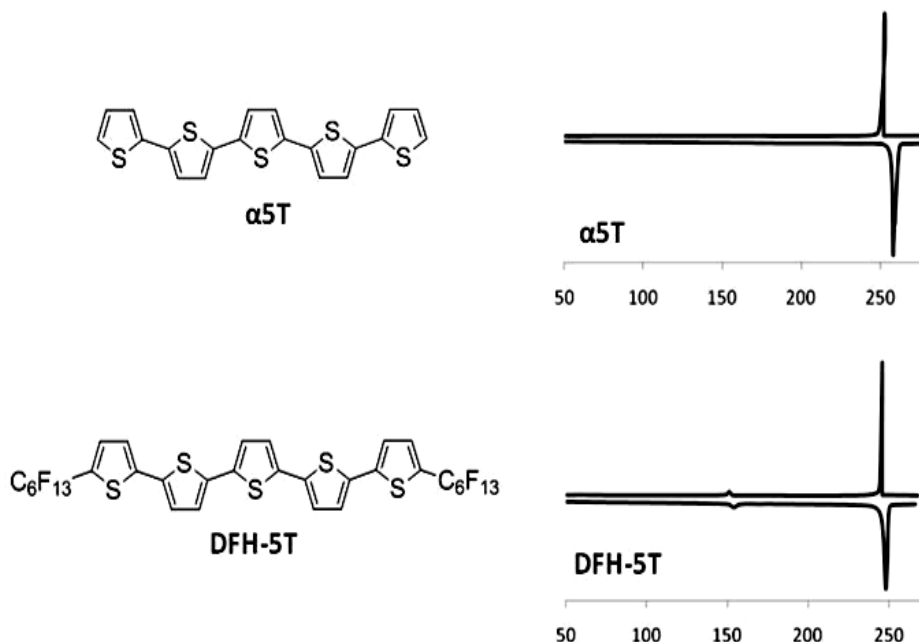


Figure 2.13 First heating thermograms of α 5T and DFH-5T

melting which has several shoulders, probably due to early melting of DFH-5T. Upon cooling an initial broad exotherm is observed near 220 °C followed by a sharper crystallization around 200 °C. Interestingly, the second heating shows almost complete disappearance of the end-group melting peak. This implies that crystallization of the perfluoroalkyl polymer end-group was inhibited by DFH-5T, but not by α 5T. Considering the otherwise identical structures of α 5T and DFH-5T this can be attributed to fluorophilic interactions between the perfluoroalkyl polymer end-group and the perfluoroalkyl chains of DFH-5T. Therefore, it is hypothesized that, through fluorophilic interactions, DFH-5T has intercalated within the lamellar structure of F-P3HT. This has significant implications

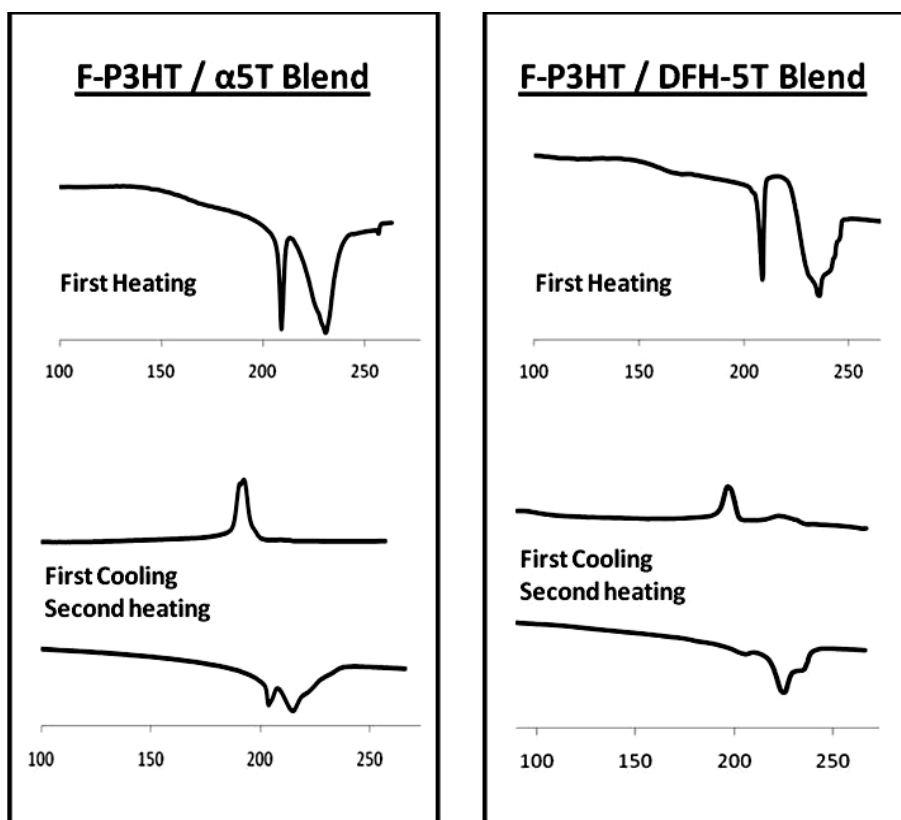


Figure 2.14 DSC thermograms of F-P3HT blended with α 5T and DFH-5T

on the ability to use fluorophilic assembly to control blend morphology, and could prove useful for applications such as photovoltaics.

2.8 Field Effect Transistor Characterization

Bottom-contact bottom-gate field effect transistors were fabricated in order to investigate any differences in charge mobility that arise from the end-group identity. Polymer solutions were spincoated onto devices from chloroform solutions, and devices were measured in air while blowing a stream of nitrogen over the transistor channel. The average hole mobilities of the three polymers are given in Table 1. All of the polymers have similar hole mobilities that lie within the standard deviation of each other. Furthermore, the devices showed a similar increase in mobility after annealing at 150 °C.

The polymer end-group does not appear to affect the charge mobility within this series of polymers. This implies that the rate limiting charge transport events, typically believed to be related to transport from one crystalline lamella to another, are not affected by the end-group identity. Previous studies showed that higher molecular weight P3HT leads to better tie chain formation and as a result shows higher hole mobilities.¹² Thus, extending the polymer chain length appears to be more effective at increasing tie chain formation than simply modifying the polymer end-group.

The ability for F-P3HT to assemble into vesicles, and to co-assemble with other perfluoroalkylated materials is especially interesting considering the polymer's

Table 2.1 Hole mobilities calculated from the saturation regime (average of ten devices)

Polymer	P3HT	4T-P3HT	F-P3HT
μ_h (cm ² /Vs)	0.032 (± 0.007)	0.037 (± 0.006)	0.031 (± 0.004)

undisturbed electrical properties. The output and transfer characteristics of a typical FET device employing F-P3HT are shown in Figure 2.15. Like P3HT, F-P3HT shows large positive threshold voltages. This arises from the high HOMO level, which leads to the formation of a charge transfer salt in the presence of water and oxygen. The doped polymer is conductive and therefore requires a positive gate bias in order to reduce the polymer to its non-conductive state. This characteristic of P3HT is undesirable because it requires excessive power consumption during device operation. This also leads to high off current, which limits the on/off current ratio to $\approx 10^3$ for F-P3HT devices measured outside of a glovebox.

Overall, within the polymer series studied, end-group modification was not found to affect the charge transport properties of P3HT. Transistor device characteristics were very similar for all three polymers which showed relatively high hole mobilities but positive threshold voltages and low on/off currents. However, the intact electrical properties of F-P3HT make it a good candidate for electronic applications that could benefit from fluorophilic interactions.

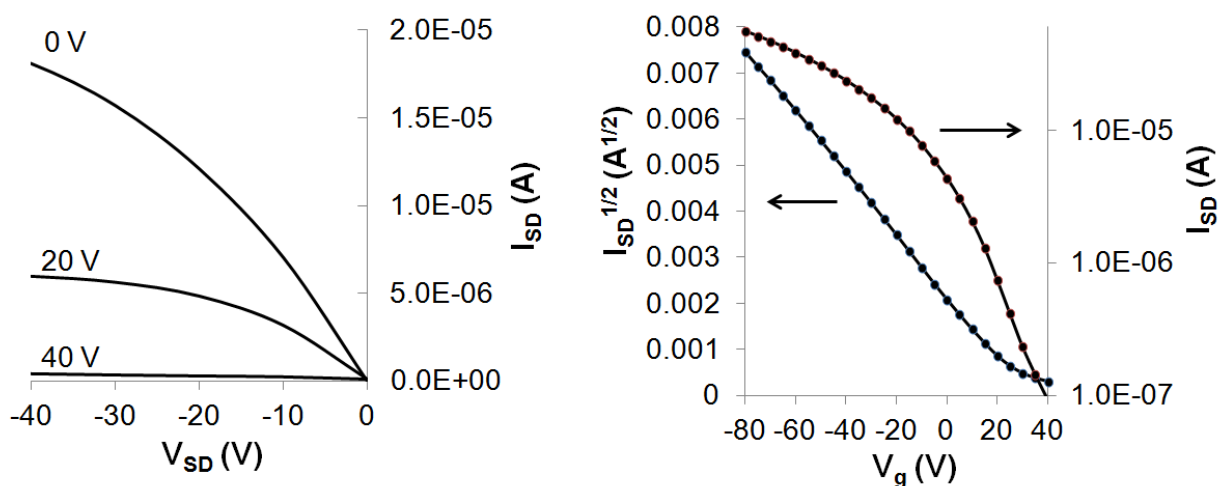


Figure 2.15 Output (left) and transfer (right) characteristics of F-P3HT devices

2.9 Conclusion

End-group modification was investigated as a potential method for improving charge percolation in conjugated polymer films. Conjugation of an unsubstituted quaterthiophene end-group led to increased aggregation of the polymer as a result of the lower solubility of the quaterthiophene end-group. This was evidenced through the darkening of 4T-P3HT solutions as well as the higher surface roughness of 4T-P3HT compared to P3HT. However, in all other ways the polymer behaved identical to P3HT, including the FET device characteristics. A perfluoroalkyl end-group was also utilized, which led to unique self-assembly of the polymer into a bilayer vesicle structure as a result of the amphiphilic nature of the polymer. In addition, DSC studies showed that F-P3HT interacted with perfluoroalkyl substituted oligothiophenes in the solid state as a result of fluorophilic interactions between the two materials.

Aside from the unique self-assembly, the properties of F-P3HT were otherwise identical to P3HT. Thus, while end-group modification was found to be unsuccessful for improving charge percolation, F-P3HT was discovered as an interesting candidate for supramolecular semiconductor structures. For example, in photovoltaics where morphology engineering is extremely important for enhancing power conversion efficiencies, blends of fluorophilic materials might be useful for forming intimate contact at the p-n interface as well as for modifying the mesoscale morphology. This could potentially be achieved by blending F-P3HT with a perfluoroalkylated fullerene. In this case fluorophilic interactions could improve the p-n interface and lead to unique mesoscale ordering of the blend morphology as depicted in Figure 2.16.



Figure 2.16 Illustration of potential supramolecular assembly between F-P3HT and a fluorinated fullerene

2.10 Experimental

Materials. All reagents were purchased from Sigma-Aldrich and used without further purification unless otherwise noted. Regioregular poly(3-hexylthiophene),¹¹ 5-(n-tributylstannyl)-2,2'-bithiophene,²⁰ 5-perfluorohexyl-5'-(n-tributylstannyl)-2,2'-bithiophene,¹⁵ and terthiophene²¹ were synthesized via procedures in literature. α -Quaterthiophene was synthesized via nickel catalyzed negishi coupling of 2,2'-bithiophene with 5-bromo-2,2'-bithiophene.

Instrumentation. UV/vis spectra were acquired using a Varian Cary 50 UV/Vis spectrometer. Cyclic voltammetry was performed using a Bioanalytical Systems (BAS) Epsilon potentiostat equipped with a standard three-electrode configuration. Scans were performed on oligomer films evaporated onto a glassy carbon electrode which served as the working electrode. A Pt wire was used as counter electrode and an Ag/AgNO₃ (0.01 M in anhydrous acetonitrile) was used as the reference electrode. Measurements were performed in anhydrous acetonitrile with tetrabutylammonium hexafluorophosphate (0.1 M) as supporting electrolyte under nitrogen at a scan rate of 100 mV/s. Internal calibration of the reference potential was achieved using the ferrocene/ferrocenium

redox couple. Melting points and thermal transitions were analyzed using a TA instruments Q200 differential scanning calorimeter.

TEM images were obtained using a JEOL 2010F FastEM at an accelerating voltage of 200 kV. Nanowhiskers were formed by heating a 2 mg/mL solution in methylene chloride to 50 °C and allowing to cool to room temperature slowly. The precipitated nanowhiskers were allowed to sit for 1 h before being diluted 10x and then dropcast onto a TEM grid for imaging. F-P3HT vesicles were prepared by forming a 0.025 wt% solution of F-P3HT in chloroform and allowing to sit for 30 min. The solution was then dropcast onto a TEM grid. AFM images were obtained using a Veeco Nanoscope V operating under peak force mode.

NMR spectra were obtained on a Bruker 500 MHz spectrometer. MALDI TOF measurements were performed on an Applied Biosystems 4800 BIOiTRAQ instrument using terthiophene as the matrix. Gel permeation chromatography (GPC) was used to determine molecular weight distributions of polymer samples with respect to polystyrene standards (Polymer Laboratories Inc.). Measurements were taken at 35 °C with tetrahydrofuran as mobile phase using three columns (Waters Styragel HR2, HR4, and HR5). Thermal transitions were analyzed using differential scanning calorimetry (DSC) using a TA Instruments DSC Q200 with heating and cooling rates of 10 °C min⁻¹ and 5 °C min⁻¹ respectively. Transmission electron microscopy (TEM) images were obtained using a JEOL 2010F-FastEM. Polymer samples were drop cast onto copper grids from a 0.01% wt solution in chloroform.

Device Fabrication. Bottom contact OFET devices were fabricated on heavily n-doped (Ar, $\rho = 0.001\text{-}0.005\text{ Ohm cm}$) Si with a 300 nm thermal oxide as gate dielectric ($C_i = 1.2 \times 10^{-8}\text{ F/cm}^2$). Source and drain electrodes were patterned using lift off and were comprised of 25 nm Au on a 5 nm Ti adhesion layer. FET channel widths ranged from 30-100 μm with lengths of 4 mm. Prior to polymer deposition, the substrates were

cleaned using UV/ozone and subsequently submerged in a 0.1M toluene solution of octyltrichlorosilane at 70 °C for 30 min. The substrates were then rinsed with toluene, isopropyl alcohol, and dried with N₂. Polymer solutions in CHCl₃ (10 mg/ml) were spincoated at 1500 rpm for 30 seconds. I-V curves were obtained using a Keithly 4200-SCS semiconductor characterization system operating in atmosphere; hole mobilities were calculated in the saturation regime.

Synthesis of 4T-Sn(Bu)₃. To a dry 500 mL flask was added α -quaterthiophene (1.5 g, 4.5 mmol) and 300 mL of dry THF. After sonication the solution was cooled to 0 °C, and *n*-Butyllithium (2.8 mL, 4.5 mmol) was added dropwise via syringe. After stirring for 20 min at 0 °C the solution was warmed to rt and allowed to stir for 1 hr. Tributyltin chloride (1.5 g, 4.6 mmol) was then added to the solution via syringe, and the reaction was stirred overnight. The reaction was quenched with 15 mL of methanol followed by removal of all solvents under reduced pressure. The solid was then collected and washed with 100 mL of cold methanol, and then extracted with 100 mL of cold hexanes. Removal of the hexanes afforded the product (0.9 g, 32%) in approximately 90% purity, which was adequate for subsequent reactions. The remaining 10% was a mixture of unreacted tributyltin chloride and bis(tributyltin) substituted quaterthiophene. ¹H NMR (400 MHz, CDCl₃): δ (ppm) 7.29 (1H, m), 7.22 (1H, d, J = 5 Hz), 7.17 (1H, d, J = 3.3 Hz), 7.07-7.09 (5H, m), 7.03 (1H, dd, J = 5 Hz, 1 Hz), 1.55-1.63 (6H, m), 1.32-1.38 (6H, m), 1.13 (6H, t, J = 8.5 Hz), 0.91 (9H, t, J = 7.3 Hz).

Polymer end-group Stille coupling procedure. The end-functionalized polymers were synthesized by stirring a toluene solution of P3HT, tributylstannyl-oligothiophene, and Pd(PPh₃)₂Cl₂ at 90 °C overnight, and were isolated by precipitation in methanol. For example the procedure for F-P3HT is as follows. A solution of P3HT (0.45 g, 0.11 mmol) in 200 mL dry toluene was prepared in a 500 mL flask equipped with reflux condenser and stir bar. 5-perfluorohexyl-5'-tributylstannyl-2,2'-bithiophene (1.3 g,

1.7 mmol) and $\text{Pd}(\text{PPh}_3)_2\text{Cl}_2$ (0.05 g, 0.07 mmol) were then added and the solution was purged with argon for 30 min. The glassware was then wrapped in aluminum foil to prevent light exposure and the reaction was heated to 90 °C and stirred overnight under argon. The solution was then poured into a mixture of methanol (1.5 L) and water (300 mL) to precipitate the polymer. The product was recovered on a Buchner funnel and washed with copious amount of methanol and hexanes to afford the pure polymer (0.37 g, 76%) as determined by ^1H NMR and ^{19}F NMR. End-group conversion was analyzed using MALDI TOF

References

- 1) Paul, K. E.; Wong, W. S.; Ready, S. E.; Street, R. A. *Appl. Phys. Lett.* **2003**, 83, 2070.
- 2) Sirringhaus, H.; Kawase, T.; Friend, R. H. *MRS Bull.* **2001**, 26, 539
- 3) Arias, A. C.; Ready, S. E.; Lujan, R.; Wong, W. S.; Paul, K. E.; Salleo, A.; Chabinyc, M. L.; Apte, R.; Street, R. A.; Wu, Y.; Liu, P.; Ong, B. *Appl. Phys. Lett.* **2004**, 85, 3304
- 4) Irimia-Vladu, M.; Sariciftci, N. S.; Bauer, S. *J. Mater. Chem.* doi: 10.1039/c0jm02444a
- 5) Jimison, L. H.; Toney, M. F.; McCulloch, I.; Heeney, M.; Salleo, A. *Adv. Mater.* **2009**, 21, 1568
- 6) Zhang, X.; Hudson, S. D.; DeLongchamp, D. M.; Gundlach, D. J.; Heeney, M.; McCulloch, I. *Adv. Funct. Mater.* DOI:10.1002/adfm.201001232
- 7) Rivnay, J.; Jimison, L. H.; Northrup, J. E.; Toney, M. F.; Noriega, R.; Lu, S. F.; Marks, T. J.; Facchetti, A.; Salleo, A. *Nat. Mater.* **2009**, 8, 952
- 8) Bao, Z.; Dodabalapur, A.; Lovinger, A. J. *Appl. Phys. Lett.* **1996**, 69, 4108
- 9) Sirringhaus, H.; Tessler, N.; Friend, R. H. *Science*, **1998**, 280, 1741
- 10) Cho, S.; Lee, K.; Yuen, J.; Wang, G.; Moses, D.; Heeger, A. J.; Surin, M.; Lazzaroni, R. *J. Appl. Phys.* **2006**, 100, 114503
- 11) Osaka, I.; McCullough, R. D. *Acc. Chem. Res.* **2008**, 41, 1202
- 12) Jeffries-El, M.; Sauvé, G.; McCullough, R. D. *Macromolecules* **2005**, 38, 10346
- 13) Liu, J.; McCullough, R. D. *Macromolecules* **2002**, 35, 9882
- 14) Liu, J.; Loewe, R. S.; McCullough, R. D. *Macromolecules* **1999**, 32, 5777
- 15) Facchetti, A.; Yoon, M. H.; Stern, C. L.; Hutchison, G. R.; Ratner, M. A.; Marks, T. J. *J. Am. Chem. Soc.* **2004**, 126, 13480
- 16) Merlo, J. A.; Frisbie, C. D. *J. Polym. Sci. Part B: Polym. Phys.* **2003**, 41, 2674
- 17) Liu, J.; Arif, M.; Zou, J.; Khondaker, S. I.; Zhai, L. *Macromolecules* **2009**, 42, 9390
- 18) Tremblay, N. J.; Gorodetsky, A. A.; Cox, M. P.; Schiros, T.; Kim, B.; Steiner, R.; Bullard, Z.; Sattler, A.; So, W.-Y.; Itoh, Y.; Toney, M. F.; Ogasawara, H.; Ramirez, A. P.; Kymissis, I.; Steigerwald, M. L.; Nuckolls, C. *ChemPhysChem* **2010**, 11, 799
- 19) Cravino, A.; Sariciftci, N. S. *J. Mater. Chem.* **2002**, 12, 1931
- 20) Matharu, A. S.; Cowling, S. J.; Wright, G. *Liq. Cryst.* **2007**, 34, 489
- 21) Pham, C. V.; Burkhardt, A.; Shabana, R.; Cunningham, D. D.; Mark, H.

B.; Zimmer, H. *Phosphorous Sulfur* **1989**, 46, 153

CHAPTER 3

Solution Processable Oligothiophenes for Field Effect Transistors

3.1 Introduction

Solution processable organic semiconductors (OSCs) are attractive for low cost fabrication of electronic devices such as field effect transistors¹ (FETs), light emitting diodes², and photovoltaic cells.³ However, many OSCs are susceptible to degradation through photo-oxidation and/or moisture sensitivity and often have limited device lifetime in atmospheric conditions.^{4,5} For p-type semiconductors, correct energy alignment of the highest occupied molecular orbital (HOMO) level is necessary in order to avoid charge transfer to oxygen. Stability criteria for neutral p-type semiconductors was previously established using the standard redox potentials of water and oxygen⁶; an oxidation potential ≥ 0.5 V vs. SCE (≥ 4.9 eV from vacuum) was determined necessary for air stability.

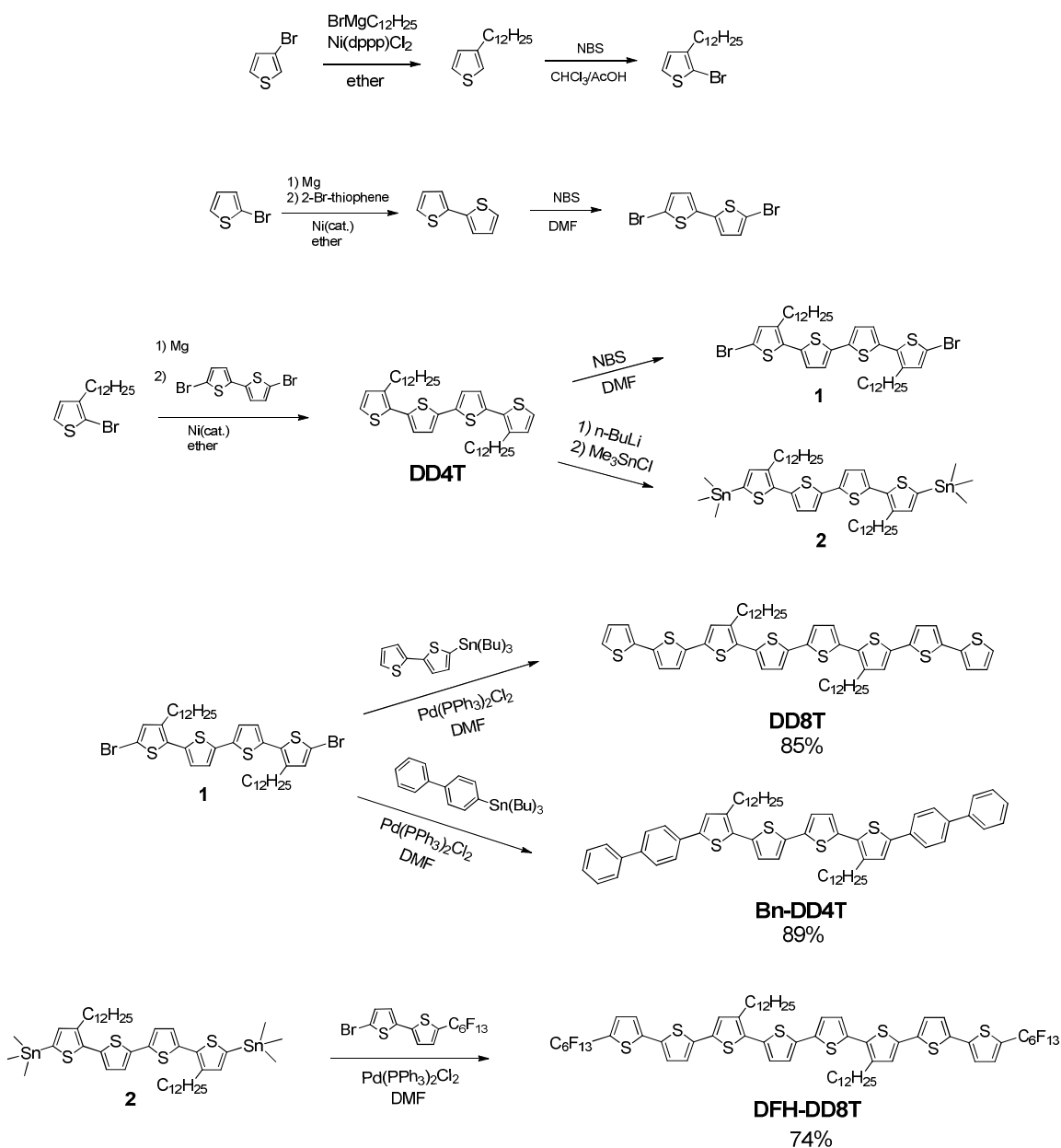
The popular semiconductor poly(3-hexylthiophene) (P3HT) exhibits good solubility as a result of alkyl side chain substitution, but suffers from poor device stability as a result of its relatively high HOMO level near -4.7 eV. Previously, a soluble polythiophene with lower lying HOMO was synthesized by electrochemical polymerization of 3,3''-didodecyl-2,2':5',2'':5'',2'''-quaterthiophene (DD4T). Reduction of the HOMO was achieved by increasing the spacing between electron donating alkyl substituents along the polymer backbone, leading to air stable OFET devices.⁷

Oligothiophenes are also of interest for various electronic technologies since their molecular structures and their morphologies are typically better defined due to their monodispersity. Both unsubstituted and α,ω -substituted oligothiophenes have been extensively studied for applications in field effect transistors. High performance OFETs have been demonstrated using α,ω -dialkyl substituted oligothiophenes with 4-8 thiophene units, with hole mobilities for these materials reaching over $0.1 \text{ cm}^2/\text{Vs}$.⁸⁻¹⁰ However, most of these compounds are insoluble in organic solvents and therefore require vacuum deposition for device fabrication, a technique that devalues the use of organic semiconductors. On the other hand, FET studies employing β -substituted oligothiophenes are relatively scarce in the literature, though these compounds are important building blocks for soluble oligothiophene semiconductors. Furthermore, the FET device stability of β -substituted oligothiophenes has not yet been explored.

This chapter describes the synthesis and characterization of new soluble β -alkylated oligothiophenes stable HOMO levels at or below -5.1 eV. Structure property relationships are examined between three oligothiophenes including a soluble octithiophene with α,ω -perfluorohexyl groups. Bottom contact field effect transistors employing the new materials have been characterized, and the stability of the devices is discussed. These studies further explore the effects of perfluoroalkylation on thiophene based semiconductors.

3.2 Synthesis and Characterization

The synthesis of the oligomers began with the construction of a dodecyl substituted quaterthiophene core. Dodecyl substituents were chosen to ensure solubility of the larger π -conjugated systems. Compounds **1** and **2** were synthesized in six steps



Scheme 3.1 Synthetic route for oligomers DD8T, Bn-DD4T and DFH-DD8T

following procedures in the literature. The oligothiophenes were completed by Stille coupling between either **1** or **2** and the corresponding aromatic halide or stannane as outlined in Scheme 3.1. Reactions were carried out in DMF which allowed for soluble intermediates but led to precipitation of the products. The crude products were red powders that were further purified by re-precipitation.

The three oligomers were characterized by ^1H NMR and elemental analysis (see Appendix). The aromatic region of Bn-DD4T shows the presence of $\approx 10\%$ impurities. Re-precipitation was not successful at removing these impurities and the data presented for Bn-DD4T corresponds to the compound in $\approx 90\%$ purity. Purity of DD8T and DFH-DD8T was much higher (98-99%). The aromatic protons of DFH-DD8T are shifted slightly downfield compared to DD8T, a result of the electron withdrawing effects of the perfluoroalkyl substituents. DFH-DD8T was also characterized by ^{19}F NMR and showed the six expected signals from the perfluorohexyl groups, further verifying the compounds purity.

3.3 Thermal Properties

Thermal transitions of the oligomers were evaluated using DSC (Figure 3.1). Upon, first heating of DD8T an exotherm is observed around $85\text{ }^\circ\text{C}$, indicating crystallization upon heating. This can be explained by reorganization of the amorphous portion of DD8T following a glass transition that is observed around $50\text{ }^\circ\text{C}$ in the second heating. DD8T then melts at $117\text{ }^\circ\text{C}$. The melting point of DFH-DD8T is very close to that of DD8T at $116\text{ }^\circ\text{C}$. This indicates similar π - π interactions for these two oligomers, since π - π interactions are expected to dominate the cohesive forces in these crystals. Unlike DD8T the perfluoroalkylated oligomer melts into a mesophase at $116\text{ }^\circ\text{C}$ and clears to isotropic at $140\text{ }^\circ\text{C}$. The liquid crystal phase of DFH-DD8T, reminiscent of a smectic phase, appeared very stable and could be observed using polarized optical microscopy both during heating and cooling (Figure 3.2). Bn-DD4T melts at $137\text{ }^\circ\text{C}$, much higher than the other oligomers. Therefore, the biphenyl end groups appear to increase the cohesive forces of the π -system.

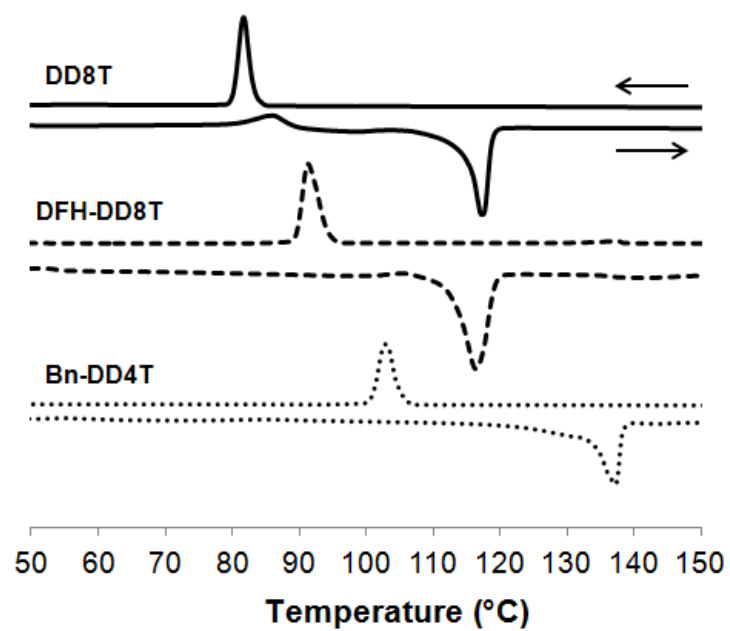


Figure 3.1 First heating/cooling DSC thermograms of oligomers (endo is down)

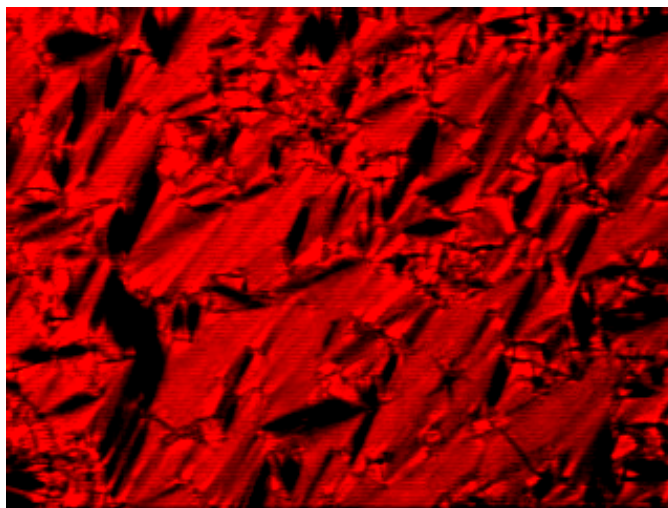


Figure 3.2 Polarized optical microscope image of DFH-DD8T at 130 °C

3.4 Optical/Electrochemical Properties

All three oligomers are red solids, a result of their similar degrees of conjugation. Figure 3.3 shows DD8T illuminated under 420 nm irradiation. The solution and film UV/vis spectra of the three oligomers are shown in Figure 3.4. Compounds DD8T and DFH-DD8T have almost identical spectra in solution, with maxima at 442 nm. Compound Bn-DD4T has a slightly blue shifted absorbance with maximum at 420 nm. This is due to the greater torsion angles in the biphenyl system compared to bithiophene which reduces conjugation and leads to a larger band-gap.



Figure 3.3 Image of DD8T in THF solution (left) and as powder (right) under 420 nm irradiation

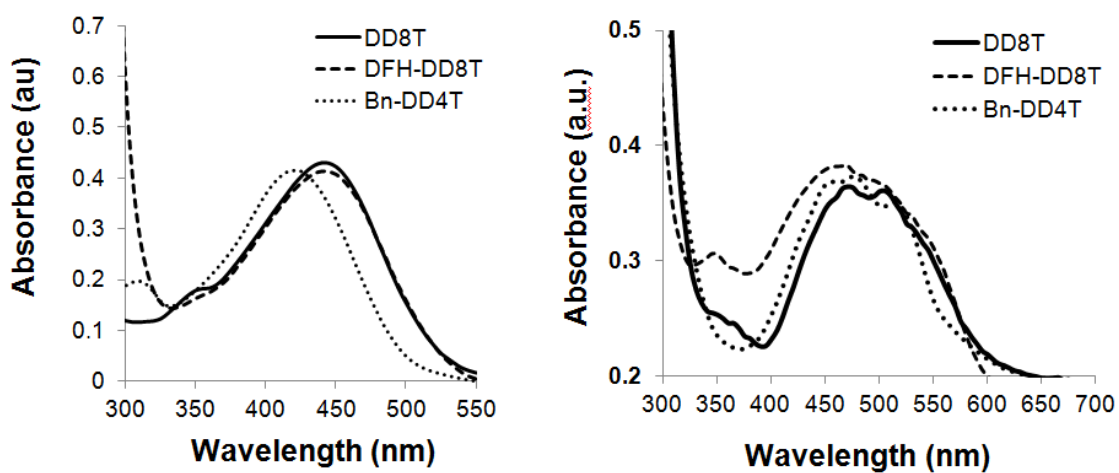


Figure 3.4 UV/vis spectra of the three oligomers in solution (left) and as films (right)

Film spectra show red-shifted absorbance with vibronic coupling for all three oligomers. This indicates an ordered film with increased planarity of the backbone and significant intermolecular interactions. Band gaps of the three oligomers were calculated from the shoulder of the film spectra, giving 2.2 eV for DD8T and DFH-DD8T and 2.4 eV for Bn-DD4T.

Fluorescence quantum yields were measured for DD8T and DFH-DD8T since previous studies found that α,ω -perfluoroalkylation significantly increased the quantum yields of α -oligothiophenes.¹¹ For the compounds studied here perfluoroalkylation had little effect on the quantum yield, with DD8T having Φ_f of 0.38 and DFH-DD8T having Φ_f of 0.40. These quantum yields are significantly lower than those found for α,ω -perfluoroalkylated oligothiophenes without β -alkyl substituents,¹¹ where α,ω -perfluorohexyl-sexithiophene had $\Phi_f \approx 1.0$. The alkyl substituents in these octithiophenes

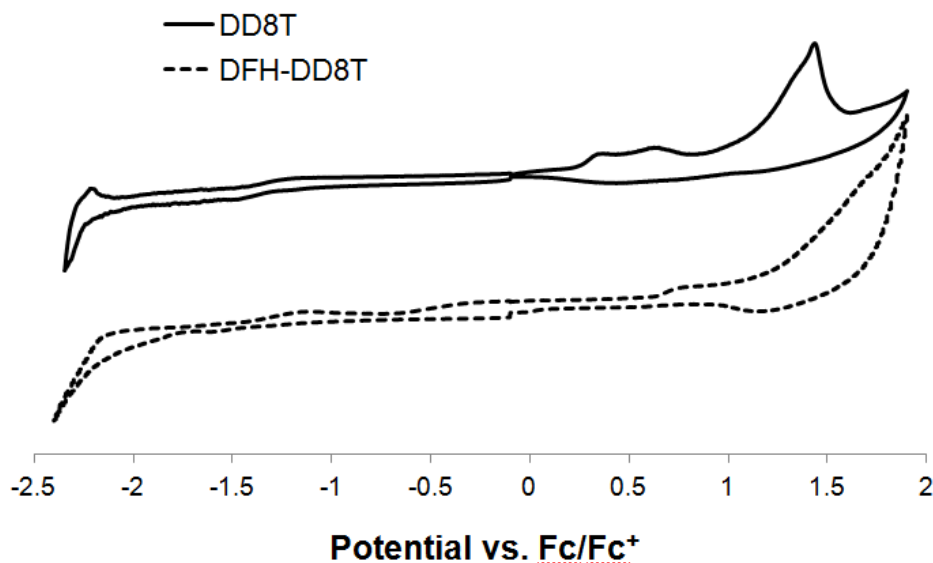


Figure 3.5 Cyclic voltammograms of DD8T and DFH-DD8T

leads to increased non-radiative decay, which is related to the relative positioning of the singlet and triplet manifolds as well as the vibronic relaxation available to the compound.

Cyclic voltammetry was used to study the HOMO and LUMO levels of DD8T and DFH-DD8T (Figure 3.5). The frontier molecular, calculated from the onset of oxidation are given in Table 3.1. The electrochemical and optical band gaps are in good agreement. The HOMO level of DD8T is -5.04 eV, approximately 0.15 eV lower than that of P3HT. Theoretically a p-type semiconductor must have HOMO level below -4.9 eV in order to be stable toward oxidation in atmospheric conditions.¹² Thus, DD8T is expected to have improved stability compared to P3HT. Perfluoroalkylation significantly lowered both the HOMO and LUMO of DFH-DD8T. This is in contrast to the $\alpha\omega$ T series previously studied, where α,ω -perfluoroalkylation had a much stronger effect on the LUMO energy than the HOMO energy.¹¹ The low lying HOMO level of DFH-DD8T is expected to impart good stability to the semiconductor, but will also increase the hole injection barrier from gold electrodes.

The HOMO level of Bn-DD4T was determined using ultraviolet photoelectron spectroscopy to be -5.20 eV. The HOMO of Bn-DD4T is lower than that of DD8T due to

Table 3.1 Optical /Electrochemical data

Compound	$\lambda_{\text{abs, THF}}$ (nm)	$\lambda_{\text{abs, film}}$ (nm)	E_g^{opt} (eV) ^a	HOMO (eV)	LUMO (eV)	E_g^{CV} (eV)
DD8T	442	472	2.2	-5.04	-2.86	2.18
DFH-DD8T	442	472	2.2	-5.44	-3.26	2.18
Bn-DD4T	420 ^b	478	2.4	-5.20 ^c	-2.80 ^d	-

^aEstimated from the low energy shoulder of the film spectra. ^b Maximum in CHCl₃.

^cDetermined using ultraviolet photoelectron spectroscopy. ^dEstimated from the HOMO plus optical band gap.

reduced conjugation as a result of the twisted biphenyl groups. Bn-DD4T is thus expected to be a stable semiconductor, and like DD8T have a relatively small hole injection barrier.

3.5 Density Functional Theory (DFT) Calculations

Charge transport in organic films relies on hopping from one molecule to another and therefore depends on molecular orbital overlap. Density functional theory simulations are helpful for understanding molecular orbital energies and orbital geometries in organic semiconductors. Orbital geometry simulations can provide which parts of a molecule have significant electron density in the frontier orbitals that participate in charge transport.

Figure 3.6 displays the calculated HOMO orbitals for the three oligomers. The HOMO orbital of DD8T shows little contribution from sulfur, with electron density that extends over all eight thiophene rings. Contribution from the core quaterthiophene is greatest as electron density diminishes towards the periphery. The HOMO orbital of DFH-DD8T shows an almost identical geometry as DD8T but with faster diminishing electron density at the peripheral bithiophenes. Considering only the orbital geometries of these two compounds similar charge transport properties of DD8T and DFH-DD8T are expected. The calculations predict the HOMO of DFH-DD8T to be 0.3 eV lower than that of DD8T, in close agreement with the electrochemistry data.

The HOMO orbital of Bn-DD4T is almost completely concentrated on the core quaterthiophene. This is a result of the large torsion angles that the phenyl rings impart, limiting full conjugation to the oligomer core. This leads to a lower HOMO energy than DD8T and a calculated band gap of 3.0 eV (Table 3.2), significantly larger than the other oligomers.

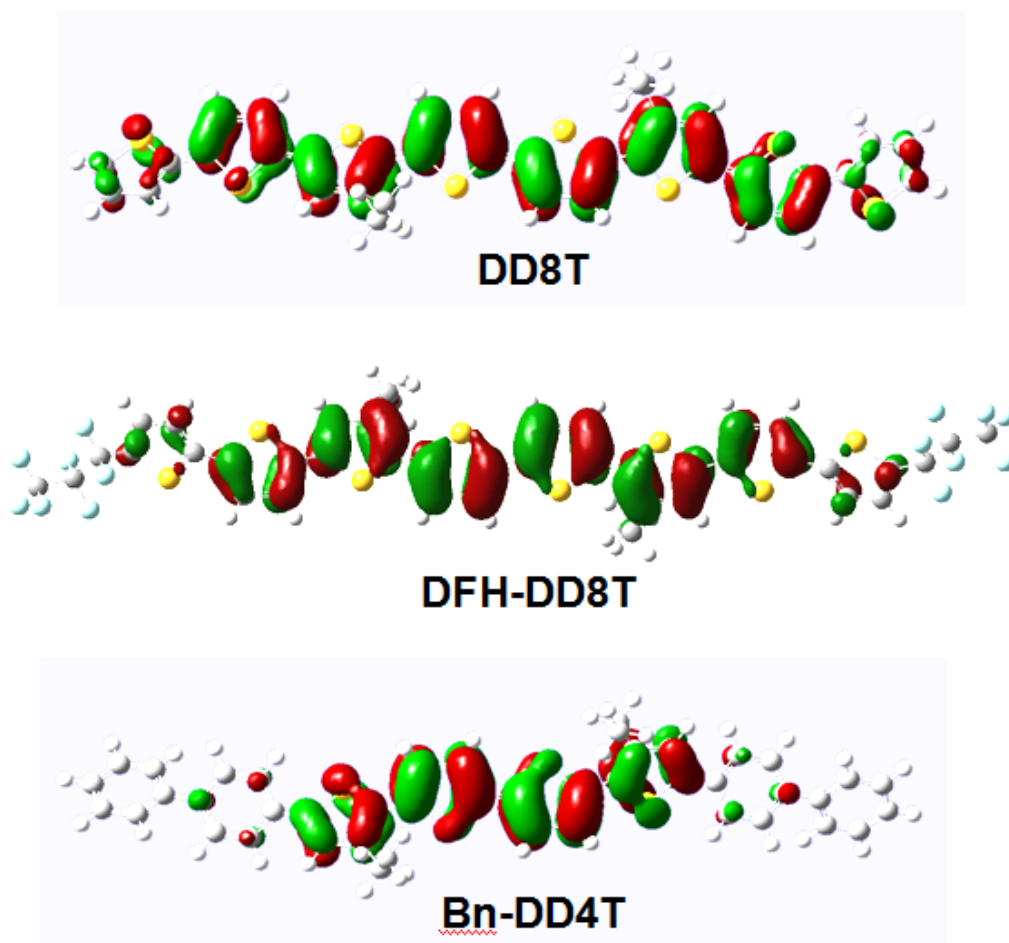


Figure 3.6 Calculated HOMO geometries for the three oligomers

The LUMO orbitals of all three oligomers are quinoidal with significant contribution from sulfur, a common characteristic of oligothiophenes (Figure 3.7). Compared to DD8T the LUMO of perfluoroalkylated DFH-DD8T has a more balanced extension over the eight thiophene rings. Whereas the LUMO of DD8T diminishes towards the periphery, the electron withdrawing perfluoroalkyl groups pull electron density to the external thiophene rings. This stabilizes the LUMO by 0.33 eV. Therefore, the calculations predict almost identical reductions in HOMO and LUMO energies for the transition DD8T \rightarrow DFH-DD8T.

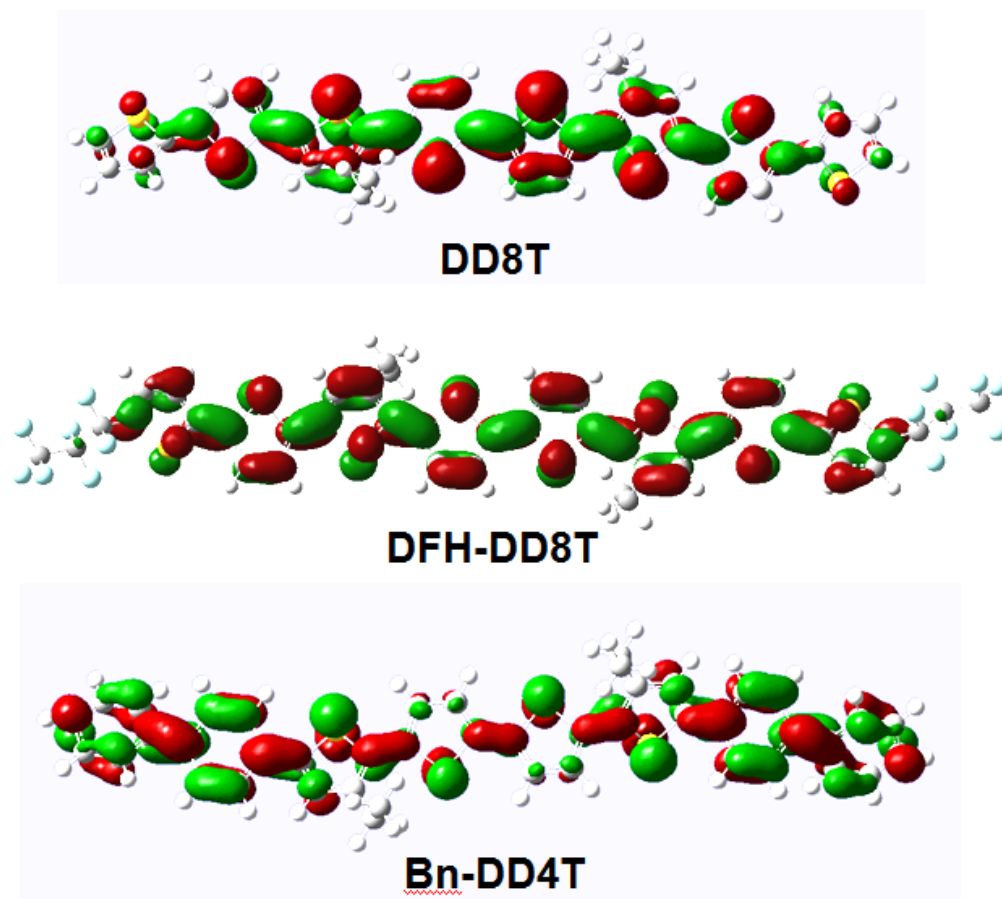


Figure 3.7 Calculated LUMO geometries for the three oligomers

Interestingly the LUMO of Bn-DD4T is shifted towards the exterior biphenyl rings. Even without heteroatoms the biphenyl groups act as electron acceptors in Bn-DD4T. However, the LUMO energy of Bn-DD4T is still higher than DD8T by about 0.2 eV as a result of the reduced conjugation across the eight aromatic rings.

Table 3.2 Calculated HOMO and LUMO energies

Compound	HOMO (eV)	LUMO (eV)	E _g (eV)
DD8T	-5.08	-2.39	2.70
DFH-DD8T	-5.38	-2.72	2.66
Bn-DD4T	-5.20	-2.20	3.0

3.6 Morphological Properties

The morphology of organic thin films is known to significantly impact the charge transport properties by affecting molecule-molecule interactions in the bulk as well as the number and nature of grain boundaries. The morphology of DD8T films was studied in depth using x-ray diffraction (XRD) as well as scanning electron microscopy (SEM). First the powder was analyzed by XRD, showing two peaks at 3.66° and 23.90° (Figure 3.8). The first peak corresponds to an intermolecular distance of 2.4 nm and is attributed to the distance between two DD8T chains, separated by alkyl chains. This indicates that the alkyl chains are interdigitated, since one extended dodecyl chain is approximately 1.5 nm in length. Interdigitation of alkyl chains is not observed for P3HT, and is a result of: 1) longer alkyl chain length in DD8T which aids crystallization and 2) greater separation between alkyl chains in DD8T allowing for improved packing. The second peak corresponds to a distance of 0.37 nm and is attributed to the π - π stacking distance. This is a relatively small π - π distance and suggests good electronic interactions in this direction.

Previously the single crystal structure of the quaterthiophene core DD4T (Scheme 3.1) was determined by x-ray analysis. Crystals of **DD4T** were shown to exhibit unique molecular packing, with a layered structure comprised of slip-stacked oligothiophene backbones.¹³ All of the oligothiophene backbones were found to be parallel within the crystal. The interlayer spacing between the conjugated backbones was only 3.45 Å, indicating a tightly packed structure. This is significantly different than the more common herringbone structures of unsubstituted oligothiophenes.¹⁴ Dodecyl side chains were found to lie in the plane of the conjugated backbone and were interdigitated. These findings are pertinent to DD8T which exhibits the same core structure and likely assembles into a similar solid state structure.

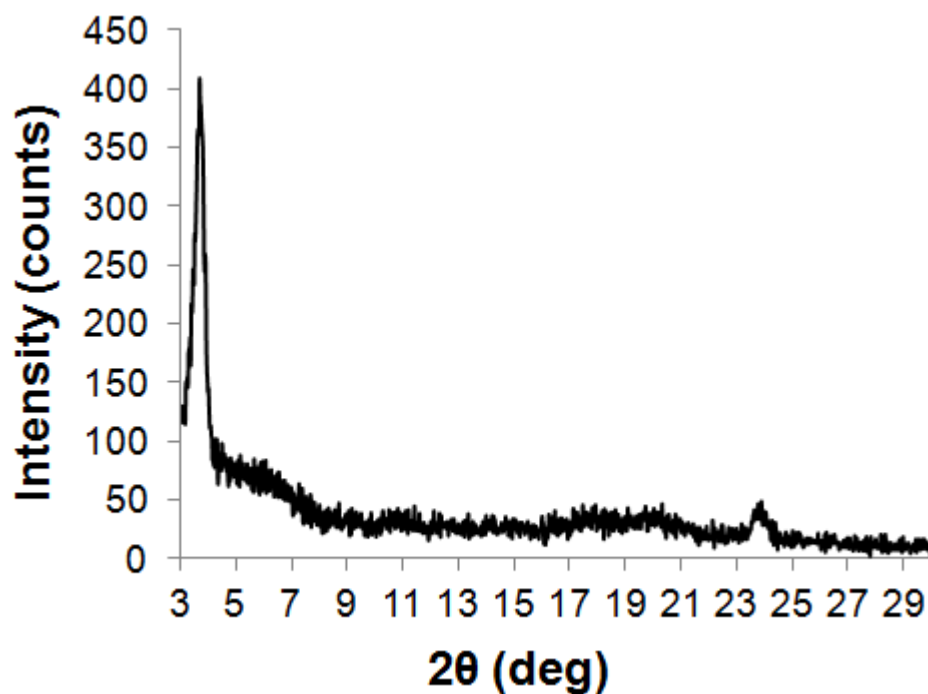


Figure 3.8 Powder diffractogram of DD8T

Thin films of DD8T were prepared by spincoating a 10 mg/ml CHCl_3 solution onto an octyltrichlorosilane (OTS) treated silicon wafer. The OTS treatment was performed in order to replicate the conditions used later for field effect transistor fabrication. The pristine thin films showed morphology comprised of a network of fibers approximately 100 nm in width and between 0.5-1.0 μm in length (Figure 3.9). There were no peaks in the grazing incidence XRD diffractogram of the pristine film, indicating a primarily amorphous film. The film was then annealed at 90 $^{\circ}\text{C}$ under vacuum. This temperature was chosen because it lies above the crystallization exotherm observed in the first heating DSC thermogram but below the melting point of DD8T. Annealing above the melting point is undesirable as it can lead to de-wetting of the surface. The annealed film showed a different morphology comprised of terrace like grains with far fewer grain boundaries. In addition, a peak was observed in the grazing incidence diffractogram, corresponding to a d -spacing of 1.7 nm. This d -spacing is shorter than the spacing

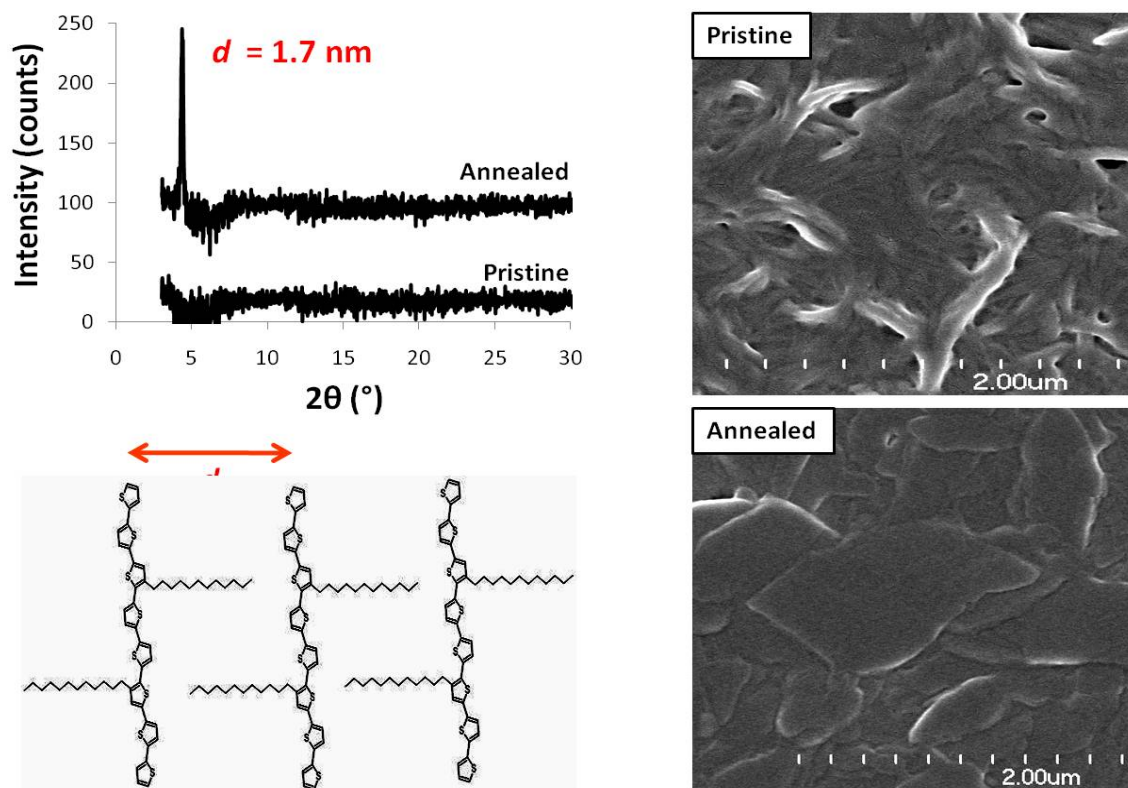


Figure 3.9 Grazing incidence diffractograms and SEM images of pristine/annealed DD8T films

observed in the powder diffractogram. Therefore, the annealing step leads to further interdigitation of the alkyl chains, decreasing the distance between neighboring DD8T molecules. Overall the annealing step leads to a morphology that is more ideal for charge transport.

The effects of annealing films of DD8T were compared to DFH-DD8T using polarized optical microscopy. For these experiments the compounds were dropcast from a 5 mg/ml solution in THF and then imaged under a polarized optical microscope (POM). The POM images show small crystallites with poor connectivity for the pristine dropcast films of both DD8T (Figure 3.10 a) and DFH-DD8T (Figure 3.10 b). The pristine film of DFH-DD8T could not be observed when the polarizers were crossed and was therefore primarily amorphous. The image in Figure 3.10 c was taken without crossed polarizers.

Films were then annealed to 160 °C for 10 min under vacuum in order to study the differences in crystallization behavior from the melt. The annealed DD8T film showed larger crystalline grains but poor connectivity between grains. On the other hand the annealed film of DFH-DD8T showed exceptional long range order, with less drastic grain boundaries. This was a result of DFH-DD8T being cooled through its mesophase, which imparts mesoscale ordering and reduces the severity of grain boundaries within the film. Previous reports in the literature have demonstrated this mesophase ordering as a

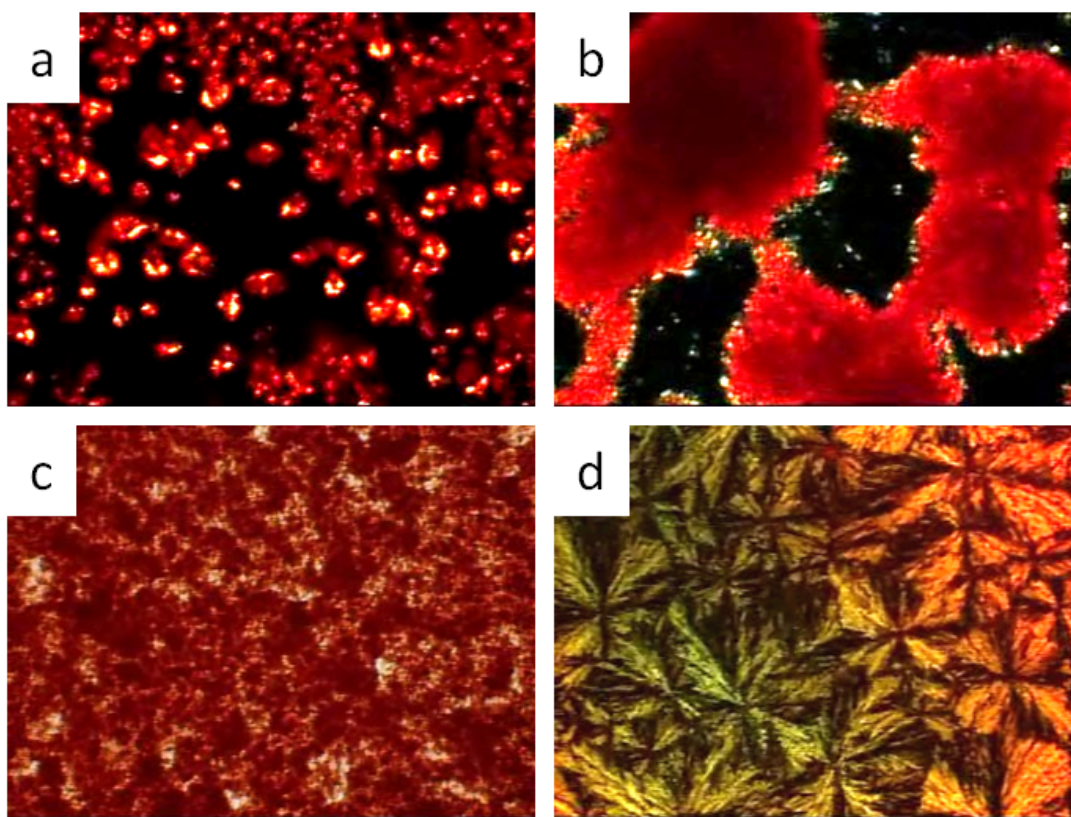


Figure 3.10 Polarized optical microscope images of DD8T (top) and DFH-DD8T (bottom) as pristine dropcast films (left) and after annealing at 90 °C for 10 min (right). Image c was taken without polarizers crossed

method for improving charge transport in FETs.⁷ The capability of DFH-DD8T to form highly ordered films could therefore be advantageous for electronic applications.

3.7 Field Effect Transistor Characterization

Bottom-contact bottom-gate field effect transistors were fabricated by spin-casting a 10 mg/ml solution of each oligomer onto an OTS treated silicon wafer. Devices were then measured in air while blowing a stream of nitrogen over the transistor channel. For pristine DD8T devices the average hole mobility was $4.7 \times 10^{-4} \text{ cm}^2/\text{Vs}$, with on/off ratio of 5×10^3 and threshold voltage of -15 V. Annealing the devices at 90 °C resulted in significant improvement in device performance. The average hole mobility for annealed devices was $2.8 \times 10^{-3} \text{ cm}^2/\text{Vs}$ with on/off ratios of 5×10^4 and threshold voltage of -11 V. The improvement in charge mobility upon annealing is consistent with the observed changes in morphology. The output and transfer characteristics of annealed DD8T devices are shown in Figure 3.11. Some contact resistance can be observed in the output curves, seen as a deviation from linearity at low source-drain voltage. Good saturation behavior is observed in the output characteristics for DD8T;

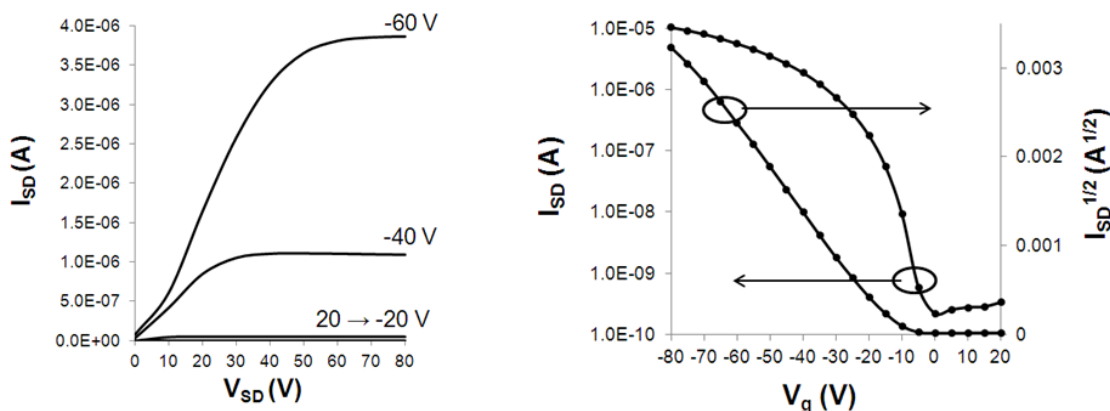


Figure 3.11 Output (left) and transfer (right) characteristics of DD8T devices

however, some deviation from linearity can be seen at low V_{SD} indicating contact resistance. The relatively low negative threshold voltage is a result of the closely matched work function of gold and the HOMO energy of DD8T. This is a substantial improvement over P3HT which showed threshold voltages as high as positive 60 V. This implies that the HOMO energy cut-off for stable p-type semiconductors is between -4.9 to -5.0 eV, consistent with theoretical predictions.¹²

The stability of DD8T devices was examined further by testing a single FET device over the course of one month. Figure 3.12 shows the transfer characteristics of the fresh device and the device after storage in ambient atmosphere for one month. Little change is observed in the off current after storage in air for 30 days, indicating the good stability of DD8T toward oxidation. However, it should be noted that off currents for DD8T devices were an order of magnitude higher when nitrogen was not blown over the

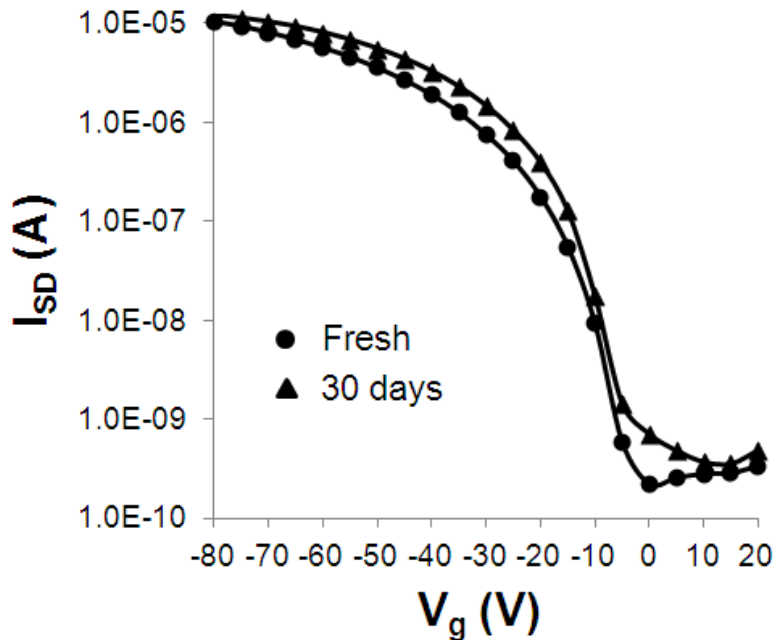


Figure 3.12 Transfer characteristics of a fresh DD8T FET and a device stored in air for 30 days

channel during operation. The reversibility of this change in off current indicates that it is not a result of oxidation of the polymer, but likely due to adsorbed H₂O/O₂ on the surface of the film or at exposed dielectric. This type of device degradation may be avoided by encapsulation.

No field effect behavior could be observed when DFH-DD8T was employed in devices. Devices were annealed through the mesophase in order to improve thin film morphology, still there was no transistor behavior. The lack of transistor behavior for DFH-DD8T is most likely a result of a large charge injection barrier due to the lower lying HOMO (-5.44 eV) for the perfluoroalkylated compound.

Devices fabricated using Bn-DD4T showed similar p-type behavior as DD8T (Figure 3.13). The average hole mobilities calculated for pristine films of Bn-DD4T were $2.3 \times 10^{-4} \text{ cm}^2/\text{Vs}$ with on/off ratios of $\approx 10^3$ and threshold voltage of -15 V. The device characteristics were therefore very similar to those of pristine DD8T films. Apparently the confined HOMO orbital of Bn-DD4T does not significantly affect charge mobility. This is an indication that hole transport from one molecule to another occurs mainly within the quaterthiophene core for both DD8T and Bn-DD4T. The stability of Bn-DD4T devices

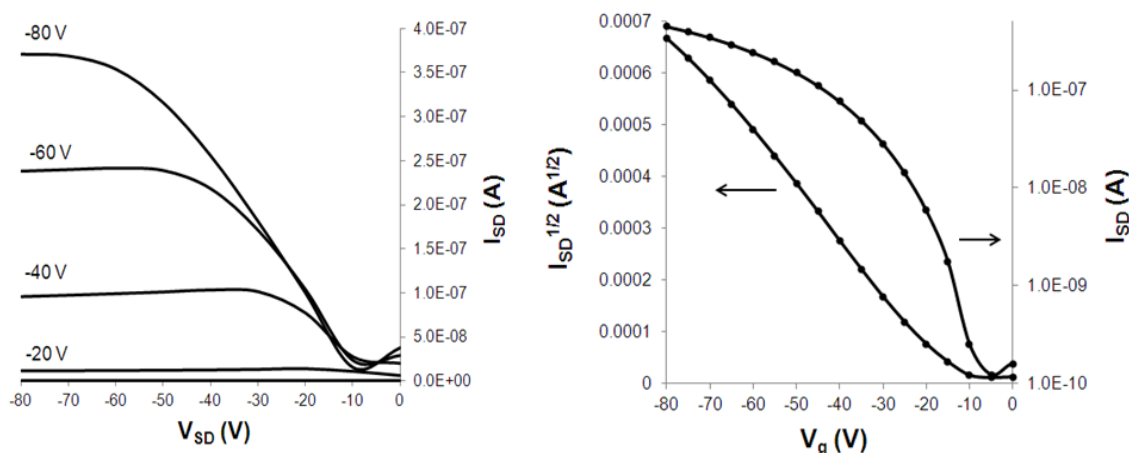


Figure 3.13 Output (left) and transfer (right) characteristics of Bn-DD4T devices

was examined over the course of a week, showing no degradation in transfer characteristics. This was expected due to the lower HOMO of Bn-DD4T At -5.2 eV.

3.8 Conclusion

Three new soluble oligothiophenes were studied for applications in solution processable field effect transistors. A new octithiophene DD8T showed hole mobilities up to $3.3 \times 10^{-3} \text{ cm}^2/\text{Vs}$ and could be stored in air for one month without degradation in device performance. The stability of DD8T devices was attributed to the HOMO level of -5.04 eV, which lies below the stability cut-off for neutral p-type semiconductors. Annealing DD8T films led to improved FET device performance which was related to changes in the morphology of the oligomer. α,ω -Perfluoroalkylation of the octithiophene led to a mesophase which was used to significantly increase the long range order within thin films. However, DFH-DD8T did not show field effect behavior in transistor devices. This is presumably due to a high hole injection barrier as a result of the oligomer's low lying HOMO level and electron deficient periphery.

The substitution of peripheral bithiophene groups for biphenyl groups led to a reduction in conjugation of the π -system, affording a HOMO orbital concentrated on the quaterthiophene core. However, this did not affect FET device performance. Transistors made using Bn-DD4T could also be stored in air without degradation of the transfer characteristics.

Compounds DD8T and Bn-DD4T are useful semiconductors for solution processable transistors due to their high solubility and good FET characteristics. In addition this series of oligomers has shed light upon structure property relationships within oligothiophenes, and will help aid the future design of soluble semiconductors. Improvements in charge mobilities may be possible through incorporation of fused aromatic rings which have extended π -orbitals and good π - π overlap in the solid state.

Furthermore, while compounds DD8T and Bn-DD4T were air stable in terms of storage, materials that retain low off currents while operating in air are desirable. Air stable OFET operation has been observed in some polymers¹⁵ and is likely related not only to orbital energetics, but also to the degree of pinholes in the thin film which can allow migration of H₂O and O₂ to the dielectric surface. Thus the design of air-stable materials for FETs should also consider morphological characteristics.

3.9 Experimental

Materials. All chemicals were purchased from Aldrich and used as received unless otherwise noted. [2,2'-bithiophen]-5-yltributylstannane¹⁶, 5-(tri-*n*-butylstannyl)-5'-perfluorohexyl-2,2'-bithiophene¹¹, 5,5'''-dibromo-3,3'''-didodecyl-2,2':5',2'':5'',2'''-quaterthiophene,¹⁷ 5,5'''-bis(tri-*n*-butylstannyl)-3,3'''-didodecyl-2,2':5',2'':5'',2'''-quaterthiophene,¹⁸ and (4-biphenyl)tributylstannane¹⁹ were synthesized according to procedures in the literature.

Instrumentation. NMR characterization was carried out using either a Bruker 300 MHz or 500 MHz instrument. UV/vis spectra were acquired using a Varian Cary 50 UV/Vis spectrometer. Cyclic voltammetry was performed using a Bioanalytical Systems (BAS) Epsilon potentiostat equipped with a standard three-electrode configuration. Scans were performed on oligomer films evaporated onto a glassy carbon electrode which served as the working electrode. A Pt wire was used as counter electrode and an Ag/AgNO₃ (0.01 M in anhydrous acetonitrile) was used as the reference electrode. Measurements were performed in anhydrous acetonitrile with tetrabutylammonium hexafluorophosphate (0.1 M) as supporting electrolyte under nitrogen at a scan rate of 100 mV/s. Internal calibration of the reference potential was achieved using the ferrocene/ferrocenium redox couple. Melting points and thermal transitions were analyzed using a TA instruments Q200 differential scanning calorimeter. SEM images of

DD8T films were taken from devices that had an additional 2.0 nm Au/Pd film sputtered over the film. Images were obtained using a Hitachi S-4700 cold cathode field emission microscope. DFT calculations for DD8T and DFH-DD8T were performed at the B3LYP/6-311+G* level of theory. Dodecyl and perfluorohexyl chains were substituted for propyl and perfluoropropyl chains, respectively, in order to reduce computational time.

Grazing incidence XRD was carried out using a Rigaku Multiflex Diffractometer. The angle of incidence was held at 2.8 while the 2θ was scanned between 3-40° at 5°/min. Films were spincoated onto an octyltrichlorosilane treated silicon oxide wafer. The wafer was cleaned using UV/ozone, and then submerged into a 0.1M solution of octyltrichlorosilane in toluene at 70 °C for 30 min. A solution of **DD8T** in CHCl_3 (10 mg/ml) was then spincoated at 1000 rpm for 20 seconds.

Device Fabrication. Bottom contact OFET devices were fabricated on heavily n-doped (Ar, $\rho = 0.001\text{-}0.005\text{ Ohm cm}$) Si with a 300 nm thermal oxide as gate dielectric ($C_i = 1.2 \times 10^{-8}\text{ F/cm}^2$). Source and drain electrodes were patterned using lift off and were comprised of 25 nm Au on a 5 nm Ti adhesion layer. FET channel widths ranged from 30-100 μm with lengths of 4 mm. Prior to polymer deposition, the substrates were cleaned using UV/ozone and subsequently submerged in a 0.1M toluene solution of octyltrichlorosilane at 70 °C for 30 min. The substrates were then rinsed with toluene, isopropyl alcohol, and dried with N_2 . Oligomer solutions in CHCl_3 (10 mg/ml) were spincoated at 1500 rpm for 30 seconds. I-V curves were obtained using a Keithly 4200-SCS semiconductor characterization system operating in atmosphere; hole mobilities were calculated in the saturation regime.

Synthesis.

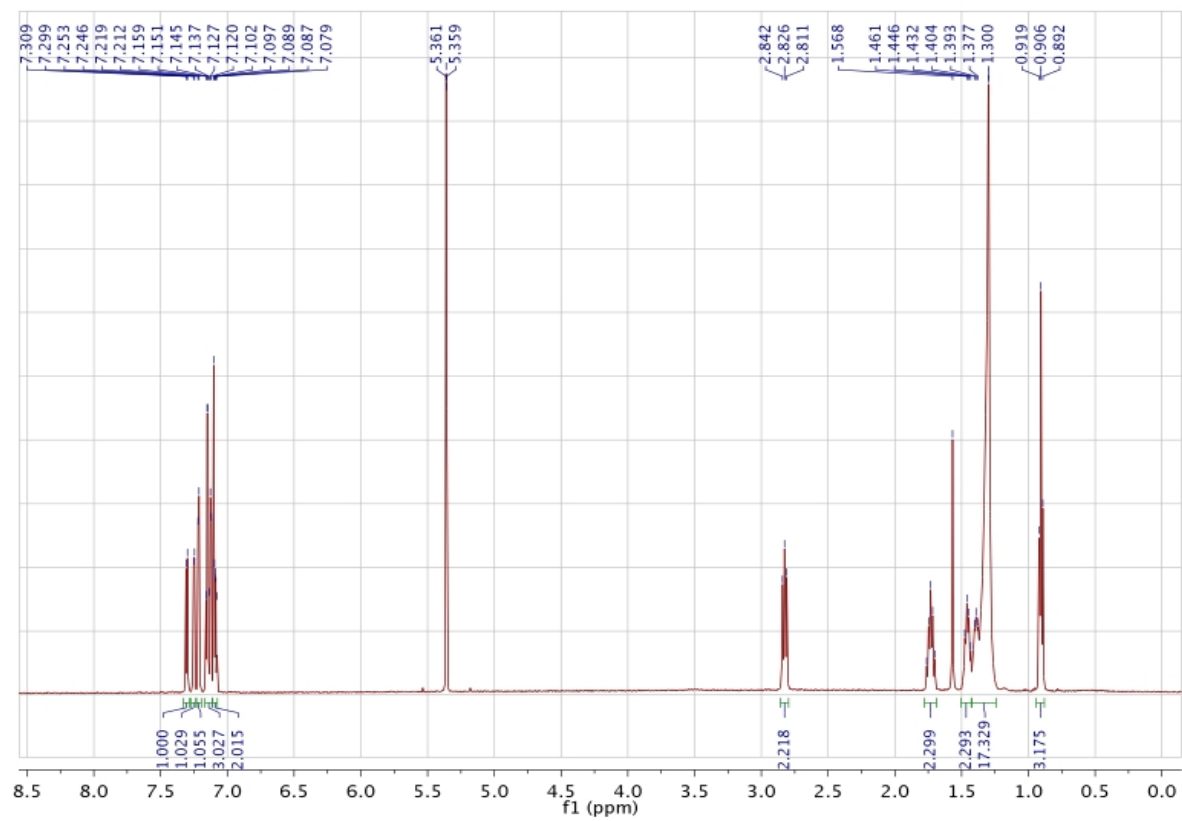
3''',4''-didodecyl-2,2':5,2'':5'',2''':5''',2''':5''',2''':5''',2''':5''',2''':5'''-octithiophene (DD8T). To a 100 mL round bottom flask was added 5,5'''-dibromo-3,3'''-didodecyl-2,2':5,2'':5'',2''':5'''-quaterthiophene (0.5 g, 0.61 mmol), [2,2'-bithiophen]-5-yltributylstannane

(0.83 g, 1.82 mmol), Pd(PPh₃)₂Cl₂ (0.029 g, 0.04 mmol) and 50 mL anhydrous DMF. The solution was purged with argon for 30 min, then brought to 85 °C and stirred overnight. The reaction was cooled over ice and filtered to collect the red precipitate. The product was purified by dissolving in methylene chloride and slowly precipitating the compound by addition of methanol. The resulting precipitate was collected by filtration and dried under vacuum to give the pure product as a bright red solid (0.51 g, 85%). ¹H NMR (500 MHz, CD₂Cl₂): δ (ppm) 7.30 (2H, d, J = 5.0 Hz), 7.25 (2H, d, J = 3.5 Hz), 7.22 (2H, d, J = 3.5 Hz), 7.14-7.16 (4H, m), 7.12 (2H, d, J = 3.5 Hz), 7.1 (2H, s), 7.09 (2H, dd, J = 4, 5 Hz), 2.83 (4H, t, J = 7.5 Hz), 1.73 (4H, p), 1.30-1.48 (36H, m), 0.91 (6H, t, J = 7.0 Hz). Elemental analysis calculated for C₅₆H₆₆S₈: C, 67.55, H, 6.68%. Found: C, 67.76, H, 6.49%.

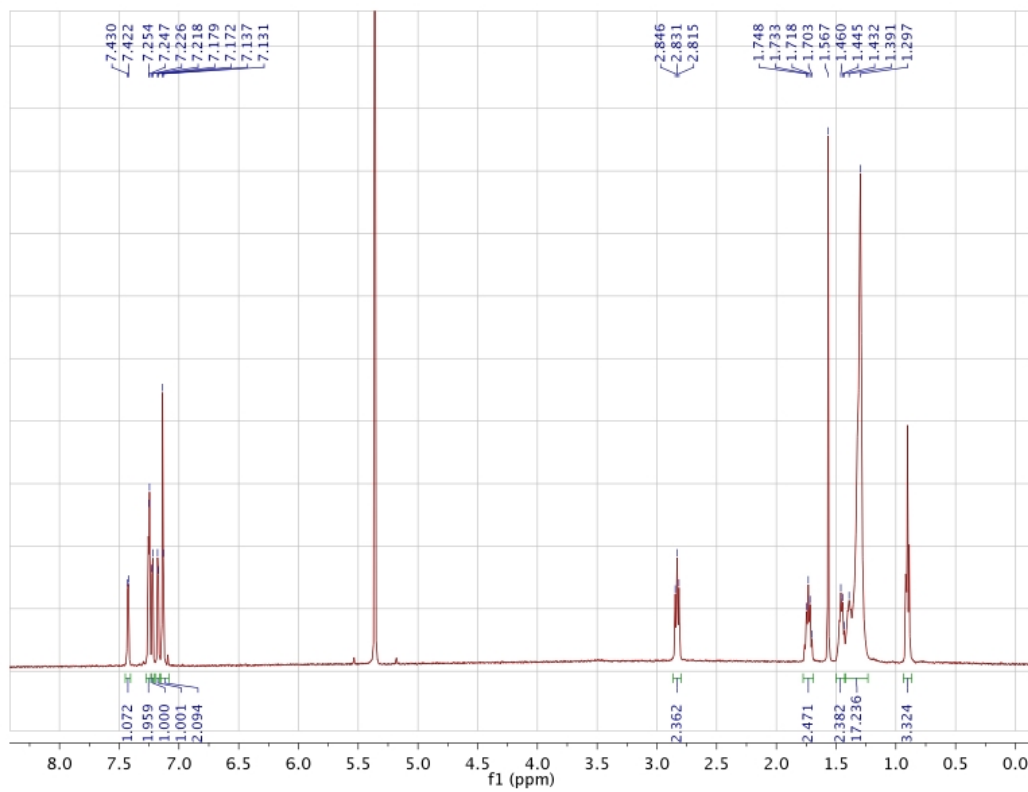
3''',4''-didodecyl-(5,5''''-diperfluorohexyl)-2,2':5',2'':5'',2''':5''',2''':5''',2''':5''',2''':5''''-octithiophene (DFH-DD8T). To a 25 mL round bottom flask was added 5,5'''-bis(tri-*n*-butylstannyl)-3,3'''-didodecyl-2,2':5',2'':5'',2'''-quaterthiophene (0.25 g, 0.25 mmol), 5-bromo-5'-perfluorohexyl-2,2'bithiophene (0.43 g, 0.76 mmol), Pd(PPh₃)₄ (0.013 g, 0.011 mmol) and 15 mL anhydrous DMF. The solution was purged with argon for 30 min, then brought to 85 °C and stirred overnight. The reaction was cooled over ice and filtered to collect the red precipitate. The product was purified by dissolving in methylene chloride and slowly precipitating the compound by addition of methanol. The resulting precipitate was collected by filtration and dried under vacuum to give the pure product as a bright red solid (0.30 g, 74%). ¹H NMR (500 MHz, CD₂Cl₂): δ (ppm) 7.43 (2H, d, J = 4.0 Hz), 7.25 (4H, d, J = 3.5 Hz), 7.22 (2H, d, J = 4 Hz), 7.18 (2H, d, J = 3.5 Hz), 7.13-7.14 (4H, m). ¹⁹F NMR (500 MHz, CD₂Cl₂): δ (ppm) -81.1 (6F, b), -101.5 (4F, b), -121.6 (4F, b), -121.8 (4F, b), -123.0 (4F, b), -126.4 (4F, b). Elemental analysis calculated for C₆₈H₆₄F₂₆S₈: C, 50.06, H, 3.95, F, 30.27%. Found: C, 50.20, H, 3.98, F, 30.20%.

3'''',4-didodecyl-(5,5'''-di-1,4-biphenyl)-2,2':5',2'':5'',2'''-quaterthiophene (*Bn-DD4T*). To a 50 mL round bottom flask was added (4-biphenyl)tributylstannane (0.48 g, 1.1 mmol), 5,5'''-dibromo-3,3'''-didodecyl-2,2':5',2'':5'',2'''-quaterthiophene (0.3 g, 0.36 mmol), Pd(PPh₃)₂Cl₂ (0.02 g, 0.03 mmol) and 18 mL anhydrous DMF. The solution was purged with argon for 30 min, then brought to 100 °C and stirred overnight. The reaction was cooled over ice and filtered to collect the red precipitate. The product was purified by dissolving in chloroform and slowly precipitating the compound by addition of methanol. The resulting precipitate was collected by filtration and dried under vacuum to give the pure product as a red solid (0.31 g, 89%). ¹H NMR (300 MHz, CD₂Cl₂): δ (ppm) 7.66-7.73 (12H, m), 7.48 (4H, t, J = 7.2 Hz), 7.38 (2H, t, 7.2 Hz), 7.29 (2H, s), 7.22 (2H, d, J = 3.6 Hz), 7.14 (2H, d, J = 3.6 Hz), 2.85 (4H, t, J = 7.8 Hz), 1.72 (4H, m), 1.28-1.46 (36H, b), 0.89 (6H, t, 6.0 Hz). Elemental analysis calculated for C₆₄H₇₄S₄: C, 79.12, H, 7.68%. Found: C, 77.69, H, 7.66%.

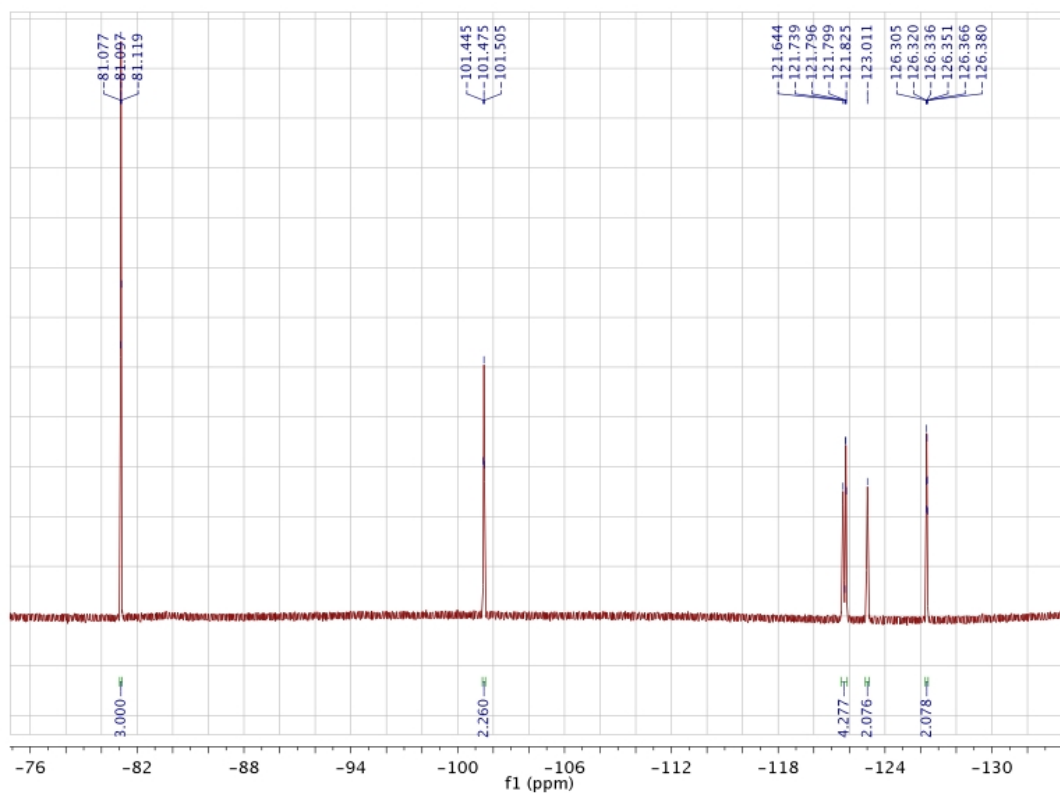
Appendix



¹H NMR Spectrum of DD8T in CD₂Cl₂



¹H NMR Spectrum of DFH-DD8T in CD₂Cl₂



¹⁹F NMR Spectrum of DFH-DD8T in CD₂Cl₂

References

- 1) Facchetti, A. *Mater. Today*. **2007**, 10, 28
- 2) Kulkarni, A. P.; Tonzola, C. J.; Babel, A.; Jenekhe, S. A. *Chem. Mater.* **2004**, 16, 4556
- 3) Günes, S.; Neugebauer, H.; Sariciftci, N. S. *Chem. Rev.* **2007**, 107, 1324
- 4) Manceau, M.; Rivaton, A.; Gardette, J.-L.; Guillerez, S.; Lemaître, N. *Polym. Degrad. Stabil.* **2009**, 94, 898
- 5) McCulloch, I.; Heeney, M.; Bailey, C.; Genevicius, K.; MacDonald, I.; Shkunov, M.; Sparrowe, D.; Tierney, S.; Wagner, R.; Zhang, W.; Chabinyc, M. L.; Kline, R. J.; McGehee, M. D.; Toney, M. F. *Nat. Mater.* **2006**, 5, 328
- 6) de Leeuw, D. M.; Simenon, M. M. J.; Brown, A. R.; Einerhand, R. E. F. *Synth. Met.* **1997**, 87, 53
- 7) Ong, B. S.; Wu, Y.; Liu, P.; Gardner, S. *J. Am. Chem. Soc.* **2004**, 126, 3378
- 8) Murphy, A. R.; Fréchet, J. M. J. *Chem. Rev.* **2007**, 107, 1066
- 9) Dimitrakopoulos, C. D.; Furman, B. K.; Graham, T.; Hegde, S.; Purushothaman, S. *Synth. Met.* **1998**, 92, 47
- 10) Hajlaoui, M. E.; Garnier, F.; Hassine, L.; Kouki, F.; Bouchriha, H. *Synth. Met.* **2002**, 129, 215
- 11) Facchetti, A.; Yoon, M. H.; Stern, C. L.; Hutchison, G. R.; Ratner, M. A.; Marks, T. J. *J. Am. Chem. Soc.* **2004**, 126, 13480
- 12) de Leeuw, D. M.; Simenon, M. M. J.; Brown, A. R.; Einerhand, R. E. F. *Synth. Met.* **1997**, 87, 53
- 13) Azumi, R.; Götz, G.; Debaerdemaeker, T.; Bäurle, P. *Chem. Eur. J.* **2000**, 6, 735
- 14) Fichou, D. *J. Mater. Chem.* **2000**, 10, 571
- 15) Ahmed, E.; Subramanian, S.; Kim, F. S.; Xin, H.; Jenekhe, S. A. *Macromolecules* **2011**, 44, 7207
- 16) Matharu, A. S.; Cowling, S. J.; Wright, G. *Liq. Cryst.* **2007**, 34, 489
- 17) Prehm, M.; Götz, G.; Bäuerle, P.; Liu, F.; Zeng, X.; Ungar, G.; Tschierske, C. *Angew. Chem. Int. Ed.* **2007**, 46, 7856
- 18) Yue, W.; Zhao, Y.; Tian, H.; Song, D.; Xie, Z.; Yan, D.; Geng, Y.; Wang, F. *Macromolecules* **2009**, 42, 6510

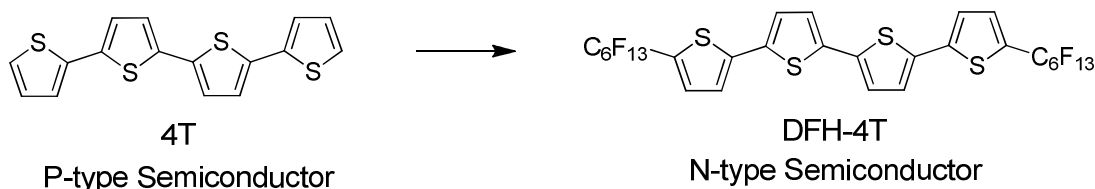
19) Furuya, T.; Strom, A. E.; Ritter, T. *J. Am. Chem. Soc.* **2009**, *131*, 1662

CHAPTER 4

Tuning Frontier Molecular Orbital Energies via α,ω -Perfluoroalkylation: P-type vs. N-type Conductivity in Perfluoroalkylated Oligothiophenes

4.1 Introduction

Small molecule semiconductors have received significant attention for organic field effect transistor (OFET) applications owing to their ease of purification and highly ordered thin films.¹ Furthermore molecular semiconductors are useful materials for understanding relationships between conductivity and material/film properties. Oligothiophene semiconductors have been a focus of research for OFETs for more than two decades and have played an important role in understanding structure property relationships over the years.^{1,2} Substitution of oligothiophenes has been a key strategy for controlling material properties such as solubility, molecular orbital energies, crystal structure, and film forming capability. Important lessons have been learned from these studies, directing the synthesis of new materials with desirable properties. One area of interest within OFET research is the design and discovery of n-type and ambipolar organic semiconductors, materials that are sought after for their importance in complementary circuit technologies.³⁻⁵ Substitution at the α,ω positions with perfluoroalkyl groups was previously shown to reverse the majority charge carrier of oligothiophene semiconductors, leading to n-type materials with good electron mobility (Scheme 4.1).⁶⁻⁹



Scheme 4.1 α,ω -Perfluoroalkylation of quaterthiophene leads to n-type conductivity

This is a result of the strong σ -electron withdrawing nature of the perfluoroalkyl substituent which leads to a lower lying LUMO, enabling electron injection from gold electrodes. In addition, perfluoroalkyl groups imparted interesting material properties to the oligothiophene semiconductors including improved volatility and enhanced fluorescence.⁶ However, these compounds had LUMO levels around -3.3 eV and were not ideal for n-channel OFETs which show stable operation in air when LUMO levels are \approx -4.0 to -4.3 eV.¹⁰ Interestingly, the perfluoroalkylated oligomers showed n-type conductivity only, even though HOMO levels were closer to the work function of gold than LUMO levels.

Apart from diperfluoroalkylated α -oligothiophenes, few thiophene based semiconductors incorporating perfluoroalkyl substituents have been studied.¹¹⁻¹³ One approach to further lower LUMO levels incorporated carbonyl groups between the thiophene backbone and the perfluorohexyl chain (Figure 4.1).

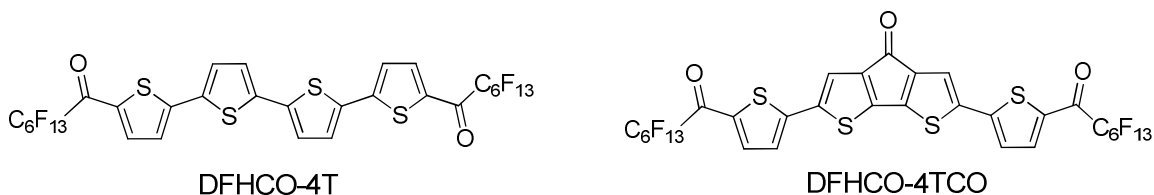


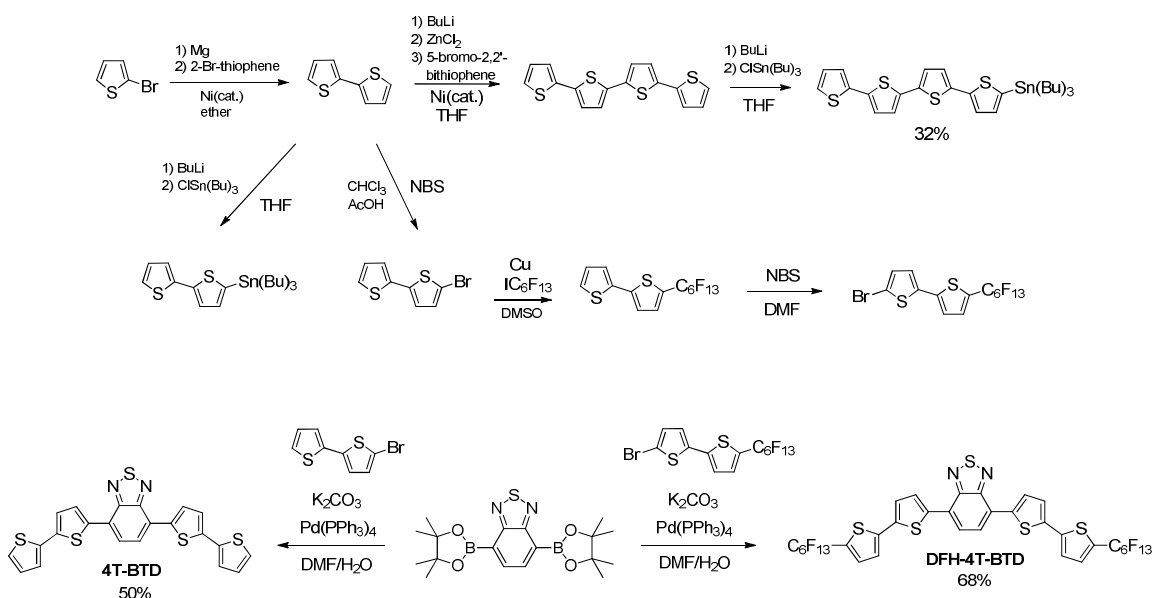
Figure 4.1 Perfluoroalkylated oligothiophenes incorporating carbonyl functionality

This led to a significant reduction in the LUMO level of the oligomers (-0.6 eV, DFH-4T → DFHCO-4T) and afforded n-type materials with high electron mobility. This work demonstrated the ability to produce materials with low lying LUMO levels by combining σ -electron withdrawing perfluoroalkyl groups with π -electron deficient groups.

This chapter presents the synthesis of an α,ω -diperfluoroalkylated oligothiophene with an electron deficient benzothiadiazole core for increased stabilization of the LUMO. The molecular orbital energies and field effect transistor properties of the new oligomer are compared to the α,ω -unsubstituted analog. Interesting differences in majority charge carrier for these two oligomers were observed as a result of the α,ω -substitution. This is discussed in terms of molecular orbital energetics and orbital geometries. In addition the synthesis and OFET properties of a monoperfluoroalkylated sexithiophene are presented. Though previous reports have presented the synthesis of monoperfluoroalkylated oligothiophenes,^{14,15} the semiconducting properties of these materials have not yet been studied in transistors. Together these studies shed light on the relationship between α,ω -substitution and majority charge carrier in oligothiophene semiconductors.

4.2 Synthesis

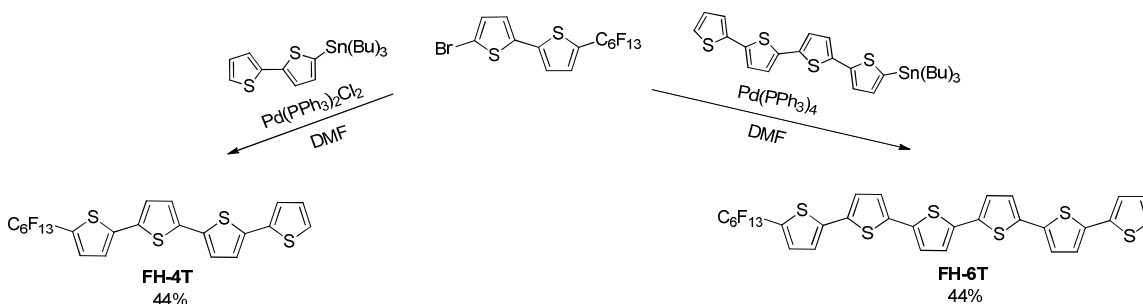
The synthesis of the new compounds first required preparing 5-bromo-5'-perfluorohexyl-2,2'-bithiophene. This was achieved following procedures in the literature as shown in Scheme 4.2. Oligomers 4T-BTD and DFH-4T-BTD were then obtained by Suzuki coupling of 2,1,3-benzothiadiazole-4,7-bis(boronic acid pinacol ester) with the appropriate flanking bithiophene. This route ensured solubility of the intermediates, and led to precipitation of the oligomers in relatively pure form. Compound 4T-BTD was previously prepared through Stille coupling but was obtained in less than 15% yield.¹⁶



The procedure used here afforded 4T-BTD in 50% yield and DFH-4T-BTD in 68% yield.

Both compounds were soluble enough for purification via recrystallization.

Monoperfluoroalkylated FH-4T and FH-6T were synthesized via Stille coupling between 5-bromo-5'-perfluorohexyl-2,2'-bithiophene and the corresponding stannylated oligothiophenes (Scheme 4.3). Compound FH-4T could be purified either by



recrystallization or by sublimation to give a bright yellow solid. Oligomer FH-6T was insoluble and was therefore purified via sublimation to give the pure compound as a bright orange solid. All oligomers were characterized by ^1H NMR and elemental analysis. Most of the oligomers had low solubility and therefore required high temperature NMR analysis using the high boiling $\text{C}_2\text{D}_2\text{Cl}_4$ solvent. Fluorinated oligomers were also characterized by ^{19}F NMR. Figure 4.2 shows the target compounds that will be

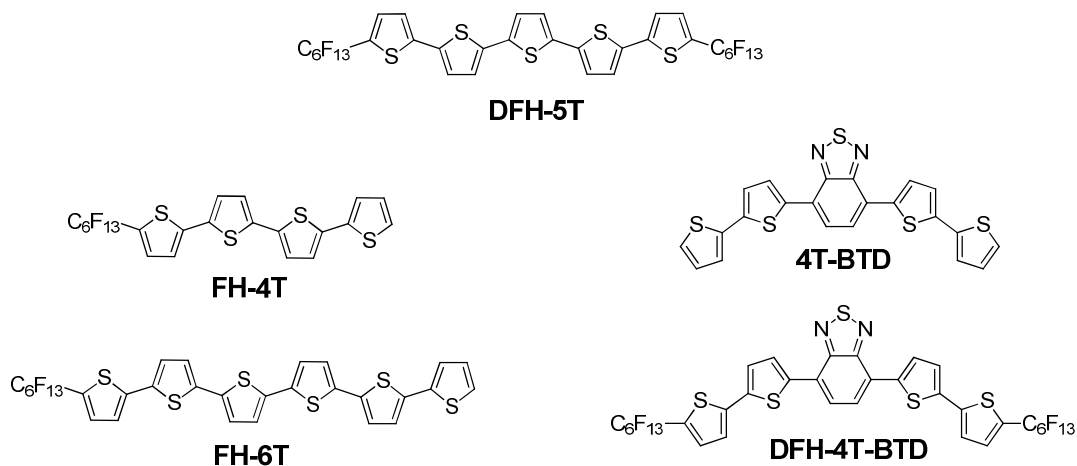


Figure 4.2 Target oligomers studied in this chapter

discussed in detail in this chapter. Compound DFH-5T was synthesized according to literature and used as a reference compound.

4.3 Thermal Properties

Thermal properties for the series of oligomers were evaluated using DSC in order to understand the relationship between molecular structure and strength of intermolecular forces. Compared to DFH-5T which melts at 249 $^{\circ}\text{C}$, compound DFH-4T-BTD melts at 237 $^{\circ}\text{C}$ (Figure 4.3), thus the benzothiadiazole core leads to a decrease in the cohesive forces of the π -system. However, comparing DFH-4T-BTD to 4T-BTD (m.p

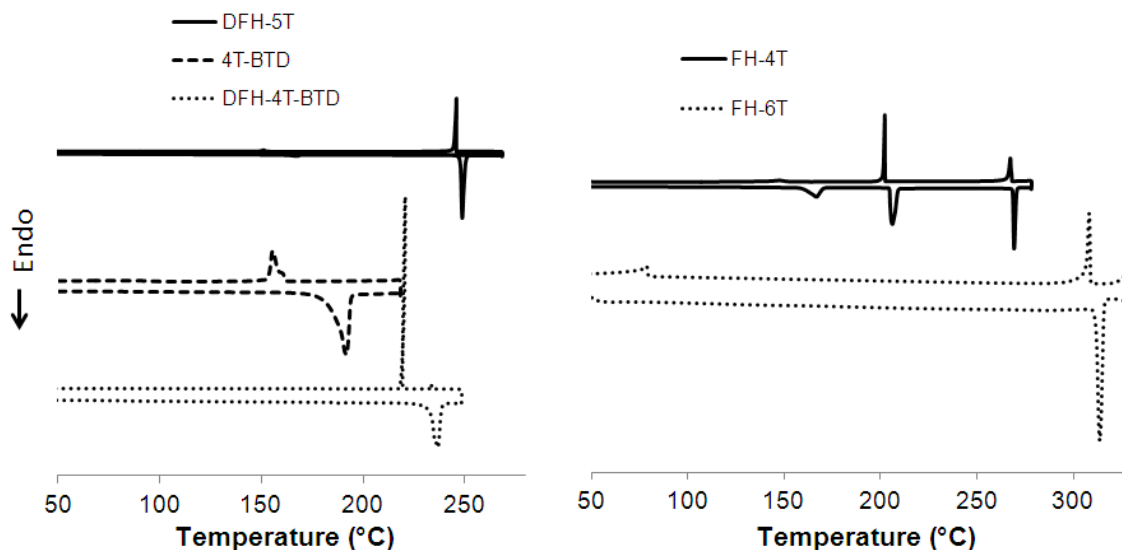


Figure 4.3 First heating DSC thermograms of diperfluoroalkylated (left) and monoperfluoroalkylated (right) oligomers

= 192 °C) the perfluoroalkyl substituents greatly increase the strength of intermolecular forces.

Compound 4T-FH was found to melt at 208 °C and compound 6T-FH melted at 314 °C. These values are close to the melting points of the unsubstituted analogs,⁷ thus asymmetric perfluoroalkylation of these oligomers does not significantly disrupt their crystalline packing. Interestingly, compound 6T-FH melts at a higher temperature than the symmetric diperfluorohexyl analog DFH-6T. Compound 4T-FH exhibited two additional exotherms upon heating, one prior to melting and one after melting. The low temperature transition was observed on multiple heating cycles, and has been observed for other perfluoroalkylated materials including DFH-5T. This peak is therefore attributed to a structural transition of the perfluorohexyl group. The latter peak is attributed to a liquid crystalline to isotropic transition, and is reversible upon cooling.

Polarized optical microscopy was used to investigate mesophases for all oligomers. All of the compounds showed liquid crystalline textures except for DFH-5T. Thus, the appearance of a mesophase in this series depends on the π system and not

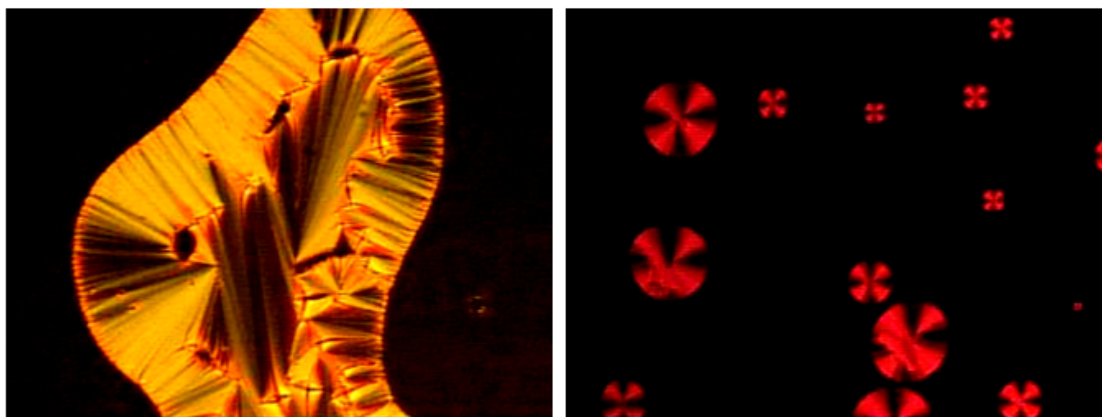


Figure 4.4 Polarized optical images of FH-4T at 230 °C (left) and DFH-4T-BTD at 225 °C (right)

on perfluoroalkyl substitution. The liquid crystal textures for compounds DFH-4T-BTD and FH-4T suggest smectic phases for these compounds (Figure 4.4). Compound 4T-FH displayed a particularly stable and reproducible LC phase. Compound 6T-FH also exhibited liquid crystalline behavior, though the mesophase was at too high of temperatures to fully investigate.

4.4 Optical Properties

The solution UV/vis spectra obtained in THF are shown in Figure 4.5. For compounds that only contain thiophene rings the absorption maximum increases with oligomer length as a result of the extended conjugation which leads to a smaller band gap. Perfluoroalkylation appears to reduce the band gap of the oligothiophenes as evidenced by the similarity in absorption maxima for DFH-5T and FH-6T. The oligomers containing benzothiadiazole show two maxima, the lower energy transition a result of intramolecular charge transfer, a characteristic of donor-acceptor π -conjugated materials.^{17,18} Thus the outer thiophene rings of DFH-4T-BTD retain substantial donor character relative to the benzothiadiazole core, even with the electron withdrawing α,ω -perfluorohexyl substituents.

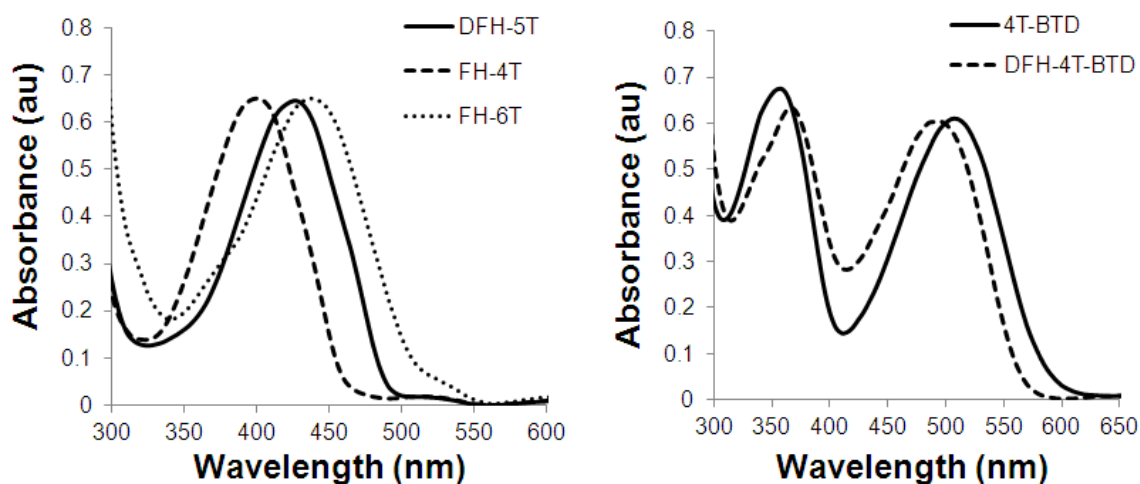


Figure 4.5 UV/vis spectra of oligomers in THF

Fluorescence spectra of the oligomers in THF are shown in Figure 4.6. The spectra of monoperfluoroalkylated FH-4T and FH-6T are more broad compared to diperfluoroalkylated DFH-5T. The fluorescence of benzothiadiazole containing compounds is shifted to longer wavelengths due to the low band-gap of the donor-acceptor oligomers. Fluorescence quantum yields were determined for most oligomers using rhodamine B as a standard. Previous studies found that α,ω perfluoroalkylation greatly increased fluorescence quantum yields of oligothiophenes.⁸ This trend was not observed for DFH-4T-BTD which had a ϕ_f of 0.46 (Table 4.1), almost identical to that of the unsubstituted analog 4T-BTD ($\phi_f = 0.44$). Both benzothiadiazole oligomers exhibited relatively large Stokes shifts ($\approx 3,800 \text{ cm}^{-1}$), and the lower quantum yields for these compounds may be due to longer excited state lifetimes leading to increased non-radiative decay.¹⁹ Monosubstituted FH-6T had a ϕ_f of 0.59, very close to the previously reported quantum yield of α -sexithiophene.⁸ Therefore, the effects of perfluoroalkylation on the fluorescence of oligothiophenes are not universal, and depend on both the π -system as well as the degree of perfluoroalkylation. It seems that the large increase in quantum yield upon perfluoroalkylation of α -nTs is unique to that series of oligomers,

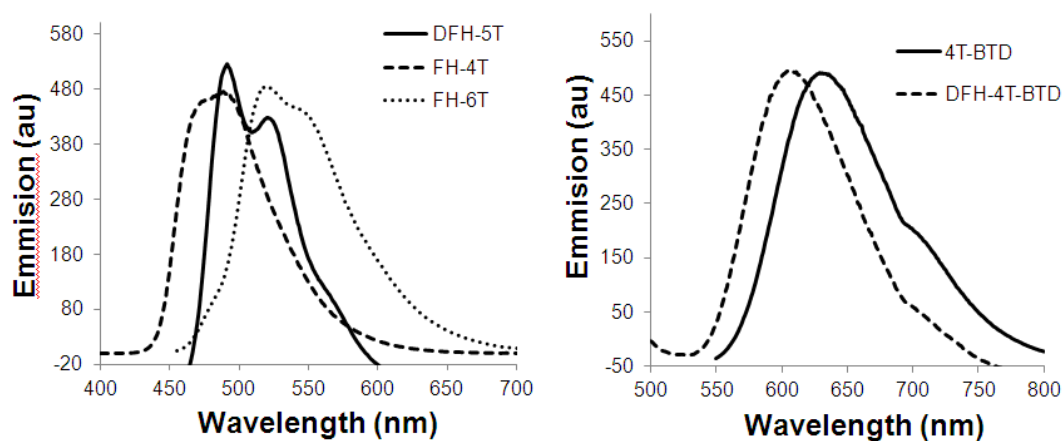


Figure 4.6 Normalized fluorescence spectra in THF

and that perfluoroalkylation in general is not an established method for improving fluorescence efficiency of π -conjugated materials.

Table 4.1 Optical properties

Compound	$\lambda_{\text{abs, THF}}$ (nm)	$\lambda_{\text{em, THF}}$ (nm)	E_g (eV) ^a	Stokes shift (cm ⁻¹)	ϕ_f
DFH-5T	426	491, 522	2.62	3163	0.76
FH-4T	401	488	2.77	4508	-
FH-6T	438	520	2.53	3758	0.59
4T-BTD	358, 508	629	2.15	3904	0.44
DFH-4T-BTD	367, 495	606	2.23	3700	0.46

4.5 Electrochemical properties

While most organic semiconductors are theoretically ambipolar in nature, majority charge carriers (holes or electrons) are typically a result of restricted charge

injection from source/drain electrodes into either the HOMO or LUMO of the semiconductor. Accessible charge injection results when the work function of the source/drain material is closely matched with one or more of the frontier molecular orbital energies. Therefore, electrochemical determination of the orbital energies is helpful for understanding observed majority charge carriers.

Under the experimental conditions diperfluoroalkylated DFH-5T shows a HOMO level of -5.83 eV and a LUMO of -2.80 eV (Figure 4.7). In moving from DFH-5T to FH-6T two structural changes are noted; 1) an extra thiophene ring is added and 2) one perfluoroalkyl substituent is removed. The addition of a thiophene ring is expected to increase the HOMO level and reduce the band-gap of the oligomer. On the other hand, removing an electron withdrawing perfluoroalkyl substituent from one side of the molecule should result in a slightly higher LUMO level than the corresponding diperfluoroalkylated oligomer. The overall result is that FH-6T shows a rise in the HOMO level (-5.58 eV) while the LUMO level is unchanged (-2.80 eV) compared to DFH-5T. Thus monoperfluoroalkylated FH-6T has identical electron affinity as the known n-type DFH-5T, with a lower ionization potential and therefore a greater propensity for hole injection. Surprisingly the HOMO level of FH-4T was very close to that of FH-6T at -5.63 eV. The LUMO of FH-4T at -2.58 eV was however much higher in energy than that of FH-6T.

As expected, replacing the central thiophene ring of DFH-5T with a benzothiadiazole unit significantly lowers the LUMO to -3.10 eV for DFH-4T-BTD. The HOMO level of DFH-4T-BTD is also significantly lower than the other oligomers at -5.97 eV, consistent with the DFT calculations. However, 4T-BTD showed the lowest reduction potential, with calculated LUMO at -3.19 eV. This was unexpected from knowledge of the structures and calculated LUMO energies. The discrepancy is most likely a result of desorption of the film during experiments which can affect the observed redox potentials. It should be

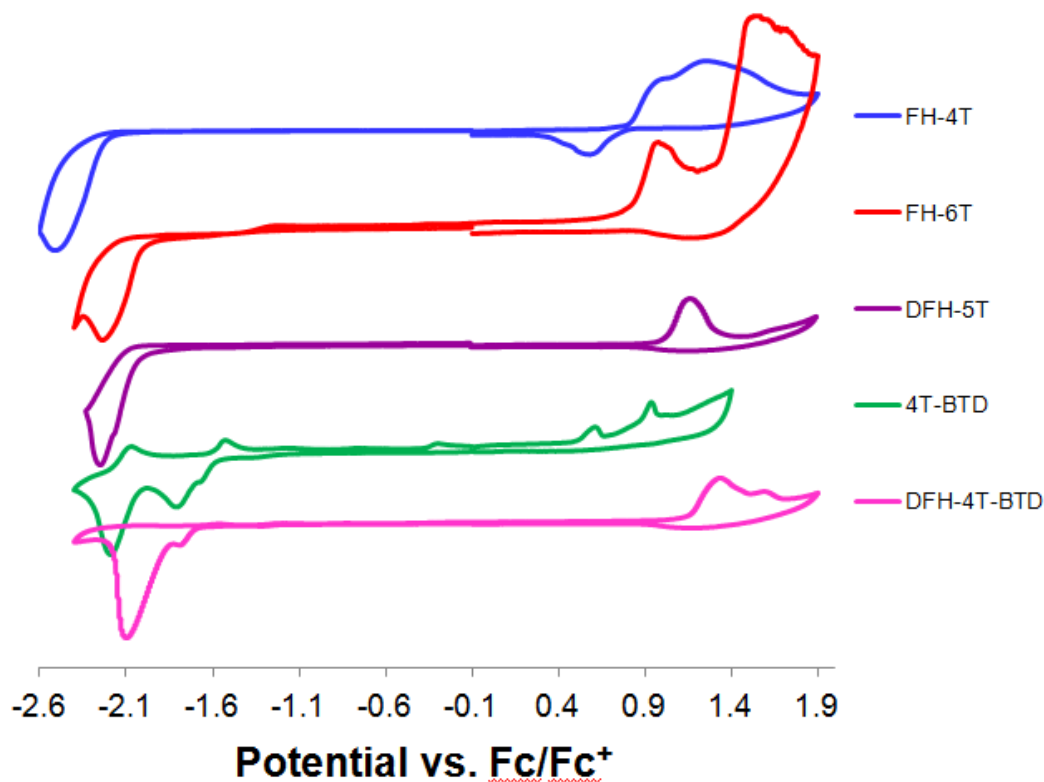


Figure 4.7 Cyclic voltammograms of thin films of the oligomers

noted that for all oligomers the workfunction of gold (5.0-5.1 eV) is closer to HOMO energy than LUMO energy, and thus from simple energetic considerations hole injection has a lower barrier than electron injection for all compounds. However, DFH-5T is known to be n-type only when employing gold source/drain electrodes. This illustrates the complexity of charge injection, which also depends on morphological considerations, molecular dipole orientation, and the nature of the metal/organic interface.

4.6 Density Functional Theory Calculations

Density functional theory (DFT) simulations were employed to further understand the relationship between molecular structure and frontier molecular orbital energies. The

simulations also provide information regarding electron distribution in the frontier orbitals. The results of the calculations are summarized in Table 4.2.

First, the effects of transitioning from unsubstituted to monoperfluoroalkylated to diperfluoroalkylated were studied for quinquethiophene (Figure 4.8). Both HOMO and LUMO energies follow the expected trend of $\alpha 5T > FH-5T > DFH-5T$. While the HOMO orbitals are similar in appearance, perfluoroalkyl substitution leads to a decrease in electron density at the substituted thiophene ring. The reduction in HOMO energy is significant, and the change in energy going from $\alpha 5T \rightarrow FH-5T$ (-0.24 eV) is essentially the same as the change going from $FH-5T \rightarrow DFH-5T$ (-0.26 eV). In the LUMO orbitals perfluoroalkyl substituents draw electron density to the peripheral thiophene rings. This effect is pronounced in $FH-5T$ which shows a highly asymmetric orbital. The LUMO energy is affected more upon addition of the first perfluoroalkyl substituent ($\alpha 5T \rightarrow FH-5T$, -0.31 eV) than the second ($FH-5T \rightarrow DFH-5T$, -0.23 eV).

In contrast to perfluoroalkylation which significantly lowers both the HOMO and LUMO energies, incorporation of the electron deficient BTB ring primarily affects the LUMO energy. The HOMO orbital of 4T-BTB is very similar in appearance to that of $\alpha 5T$ and is only ≈ 0.1 eV lower in energy. On the other hand the LUMO is concentrated on the BTB ring, which significantly stabilizes the orbital (Figure 4.9). The reduction in LUMO energy upon incorporation of the BTB unit (0.70 eV) is greater than the reduction that results from α,ω perfluoroalkylation (0.54 eV). The LUMO of perfluoroalkylated $DFH-4T-BTB$ is similar in appearance to that of 4T-BTB but is 0.41 eV lower in energy, affording by far the lowest calculated LUMO of the series at -3.42 eV (Table 4.2). Perfluoroalkylation again leads to a large reduction in the HOMO energy for $DFH-4T-BTB$ (0.51 eV).

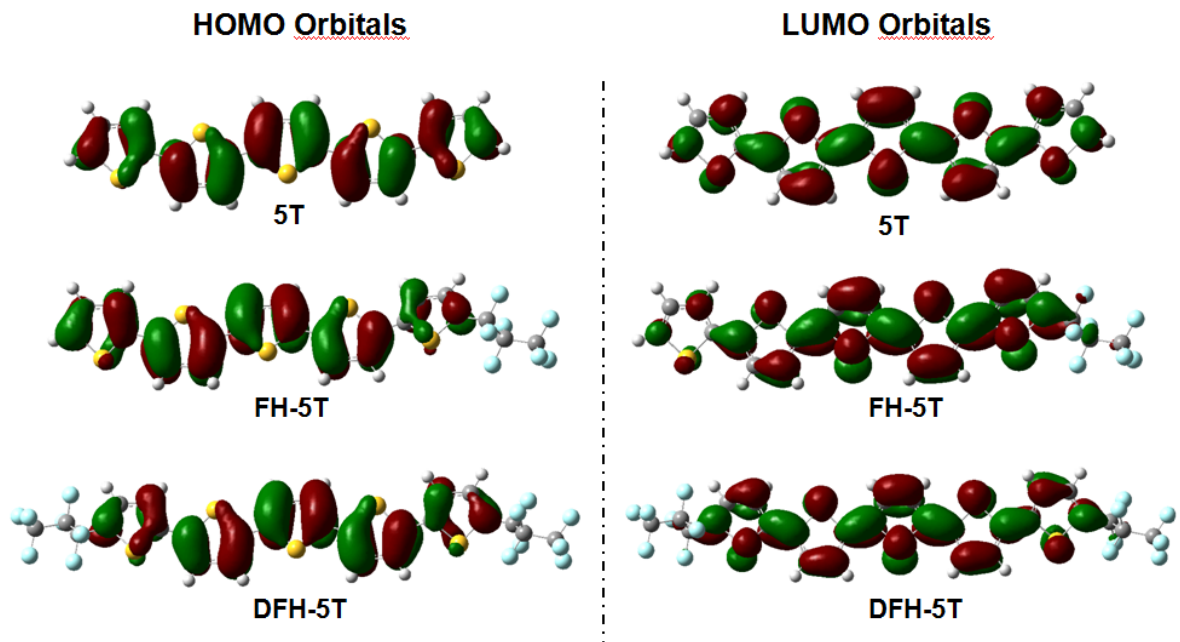


Figure 4.8 Calculated HOMO and LUMO orbitals for α 5T, FH-5T, and DFH-5T

Table 4.2 Calculated HOMO and LUMO energies

Compound	HOMO (eV)	LUMO (eV)	E_g (eV)
α 5T	-5.23	-2.31	2.92
FH-4T	-5.64	-2.54	3.10
FH-5T	-5.47	-2.62	2.85
FH-6T	-5.35	-2.67	2.68
DFH-5T	-5.73	-2.85	2.86
DFH-4T-BTD	-5.83	-3.42	2.41
4T-BTD	-5.32	-3.01	2.31

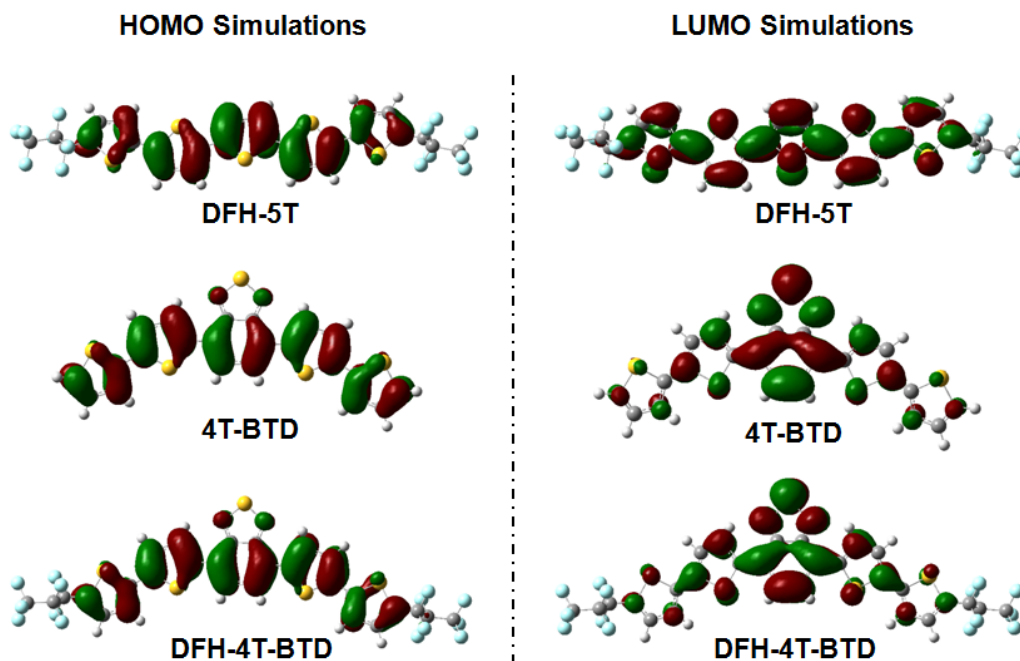


Figure 4.9 Calculated HOMO/LUMO orbitals for DFH-5T, 4T-BTD, and DFH-4T-BTD

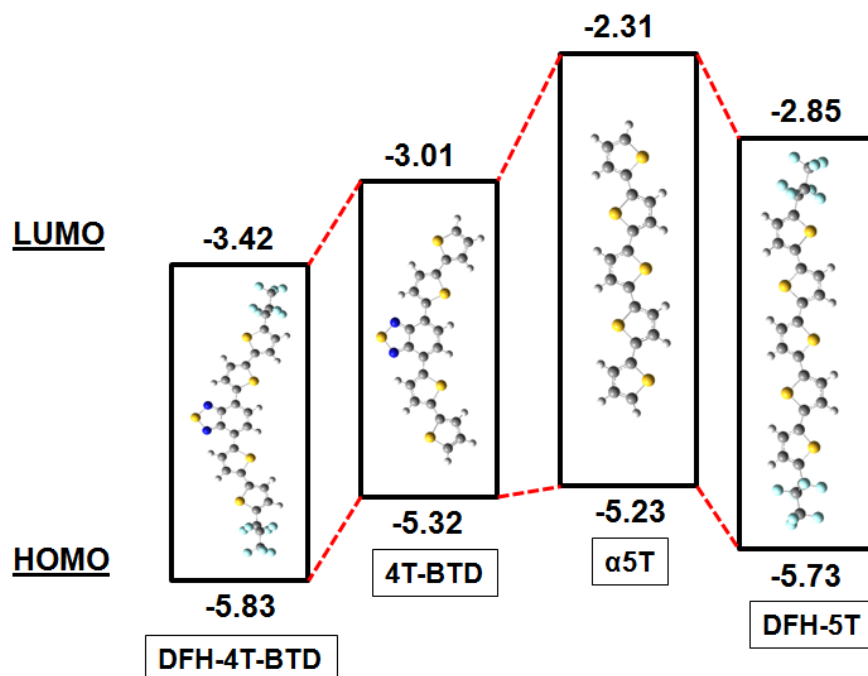


Figure 4.10 Energy diagram illustrating the changes in HOMO/ LUMO energies of the oligomers upon chemical substitution

4.7 Field Effect Transistor Characterization

Thin film transistors are useful devices for evaluating the majority charge carriers and charge mobilities of organic semiconductors. All organic semiconductors are theoretically ambipolar, and the observed majority charge carrier is mainly dependent upon charge injection barriers from the source/drain electrode material. Top-contact bottom-gate transistors were fabricated in order to explore the majority charge carriers and charge mobilities of the new semiconductors. Si(doped)/SiO_x wafers were first treated with a hydrophobic self-assembled monolayer to mask charge traps and promote improved morphologies at the dielectric. The semiconductors were then evaporated onto the substrates under high vacuum. Gold source and drain electrodes were then evaporated through a shadow mask in order to define the transistor channel. This device structure was chosen because top-contact devices typically result in much smaller contact resistance compared to bottom-contact when using evaporated thin films. The transistor results are summarized in table 4.3.

From the molecular orbital energies derived from DFT calculations compounds 4T-BTD and DFH-4T-BTD are expected to be good n-type semiconductors based off their low lying LUMO levels. Oligomer 4T-BTD was first examined and interestingly only showed p-type transistor activity (Figure 4.11). The output characteristics of 4T-BTD

Table 4.3 Summary of FET device characteristics

Compound	FET Type	μ (cm ² /Vs)	V _T (V)	I _{on/off}
DFH-5T ^a	<i>n</i>	2.6 x 10 ^{-2b}	35-40	6 x 10 ⁴
DFH-4T-BTD	<i>n</i>	3.6 x 10 ^{-3b}	15-20	10 ³ -10 ⁴
4T-BTD	<i>p</i>	2.3 x 10 ⁻³	-10	2 x 10 ⁴
FH-6T	<i>p</i>	1.1 x 10 ⁻³	-25	10 ⁵

^aData taken from reference 9. ^bSubstrate was heated to 70 °C during organic deposition

show no sign of contact resistance. Hole mobilities calculated for 4T-BTD were typically $2.0 \times 10^{-3} \text{ cm}^2/\text{Vs}$ with a relatively low threshold voltage around -10 V and on/off current ratios $> 10^4$. The exclusively p-type character of 4T-BTD is surprising considering the LUMO level is even lower than DFH-5T which is known to be n-type only. However, the HOMO level of 4T-BTD (-5.32 eV) is much higher than DFH-5T (-5.73 eV) and is thus well-matched with the work function of gold.

In contrast to 4T-BTD, compound DFH-4T-BTD showed only n-type transistor activity. Besides the difference in majority charge carrier, 4T-BTD and DFH-4T-BTD showed very similar device properties. Electron mobilities calculated for DFH-4T-BTD

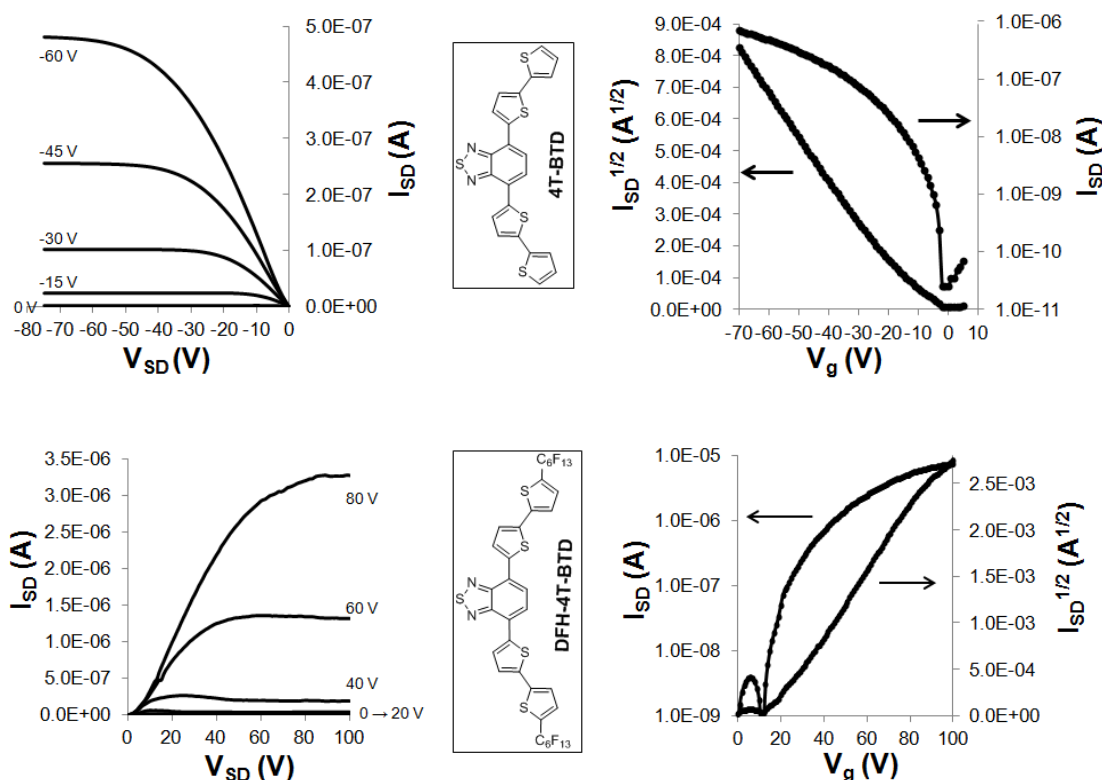


Figure 4.11 Output (left) and transfer characteristics (right) of 4T-BTD (top) and DFH-4T-BTD (bottom) transistors

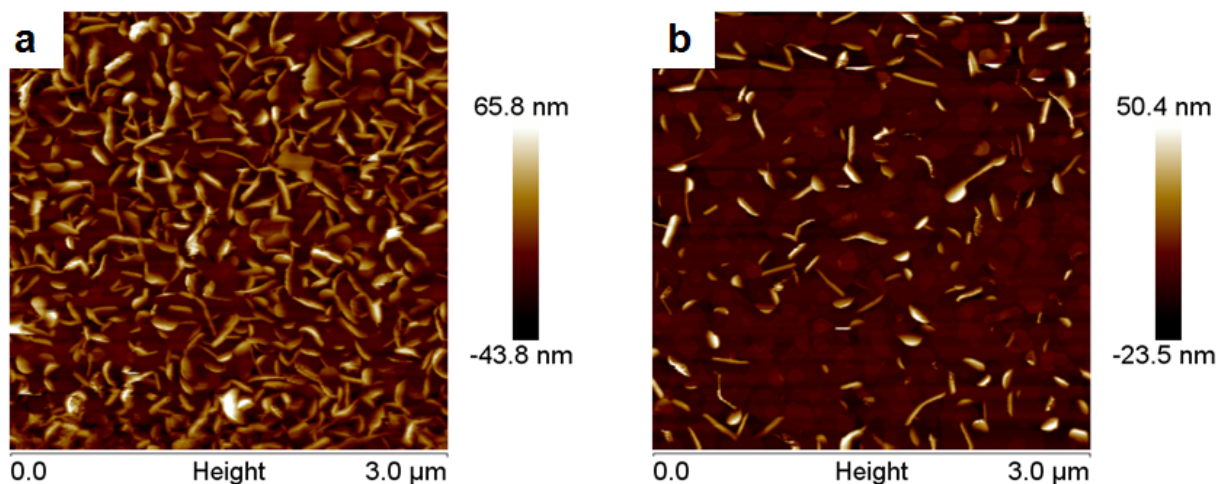


Figure 4.12 AFM images of DFH-4T-BTD films grown at room temperature (left) and at 70 °C (right)

reached $4.7 \times 10^{-3} \text{ cm}^2/\text{Vs}$ (average mobility $3.6 \times 10^{-3} \text{ cm}^2/\text{Vs}$) when the substrate was heated to 70 °C during evaporation. Mobilities were slightly lower when the substrate was not heated during evaporation (average mobility $9.8 \times 10^{-4} \text{ cm}^2/\text{Vs}$). The morphology of DFH-4T-BTD films was investigated by imaging a transistor channel using AFM (Figure 4.12). The images reveal a well-defined morphology comprised of flaky crystallites on the order of 300-500 nm in length, similar to what was previously observed for DFH-5T films.^{6,7} The film that was deposited onto a substrate held at 70 °C showed a more continuous film with less grain boundaries. The improvement in charge mobility for the devices with films grown at 70 °C can therefore be attributed to reduced resistance as a result of improved grain connectivity. The threshold voltage of DFH-4T-BTD devices was relatively low at 15-20 V, an improvement from the higher threshold voltages previously reported for DFH-5T (35-40 V).⁹ This is a result of the lower electron injection barrier into the low lying LUMO of DFH-4T-BTD.

The difference in majority charge carrier for 4T-BTD vs. DFH-4T-BTD is interesting considering the molecular orbital geometries/energies of the two oligomers. On one hand, 4T-BTD has a relatively high HOMO level which imparts a propensity for

hole injection, leading to p-channel devices. However, the LUMO level of 4T-BTD is lower than that of DFH-5T and could therefore be expected to efficiently accept electrons from gold. Furthermore, the LUMO geometry of 4T-BTD is almost identical to that of DFH-4T-BTD which was shown to only conduct electrons. The lack of n-channel activity in 4T-BTD is therefore somewhat surprising. The difference in majority charge carrier is thus likely related to the electronic interactions at the semiconductor/Au interface. At this interface the gold-molecule interactions may lead to an electronic state that differs from the bulk, and only allows injection of one type of carrier.

The monoperfluoroalkylated oligomers showed molecular orbital energies in between those of the corresponding unsubstituted and diperfluoroalkylated oligomers. Therefore, understanding the majority charge carrier in these materials was of interest. When FH-4T was tested in devices no FET behavior could be observed, regardless of the film growth temperature. The morphology of an FH-4T film grown at 50 °C was studied using AFM (Figure 4.13). The film showed a morphology consisting of well connected grains, with a much lower surface roughness compared to DFH-4T-BTD films. The morphology of FH-4T appears to be more ideal for charge transport, since film growth appears to take place primarily within the plane of the substrate. This is expected to lead to better monolayer coverage at the dielectric as well as improved grain connectivity as compared to DFH-4T-BTD. The lack of transistor response in FH-4T is therefore most likely a result of large charge injection barriers for both holes and electrons. Whereas unsubstituted and alkyl substituted quaterthiophenes show p-type conductivity,⁹ the perfluoroalkyl substituent lowers the HOMO level of FH-4T preventing hole injection. On the other hand, the single perfluoroalkyl substituent of FH-4T does not lower the LUMO enough to observe electron injection.

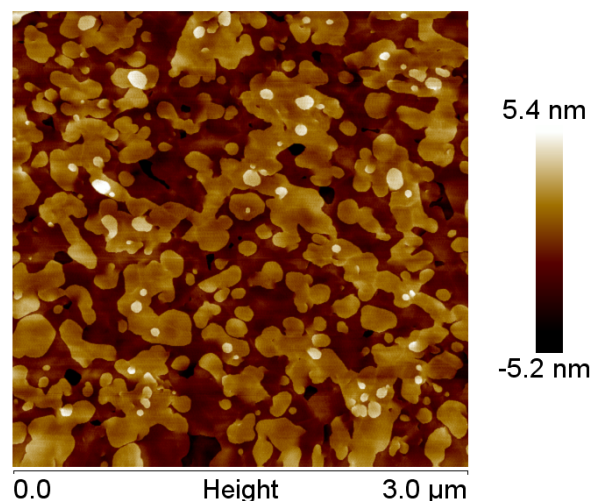


Figure 4.13 AFM image of FH-4T film grown at 50 °C

Devices employing FH-6T showed p-type conductivity only (Figure 4.14). Average hole mobility calculated for FH-6T were was $1.1 \times 10^{-3} \text{ cm}^2/\text{Vs}$, with threshold voltages of 20-25 V and On/off current ratios of 10^4 - 10^5 . Heating the substrate to 70 °C during evaporation did not improve device parameters for FH-6T. The threshold voltage for FH-6T was higher than that of 4T-BTD, a result of the lower lying HOMO energy of FH-6T (from electrochemical data). The absence of n-channel activity for FH-6T was somewhat surprising considering the very similar LUMO energies of FH-6T and DFH-5T.

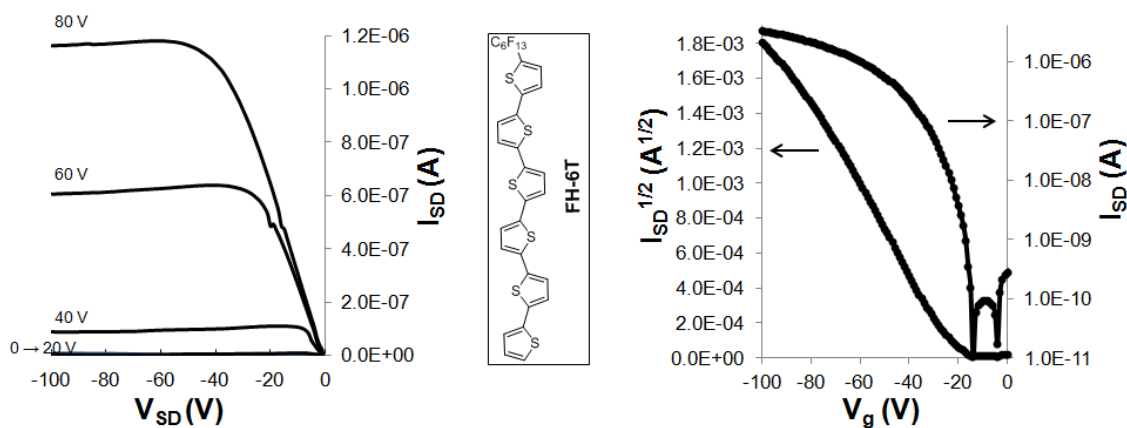


Figure 4.14 Output (left) and transfer (right) characteristics of FH-6T transistors

Again, this is likely due to the specific interactions at the Au/semiconductor interface which may modify charge injection barriers.

The findings from these FET studies shed light on the relationships between molecular orbital energy/geometry and majority charge carrier in OFETs. It is clear that α,ω -substitution of oligothiophenes has significant effects on orbital energies and charge injection barriers. Even for 4T-BTD with its low lying LUMO, α,ω -perfluoroalkylation is necessary in order to observe electron conductivity. In addition, for α -oligothiophenes monoperfluoroalkylation is not adequate for achieving electron injection. Within this series of compounds, perfluoroalkylation at both the α and ω positions was necessary in order to observe n-channel FET behavior. This finding is not universal for all materials,⁹ however; it shows that orbital energetics are not the only consideration for tuning majority charge carrier. Most likely the Au/semiconductor interface plays a large role in determining charge injection. This interface is no doubt dependent on the molecular structure and molecular dipole of the semiconductor.

4.8 Conclusion

A series of unique perfluoroalkylated oligothiophenes were synthesized and their semiconducting properties were characterized. Employing a π -electron deficient benzothiadiazole core in combination with electron withdrawing perfluoroalkyl substituents effectively lowered the LUMO to -3.42 eV (DFT) for DFH-4T-BTD. This compound showed n-channel transistors with electron mobilities comparable to that of DFH-5T but with lower threshold voltages due to the low lying LUMO. On the other hand unsubstituted 4T-BTD showed only p-type behavior as a result of its high HOMO level. Thus, while benzothiadiazole units are more effective than perfluoroalkyl substituents at lowering the LUMO energies of oligothiophenes, the latter is more effective for electron

injection from Au. This is because perfluoroalkyl substituents significantly lower the HOMO of the oligomers while the benzothiadiazole ring has little effect on the HOMO. Monoperfluoroalkylated sexithiophene showed HOMO/LUMO energies in between those of α 6T and DFH-6T, and showed only p-type transistors. These findings demonstrate the delicate balance between chemical substitution, molecular orbital energetics, and charge injection in oligothiophene semiconductors.

4.9 Experimental

Materials and methods. All materials were purchased from Sigma Aldrich and used as received unless otherwise noted. 5-bromo-2,2-bithiophene,²⁰ [2,2'-bithiophen]-5-yltributylstannane²¹ and 5,5''''-Diperfluorohexyl-2,2':5',2'':5'',2''':5''',2''''-quinquethiophene (DFH-5T)⁸ were synthesized following procedures in the literature. Cyclic voltammetry was performed using a Bioanalytical Systems (BAS) Epsilon potentiostat equipped with a standard three-electrode configuration. Scans were performed on oligomer films evaporated onto a glassy carbon electrode which served as the working electrode. A Pt wire was used as counter electrode and an Ag/AgNO₃ (0.01 M in anhydrous acetonitrile) was used as the reference electrode. Measurements were performed in anhydrous acetonitrile with tetrabutylammonium hexafluorophosphate (0.1 M) as supporting electrolyte under nitrogen at a scan rate of 100 mV/s. Internal calibration of the reference potential was achieved using the ferrocene/ferrocenium redox couple. Melting points and thermal transitions were analyzed using a TA instruments Q200 differential scanning calorimeter.

OTFT Device Fabrication. Top Contact OFETs were fabricated on heavily *n*-doped Si (Sb, $\rho = 0.005$ -0.025 Ohm cm), with a 200 nm thermal oxide as dielectric ($C_i = 17.2$ nF/cm²). Wafers were cleaned in piranha at 80 °C for 30 min, rinsed with H₂O and dried under N₂. For OTS monolayers wafers were submerged into a 0.1 M toluene solution of

octyltrichlorosilane at 70 °C for 30 min, then rinsed with acetone and dried under N₂. For F-OTS monolayers wafers were submerged in a 0.01 M toluene solution of trichloro(1H,1H,2H,2H-perfluorooctyl)silane for 1 min, then rinsed with acetone and dried under N₂. A 50 nm organic film was then deposited under vacuum at pressures below 10⁻⁵ torr. Some films were evaporated onto hot substrates by heating the copper mount. Source and drain electrodes (Au, 30 nm) were then patterned by evaporation through a shadow mask under vacuum. Transistor channel lengths were 4 mm with widths of 30-100 μm. Devices were measured under vacuum using a Keithley 4200-SCS.

Synthesis

[2,2':5',2'':5'',2'''-quaterthiophen]-5-yltributylstannane: To a dry 500 mL flask was added α-quaterthiophene (1.5 g, 4.5 mmol) and 300 mL of dry THF. After sonication the solution was cooled to 0 °C, and *n*-Butyllithium (2.8 mL, 4.5 mmol) was added dropwise via syringe. After stirring for 20 min at 0 °C the solution was warmed to rt and allowed to stir for 1 hr. Tributyltin chloride (1.5 g, 4.6 mmol) was then added to the solution via syringe, and the reaction was stirred overnight. The reaction was quenched with 15 mL of methanol followed by removal of all solvents under reduced pressure. The solid was then collected and washed with 100 mL of cold methanol, and then extracted with 100 mL of cold hexanes. Removal of the hexanes afforded the product (0.9 g, 32%) in approximately 92% purity, which was adequate for subsequent reactions. The remaining 8% was a mixture of unreacted tributyltin chloride and bis(tributyltin) substituted quaterthiophene. ¹H NMR (400 MHz, CDCl₃): δ (ppm) 7.29 (1H, m), 7.22 (1H, d, J = 5 Hz), 7.17 (1H, d, J = 3.3 Hz), 7.07-7.09 (5H, m), 7.03 (1H, dd, J = 5 Hz, 1 Hz), 1.55-1.63 (6H, m), 1.32-1.38 (6H, m), 1.13 (6H, t, J = 8.5 Hz), 0.91 (9H, t, J = 7.3 Hz).

4,7-di([2,2'-bithiophen]-5-yl)benzo[c][1,2,5]thiadiazole (4T-BTD): A mixture of 5-bromo-2,2'-bithiophene (0.80 g, 3.3 mmol), 2,1,3-benzothiadiazole-4,7-bis(boronic acid pinacol ester) (0.57 g, 1.5 mmol), Pd(PPh₃)₄ (0.080 g, 0.073 mmol), K₂CO_{3(aq)} (4.5 mL,

1.3 M) and 30 mL DMF was purged with argon for 0.5 h and then stirred at 85 °C overnight. The dark purple precipitate was then poured onto a Buchner funnel and repeatedly washed with water and methanol. The solid was recrystallized from chloroform/methanol to afford the pure product (0.34 g, 50%). M.p = 192 °C. ¹H NMR (500 MHz, CD₂Cl₂): δ (ppm) 8.12 (2H, d, J = 4.0 Hz), 7.96 (2H, s), 7.37 (2H, d, J = 2.5 Hz), 7.34-7.45 (4H, m), 7.13 (2H, dd, J = 4.5, 4.0 Hz).

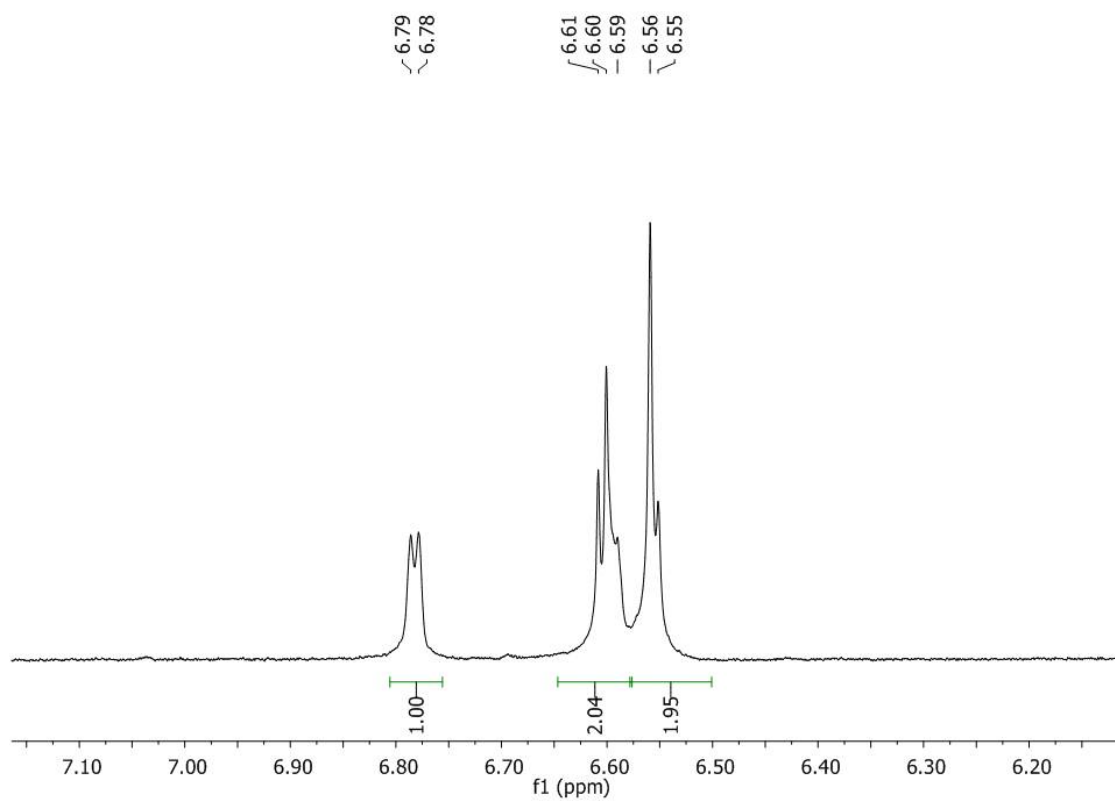
4,7-di(5'-perfluorohexyl-2,2'-bithiophen-5-yl)benzo[c][2,1,3]thiadiazole (DFH-4T-BTD): A mixture of 5-bromo-5'-perfluorohexyl-2,2'-bithiophene (0.80 g, 1.42 mmol), 2,1,3-benzothiadiazole-4,7-bis(boronic acid pinacol ester) (0.19 g, 0.49 mmol), Pd(PPh₃)₄ (0.028 g, 0.025 mmol), K₂CO_{3(aq)} (2.5 mL, 0.8 M) and 20 mL DMF was purged with argon for 0.5 h and then stirred at 80 °C overnight. The dark red precipitate was then poured onto a Buchner funnel and repeatedly washed with water, methanol and diethyl ether to afford the crude product (0.50 g, 92%). The solid was recrystallized from 1,2-dichlorobenzene to afford the pure product (0.37 g, 68%) as a dark red solid. ¹H NMR (500 MHz, C₂D₂Cl₄, 110 °C): δ (ppm) 7.49 (2H, d, J = 3.5 Hz), 7.31 (2H, s), 6.82 (2H, d, J = 4.0 Hz), 6.78 (2H, d, J = 4.0 Hz), 6.71 (2H, d, J = 3.5 Hz). ¹⁹F NMR (500 MHz, C₂D₂Cl₄, 110 °C): δ (ppm) -80.9 (6F, b), -100.4 (4F, b), -120.8 (4F, b), -121.0 (4F, b), -122.3 (4F, b), -125.5 (4F, b). Elemental analysis calculated for C₃₄H₁₀F₂₆N₂S₅: C, 37.10, H, 0.92, F, 44.88%. Found: C, 37.02, H, 0.88, F, 44.50%.

5-(perfluorohexyl)-2,2':5',2'':5'',2'''-quaterthiophene (FH-4T): A mixture of 5-bromo-5'-perfluorohexyl-2,2'-bithiophene (0.70 g, 1.2 mmol), [2,2'-bithiophen]-5-yltributylstannane (0.62 g, 1.4 mmol), Pd(PPh₃)₄ (0.04 g, 0.06 mmol) and 10 mL DMF was purged with argon for 0.5 h and then stirred at 80 °C overnight. The reaction mixture was cooled to rt and poured onto a Buchner funnel to collect the yellow precipitate. The crude product was washed with ethanol and then dried under vacuum before being purified by vacuum sublimation. The product was purified further by recrystallization from

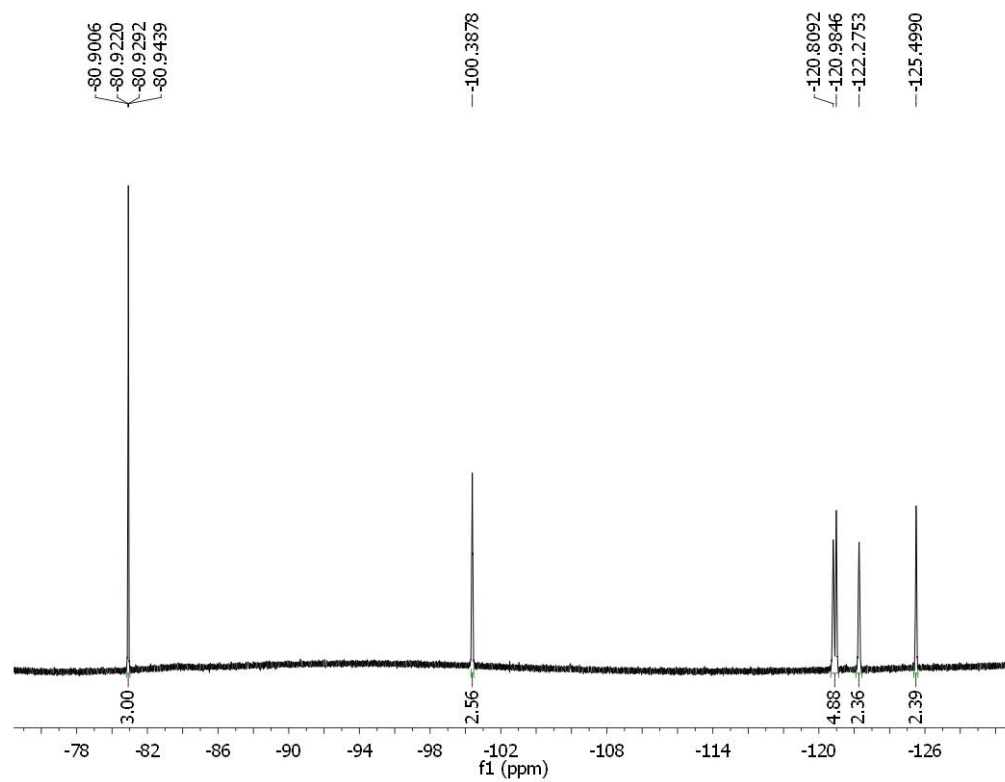
chloroform to afford the bright yellow solid (0.35 g, 44%). ^1H NMR (500 MHz, CD_2Cl_2): δ (ppm) 7.43 (1H, b), 7.32 (1H, m, b), 7.25-7.27 (3 H, m), 7.17-7.20 (3 H, m), 7.08-7.10 (1 H, m). ^{19}F NMR (500 MHz, $\text{C}_2\text{D}_2\text{Cl}_4$): δ (ppm) -81.1 (3F, b), -101.4 (2F, b), -121.6 (2F, b), -121.8 (2F, b), -123.0 (2F, b), -126.3 (2F, b). Elemental analysis calculated for $\text{C}_{22}\text{H}_9\text{F}_{13}\text{S}_4$: C, 40.74, H, 1.40, F, 38.08%. Found: C, 39.89, H, 1.51, F, 37.59%.

5-(perfluorohexyl)-2,2':5,2'':5'',2''':5''',2''''':5''''',2''''''-sexithiophene (FH-6T): A mixture of 5-bromo-5'-perfluorohexyl-2,2'-bithiophene (0.23 g, 0.41 mmol), [2,2':5,2'':5'',2''':5''',2''''':5''''',2''''''-quaterthiophen]-5-yltributylstannane (0.22 g, 0.36 mmol), $\text{Pd}(\text{PPh}_3)_4$ (0.02 g, 0.018 mmol) and 8 mL DMF was purged with argon for 0.5 h and then stirred at 90 °C for 5 h. The reaction mixture was cooled to rt and filtered to collect the orange precipitate. The crude product was washed with 50 mL ethanol, 50 mL diethyl ether and dried under vacuum. Vacuum sublimation afforded the product (0.13 g, 44%) as a bright orange solid. ^1H NMR (500 MHz, $\text{C}_2\text{D}_2\text{Cl}_4$, 110 °C): δ (ppm) 6.78 (1H, d, $J = 3.5$ Hz), 6.66 (1H, d, $J = 5.0$ Hz), 6.62-6.59 (3 H, m), 6.56-6.52 (7 H, m), 6.45 (1 H, dd, $J = 5.0$, 4.0 Hz). ^{19}F NMR (500 MHz, $\text{C}_2\text{D}_2\text{Cl}_4$, 110 °C): δ (ppm) -80.9 (3F, b), -100.4 (2F, b), -120.8 (2F, b), -121.0 (2F, b), -122.3 (2F, b), -125.5 (2F, b). Elemental analysis calculated for $\text{C}_{30}\text{H}_{13}\text{F}_{13}\text{S}_6$: C, 44.33, H, 1.61, F, 30.39%. Found: C, 44.42, H, 1.71, F, 30.59%.

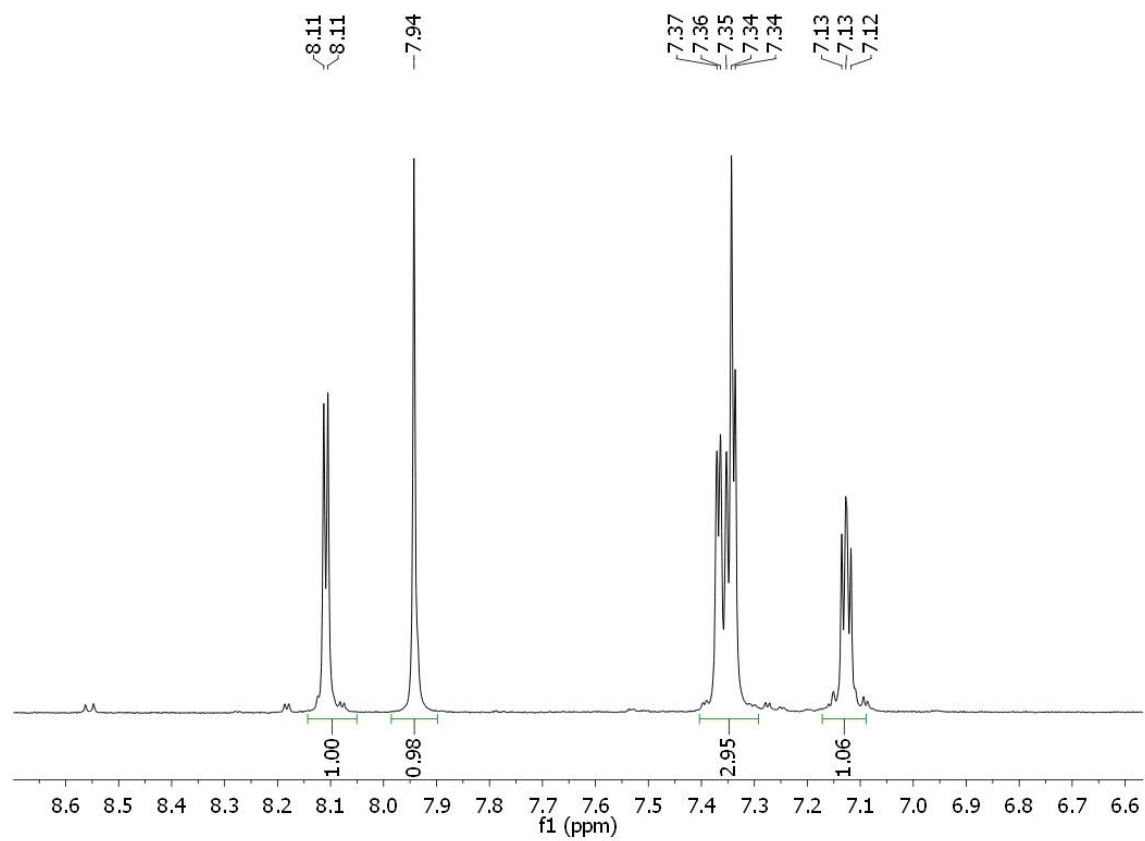
Appendix



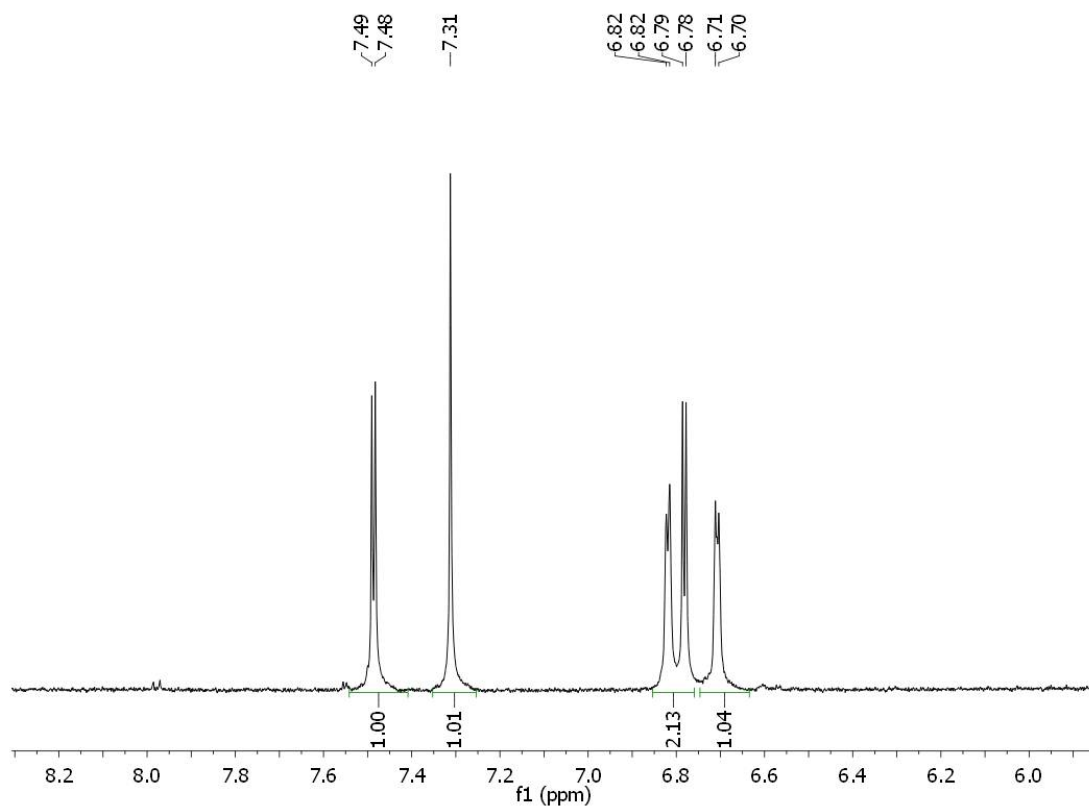
^1H NMR Spectrum of DFH-5T (500 MHz, $\text{C}_2\text{D}_2\text{Cl}_4$, 110 $^\circ\text{C}$)



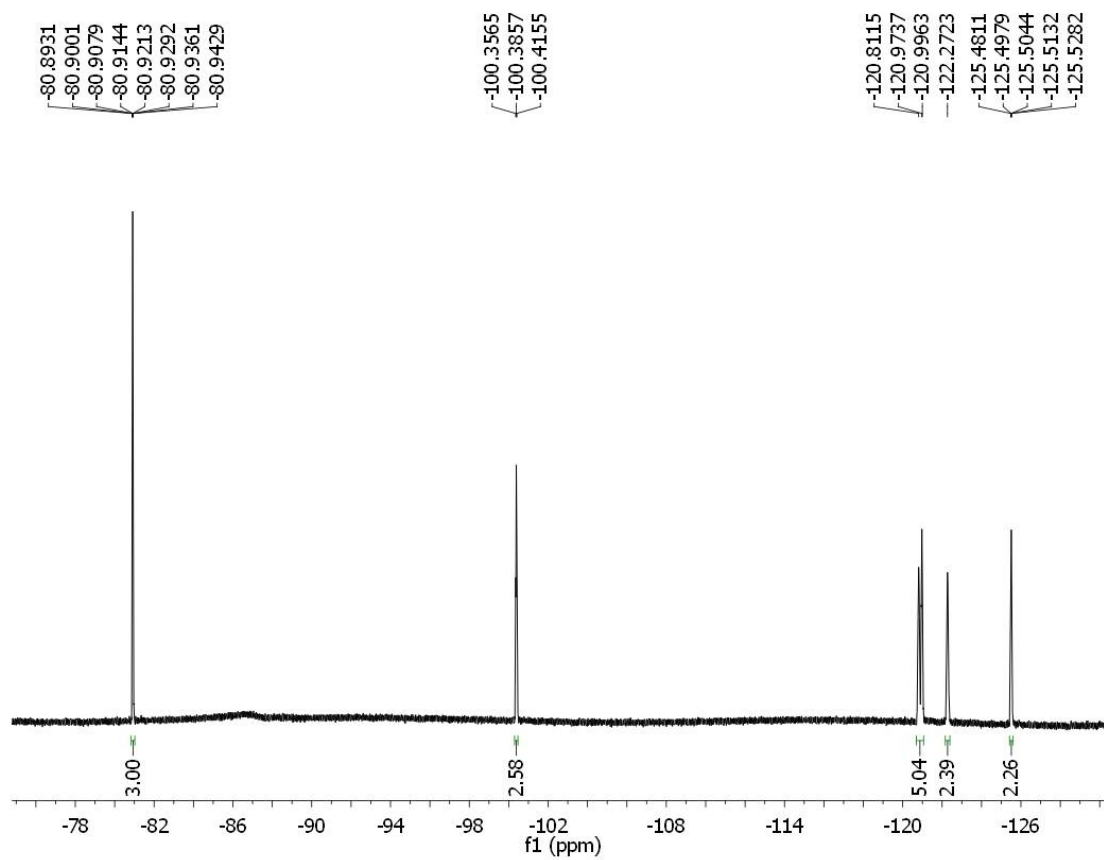
^{19}F NMR Spectrum of DFH-5T (500 MHz, $\text{C}_2\text{D}_2\text{Cl}_4$, 110 °C)



^1H NMR Spectrum of 4T-BTD (500 MHz, CD_2Cl_2)



^1H NMR Spectrum of DFH-4T-BTD (500 MHz, $\text{C}_2\text{D}_2\text{Cl}_4$, 110 $^\circ\text{C}$)



^{19}F NMR Spectrum of DFH-4T-BTD (500 MHz, $\text{C}_2\text{D}_2\text{Cl}_4$, 110 °C)

References

- 1) Murphy, A. R.; Fréchet, J. M. J. *Chem. Rev.* **2007**, *107*, 1066
- 2) Horowitz, G.; Fichou, D.; Peng, X.; Xu, Z.; Garnier, F. *Solid State Commun.* **1989**, *72*, 381
- 3) Anthopoulos, T. D. ; de Leeuw, D. M. ; Cantatore, E. ; Setayesh, S. ; Meijer, E. J. ; Tanase, C. ; Hummelen, J. C. ; Blom, P. W. M. *Appl. Phys. Lett.* **2004**, *85*, 4205
- 4) Mas-Torrent, M. ; Rovira, C. *Chem. Soc. Rev.* **2008**, *37*, 827
- 5) Yan, H. ; Chen, Z. ; Zheng, Y. ; Newman, C. ; Quinn, J. R. ; Dötz, F. ; Kastler, M. ; Facchetti, A. *Nature* **2009**, *457*, 679
- 6) Facchetti, A.; Deng, Y.; Wang, A. C.; Koide, Y.; Sirringhaus, H.; Marks, T. J.; Friend, R. H. *Angew. Chemie. Int. Ed.* **2000**, *39*, 4547
- 7) Facchetti, A.; Mushrush, M.; Katz, H. E.; Marks, T. J. *Adv. Mater.* **2003**, *15*, 33
- 8) Facchetti, A.; Yoon, M. H.; Stern, C. L.; Hutchison, G. R.; Ratner, M. A.; Marks, T. J. *J. Am. Chem. Soc.* **2004**, *126*, 13480
- 9) Facchetti, A.; Mushrush, M.; Yoon, M. H.; Hutchison, G. R.; Ratner, M. A.; Marks, T. J. *J. Am. Chem. Soc.* **2004**, *126*, 13859
- 10) Facchetti, A. *Chem. Mater.* **2011**, *23*, 733.
- 11) Yoon, M.-H.; DiBenedetto, S. A.; Facchetti, A.; Marks, T. J. *J. Am. Chem. Soc.* **2005**, *127*, 1348
- 12) Yoon, M.-H.; DiBenedetto, S. A.; Russell, M. T.; Facchetti, A.; Marks, T. J. *Chem. Mater.* **2007**, *19*, 4864
- 13) Le, Y.; Nitani, M.; Ishikawa, M.; Nakayama, K.; Tada, H.; Kaneda, T.; Aso, Y. *Org. Lett.* **2007**, *9*, 2115
- 14) Didier, D.; Sergeyev, S.; Geerts, Y. H. *Tetrahedron* **2007**, *63*, 941
- 15) McCairn, M. C.; Turner, M. L. *Tetrahedron Lett.* **2007**, *48*, 1045
- 16) Mullekom, H. A. M.; Vekemans, J. A. J. M.; Meijer, E. W. *Chem. Eur. J.* **1998**, *4*, 1235
- 17) Agrawal, A. K.; Jenekhe, S. A. *Macromolecules* **1993**, *26*, 895
- 18) Yamamoto, T.; Zhou, Z.; Kanbara, T.; Shimura, M.; Kizu, K.; Maruyama, T.; Nakamura, Y.; Fukuda, T.; Lee, B.-L.; Ooba, N.; Tomaru, S.; Kurihara, T.; Kaino, T.; Kubota, K.; Sasaki, S. *J. Am. Chem. Soc.* **1996**, *118*, 10389
- 19) Berlaman, I. B. *Fluorescence Spectra of Aromatic Molecules*; Academic Press: New York, 1971

- 20) Hotta, S.; Katagiri, T. *J. Heterocyclic Chem.* **2003**, *40*, 845
- 21) Matharu, A. S.; Cowling, S. J.; Wright, G. *Liq. Cryst.* **2007**, *34*, 489

CHAPTER 5

Synthesis, Crystal Structures, and Electronic Properties of Nonlinear Fused Thienoacene Semiconductors

5.1 Introduction

Fused polycyclic aromatic compounds are at the forefront of organic semiconductor (OSC) research due to their high charge mobilities. Some of the highest hole mobilities for OSCs have been discovered using single crystals of fused acenes such as pentacene¹ and rubrene.² Efficient charge transport within these materials is attributed to their planar structures and extended π -conjugation which leads to good π - π overlap in the solid state. Thienoacene compounds have also emerged as high performance semiconductors due to their high charge mobilities and improved stabilities compared to acenes.^{3,4,5,6,7} The aromatic ring connectivity has been shown to greatly affect the HOMO orbital geometries and crystal structures for thienoacene compounds⁸, properties that dictate charge mobility. Therefore, significant research has been directed toward understanding structure property relationships within thienoacene materials.

As described in chapter 1, the rate of electron transfer between nearest neighbors in an organic crystal is related to the molecular reorganization energy and the transfer integral. The transfer integral describes the electronic communication between molecular orbitals of nearest neighbors, and can be estimated from density functional theory calculations with knowledge of the crystal structure. Calculated transfer integrals for several thienoacenes in the literature are shown in Figure 5.1. Clearly the transfer integrals are very sensitive to small changes in the molecular structure. Substitution of

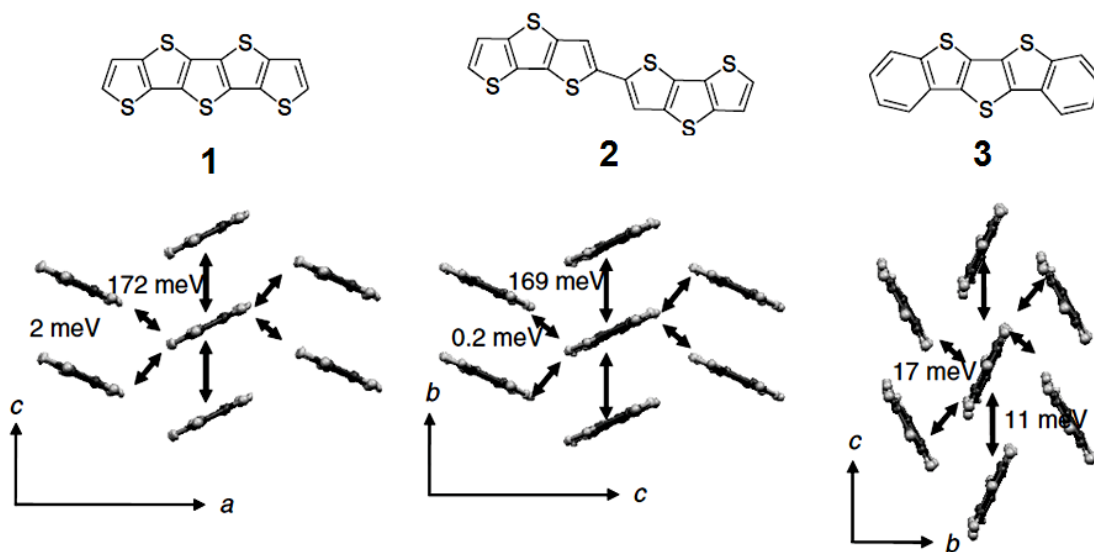


Figure 5.1 Crystal structures and transfer integrals for selected thienoacenes in the literature. Figure adapted from reference 8

the peripheral thiophene rings in compound **1** for phenyl rings in compound **3** drastically changes the transfer integral. Compound **1** exhibits good π - π overlap in the direction of the c-axis, leading to a very high transfer integral of 172 meV. On the other hand compound **3** shows a more pronounced herringbone crystal structure which reduces π - π overlap and reduces the transfer integral by more than one order of magnitude. Based off these transfer integrals alone one could expect the charge mobility of compound **1** to be significantly greater than that of **3** in the direction of the c-axis. For this reason some efforts have been made to engineer materials that exhibit face-to-face π -stacking crystal structures. For example this was achieved by alternating electron rich and electron deficient aromatic rings to induce overlap between the two units.⁹ However, experiments on thienoacene isomers **4** and **5** have shown that high charge mobilities result from balanced transport pathways in more than one dimension.¹⁰ Compound **4** showed a crystal structure defined by tight π stacks with an angle between the stacks close to zero

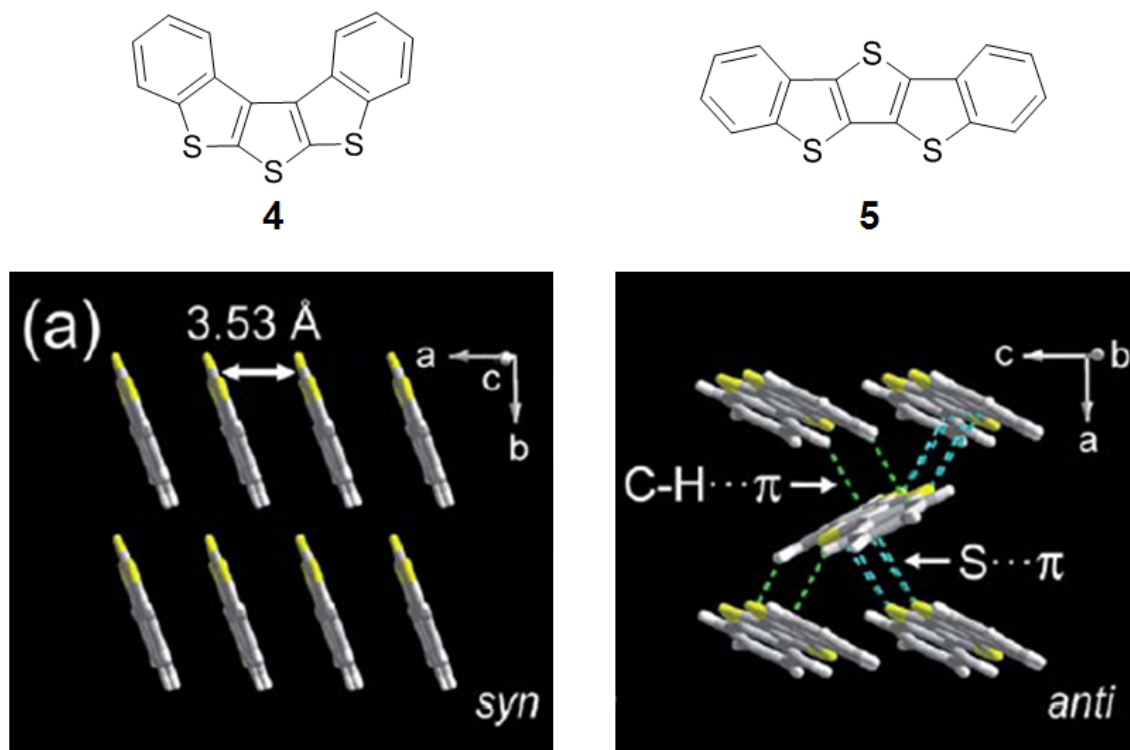


Figure 5.2 Structures and crystal analysis of thienoacene compounds **4** and **5**. Figure adapted from reference 10.

(Figure 5.2). This structure led to a relatively high transfer integral of 73 meV in the direction of π -stacks but very small transfer integrals (< 10 meV) in the other directions. Compound **5** showed a typical herringbone crystal structure with more balanced transfer integrals in two dimensions. The hole mobility of compound **5** ($1.4 \text{ cm}^2/\text{Vs}$) was almost four times as high as that of **4** ($0.4 \text{ cm}^2/\text{Vs}$) when single crystal transistors were fabricated for both compounds. This difference in charge mobility was attributed to the two-dimensional transport properties within the herringbone structure of **5**. These findings showed that the herringbone crystal structure is in fact advantageous over a π -stack structure for achieving high charge mobilities.

The vast majority of thienoacene semiconductors have been constructed with a linear or semi-linear connectivity of aromatic rings. Expansion of the π -system into two

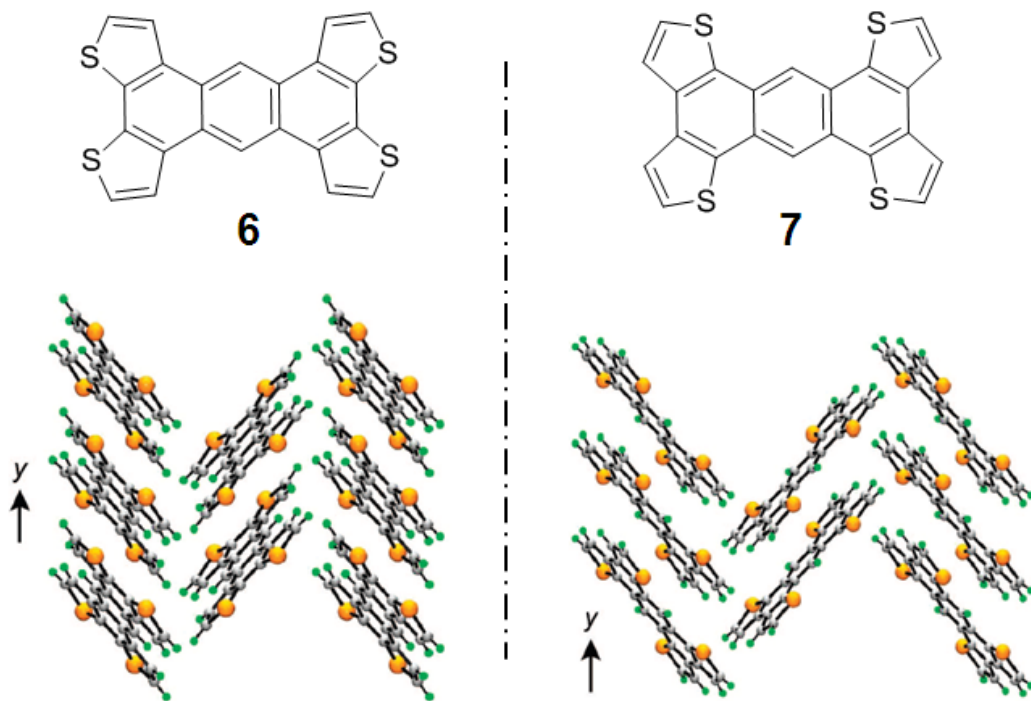


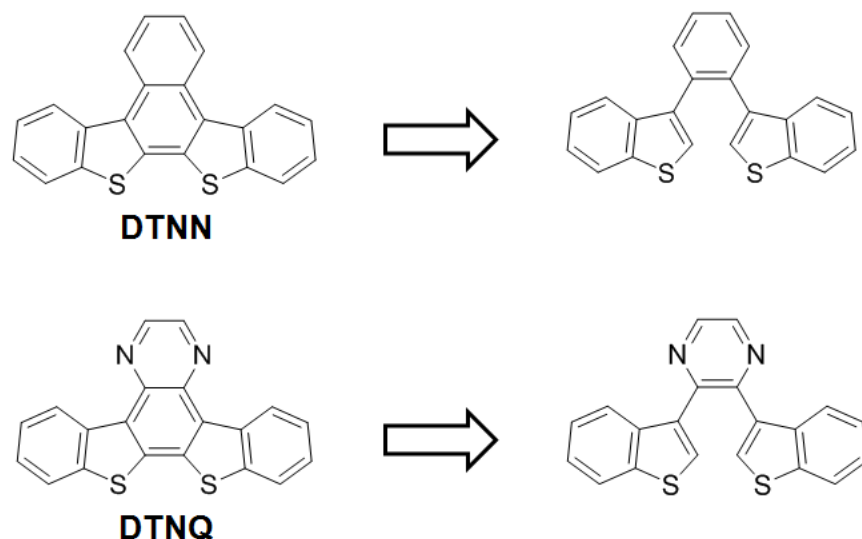
Figure 5.3 Crystal structures of tetrathienoacene compounds 6 and 7. Figure adapted from reference 11

dimensions is an interesting route for achieving extended π molecular orbitals, and could result in improved charge mobilities for thienoacene compounds. A notable example of thienoacenes with a two-dimensional structure are shown in Figure 5.3, prepared by Brusso *et al.*¹¹ Both isomers showed good π - π overlap along the stacking direction but retained the herringbone structure favorable for two dimensional charge transport. Field effect transistors were fabricated using analogous compounds with hexyl chains at the 2 positions of the thiophene rings. The compounds could be deposited from solution or through vacuum sublimation and showed charge mobilities on the order of $10^{-2} \text{ cm}^2/\text{Vs}$. Furthermore the fused compounds assembled on graphite surfaces to form highly ordered two dimensional monolayers.

This chapter presents the synthesis and properties of a new class of thienoacene semiconductors with two-dimensional ring connectivity. The crystal structures of the compounds have been analyzed and related to the self-assembly properties of the new materials. Field effect transistors were fabricated and the device characteristics are discussed.

5.2 Synthesis

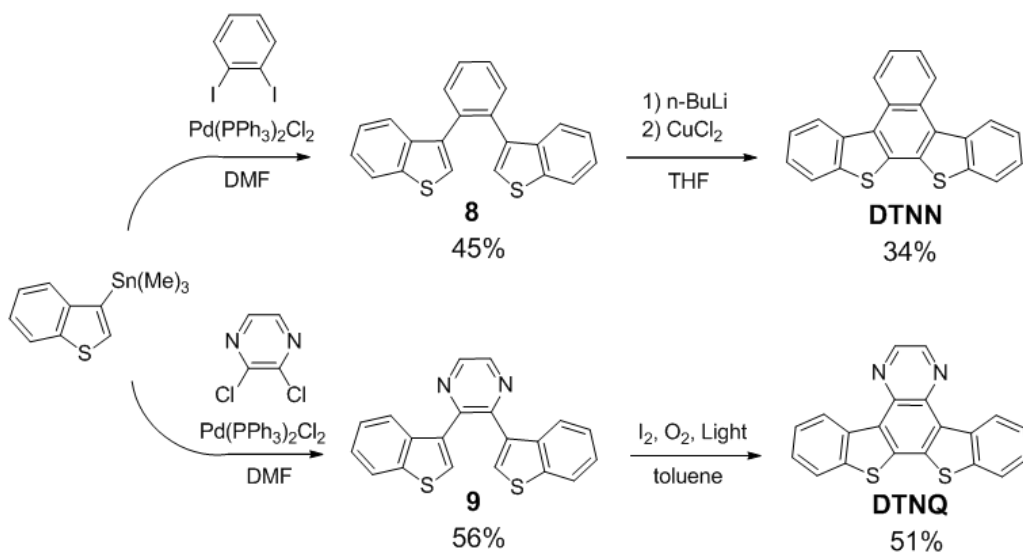
Thienoacenes with two-dimensional ring connectivity could lead to better molecular orbital overlap in the solid state as a result of the extended π molecular orbitals. The two compounds in scheme 5.1 were designed to explore this two-dimensional structural motif. In the retrosynthesis of naphtho[2,1-*b*:3,4-*b'*]bis[1]benzothiophene (DTNN) and quinoxalo[6,5-*b*:7,8-*b'*]bis[1]benzothiophene (DTNQ) the central carbon-carbon bond was formed in the last step. This ensured good solubility of the precursors and allowed the use of easily accessible benzothiophene derivatives as starting materials.



Scheme 5.1 Target thienoacene compounds and retrosynthetic pathway

Compound DTNN (Scheme 5.1) is isoelectronic with the two-dimensional hydrocarbon benzo[*s*]picene, a material which has not yet been explored for semiconductor applications.¹² Compound DTNQ incorporates a pyrazine ring in order to study the effects of nitrogen incorporation on the thienoacene system. Pyrazine rings have previously been shown to effectively modulate HOMO and LUMO energies in fused acenes,^{13,14} but nitrogen incorporation has been very limited within thienoacene structures.

A similar synthetic route was used to construct both molecules, although different reactions were utilized in the aromatic cyclization (Scheme 5.2). Photocyclooxidation was ideal for compound DTNQ since the reaction only requires solvent and catalytic iodine and leads to a pure crude product free of metals. Attempts to photocyclize compound **1** resulted in poor conversion, therefore, DTNN was synthesized using the copper promoted coupling of dilithiated **1**. Using these routes both compounds could be prepared in gram quantities within a matter of days. DTNN was previously synthesized using a different route via Nagao *et al.*, but was not studied as a semiconductor.¹⁵



Scheme 5.2 Synthetic route for compounds DTNN and DTNQ

5.3 Crystal Structure Analysis

Crystal structure analysis is an important tool for considering charge transport in organic semiconductors, since charge mobility is dependent on electronic communication between nearest neighbors in the solid state. Single crystals as large as 3 mm were easily obtainable for both compounds during purification steps. Crystals of DTNN were obtained via recrystallization from toluene whereas DTNQ crystals were grown through sublimation.

The crystallographic data is summarized in Table 5.1. Compound DTNN crystallizes in the C_2/c spacegroup with eight molecules in the unit cell while DTNQ crystallizes in P_{21}/n with only four molecules in the unit cell (Figure 5.4). However, the molecular packing of the two compounds is remarkably similar. Both compounds exhibit a layered structure comprised of tight π -stacks aligned along the b -axis, arranged into herringbone arrays (Figure 5.5). DTNN has a slight molecular curvature with maximum torsion angle of 3.9° , while DTNQ is completely planar.

Table 5.1 Crystallographic data for DTNN and DTNQ

	DTNN	DTNQ
space group	C_2/c	P_{21}/n
a (Å)	38.108	20.351
b (Å)	3.838	3.788
c (Å)	21.281	21.243
β (deg)	108.880	118.588
τ (deg)	70.59	77.90
δ (Å)	3.488	3.479
pitch (deg)	15.81	6.87
Roll (deg)	20.31	21.69

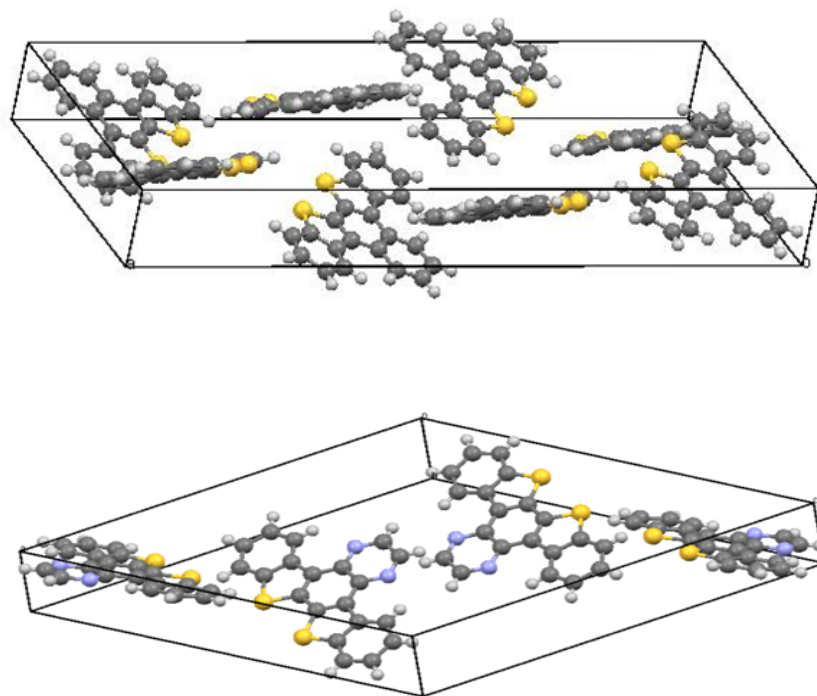


Figure 5.4 Unit cells of DTNN (top) and DTNQ (bottom)

Compared to other thienoacenes, DTNN and DTNQ have large τ values, the angle between the molecular plane and the stacking axis. This, combined with the small pitch and roll angles for both compounds, leads to large π -overlap within the stacking direction. The molecular stacking distance along the b -axis is only ≈ 3.48 Å for both compounds, further demonstrating the strong intermolecular interactions within these solids. While both compounds exhibit exceptional π - π interactions, the crystal structures retain the herringbone motif which is favorable for two-dimensional charge transport.

Unlike most other thienoacenes, DTNN and DTNQ have both sulfur atoms on the same side of the ring, leading to isolated sulfur interactions in the crystal structure. Thus, sulfur is not expected to play a large role in charge transport for these materials. In fact, DTNN does not have any sulfur contacts less than the sum of the Van der Waals radii. In contrast DTNQ has a short S-S (3.553 Å) contact, and also possesses a short S-C

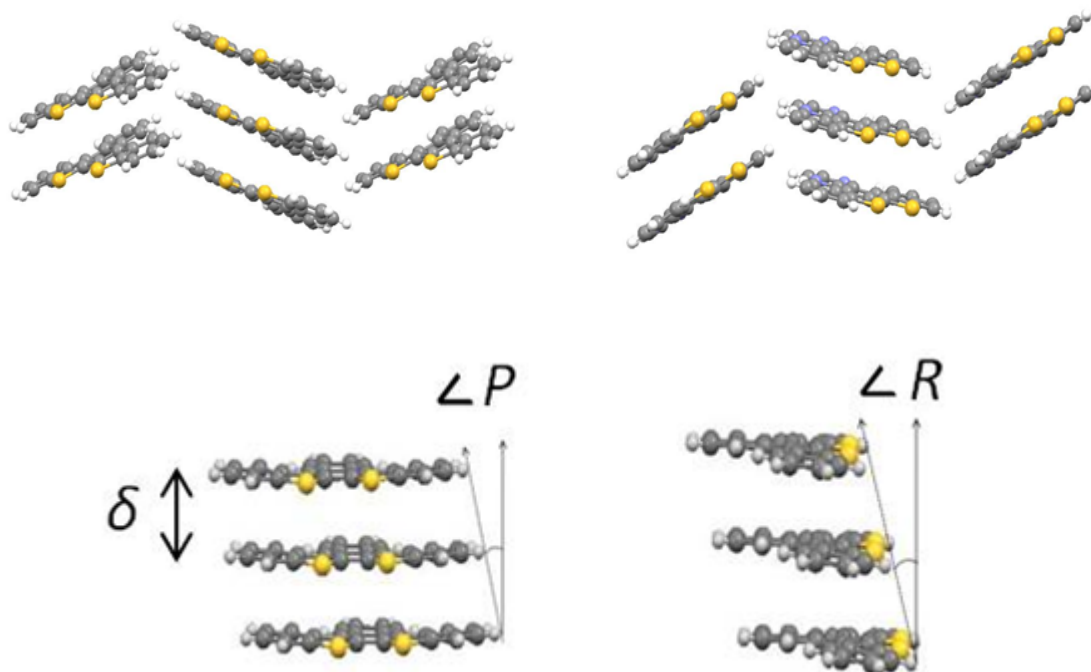


Figure 5.5 Herringbone structures of DTNN (top left) and DTNQ (top right) and illustration of δ , P° , and R°

contact (3.494 Å) within the π -stacking direction. The pitch angle for DTNQ is less than half of that for DTNN, increasing the amount of π - π interactions in the stacking direction. In addition, nitrogen atoms in DTNQ show hydrogen bonding, leading to tighter packing and a slight increase in the density of the solid ($\rho = 1.536 \text{ mg/mm}^3$ for DTNN, $\rho = 1.582 \text{ mg/mm}^3$ for DTNQ). Thus, nitrogen incorporation leads to increased intermolecular interactions in the solid state.

5.4 Optical/Electrochemical Properties

UV/vis spectra were acquired for both compounds in THF solutions (Figure 5.6). Both compounds are wide band-gap semiconductors with optical band-gaps of 3.33 eV for DTNN and 2.97 eV for DTNQ. DTNN is a white solid whereas DTNQ is yellow. Both

compounds show two maxima in the near UV resulting from vibronic coupling of the π - π^* transition. This behavior is common for rigid thienoacenes which have limited conformational disorder as a result of their fused structures.¹⁶ The quinoxaline ring in DTNQ leads to a large reduction of the band gap (0.36 eV) as a result of the donor-acceptor like structure.

The cyclic voltammogram of DTNN showed two quasi-reversible oxidation peaks while DTNQ showed one quasi-reversible oxidation peak. HOMO levels were estimated from the onset of the first oxidation peak, giving -5.93 eV for DTNN and -6.26 eV for DTNQ. The nitrogen rich quinoxaline ring in DTNQ therefore stabilizes the HOMO by -0.33 eV. Compared to other thienoacene compounds the HOMO levels of DTNN and DTNQ are exceptionally low.⁸ This is a result of the two-dimensional aromatic ring connectivity, which results in diminished aromaticity and a lower lying HOMO.^{8,17} DTNN and DTNQ are exceptionally low LUMO levels were estimated from the electrochemical HOMO plus the optical band gap to give -2.60 eV for DTNN and -3.29 eV for DTNQ.

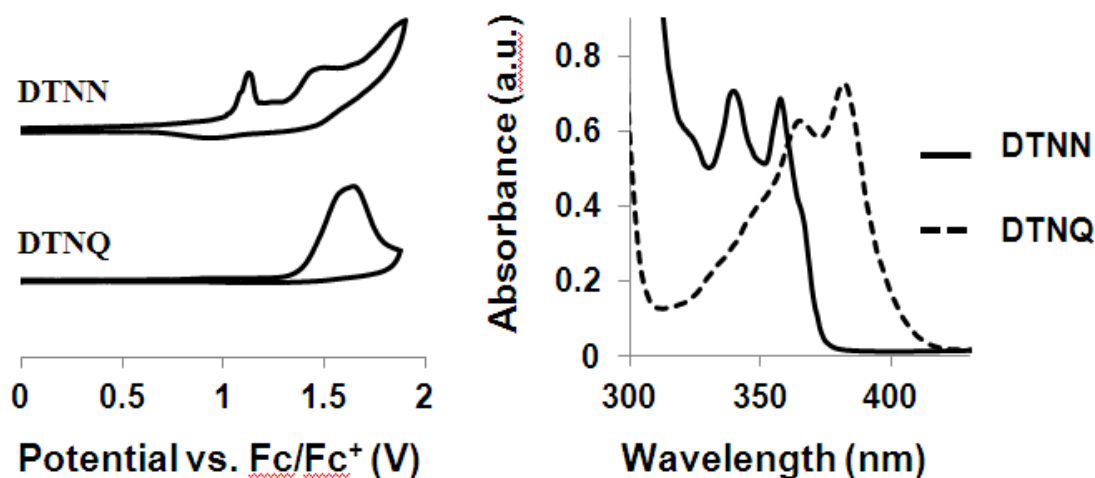


Figure 5.6 Oxidative cyclic voltammograms (left) and UV/vis spectra in THF solutions (right)

Thus, incorporation of the nitrogen rich ring leads to a much larger reduction in LUMO (0.69 eV) than HOMO (0.33 eV). This finding suggests that increasing the nitrogen content in structurally similar compounds could lead to very low LUMO levels and may be a useful strategy for the design of n-type semiconductors.

5.5 Density Functional Theory Calculations

HOMO/LUMO energies and geometries were calculated at the B3LYP/6-311+G* level of theory. HOMO orbital surfaces show large extended lobes on the thiophene

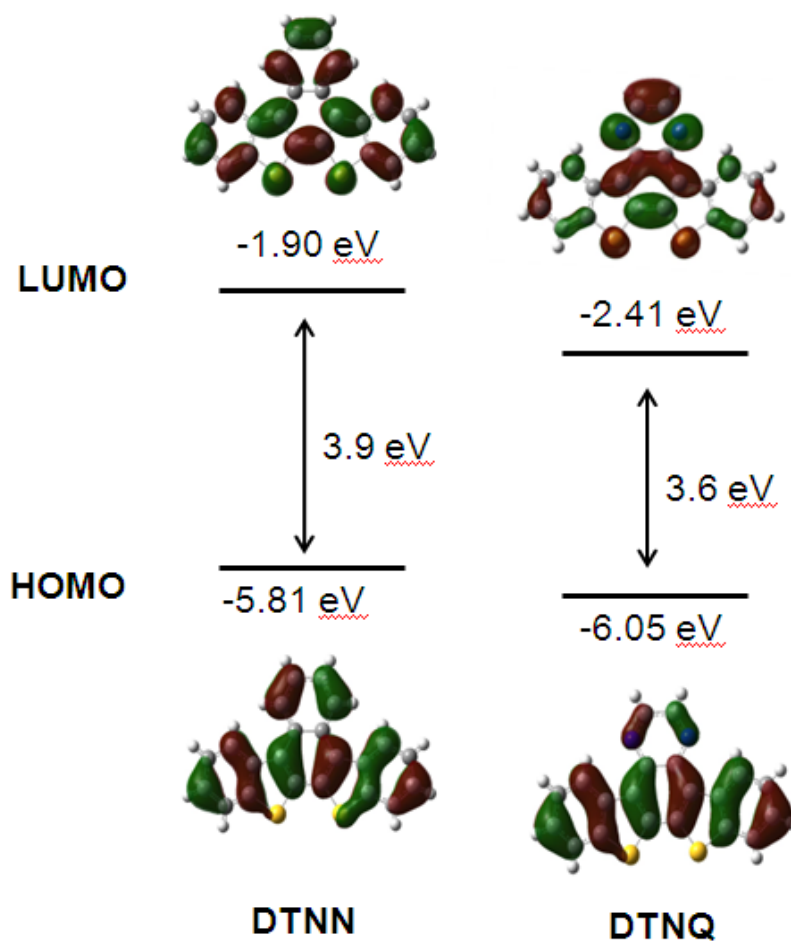


Figure 5.7 Calculated frontier molecular orbitals of DTNN and DTNQ

rings for both compounds (Figure 5.7). Contribution from sulfur to the HOMO is small compared to other thienoacenes. The electron distribution is spread evenly in two dimensions for DTNN, whereas DTNQ has a HOMO that is slightly more localized on the lower five rings. The calculated HOMO energies are slightly higher than the electrochemical data, but still very low compared to other thienoacenes. The calculated band gaps are larger than those estimated from the absorption spectra, but the trends observed going from DTNN to DTNQ are consistent with the experimental data. The LUMO of DTNQ shows significant stabilization from the nitrogen rich quinoxaline with a large quinoidal lobe in the center of the compound.

5.6 Thin Film Morphology

Scanning electron microscopy (SEM) was used to study the morphologies that arise from vapor deposition of the two compounds. Films were grown via sublimation onto an octyltrichlorosilane treated Si/SiO_x wafer (Figure 5.8). Film thicknesses were 80-100 nm, consisting of well defined crystals between 2-8 μm in length. The high aspect ratio of the crystals clearly demonstrates preferred growth parallel to the plane of the substrate. This is consistent with growth along the *b* axis, which is considerably shorter than the other axes of the unit cell for both compounds. The distinct crystallites shown in Figure 5.8 are not typical structures for thienoacene thin films, which more often form continuous films comprised of terrace like grains.^{5,18,19} The one dimensional self-assembly of DTNN and DTNQ could be useful for the construction of discrete semiconducting components (i.e. molecular wires). Formation of such well-defined crystallites is mainly attributed to highly preferred growth along the short *b*-axis, which is comprised of strong π -stacks. Similar

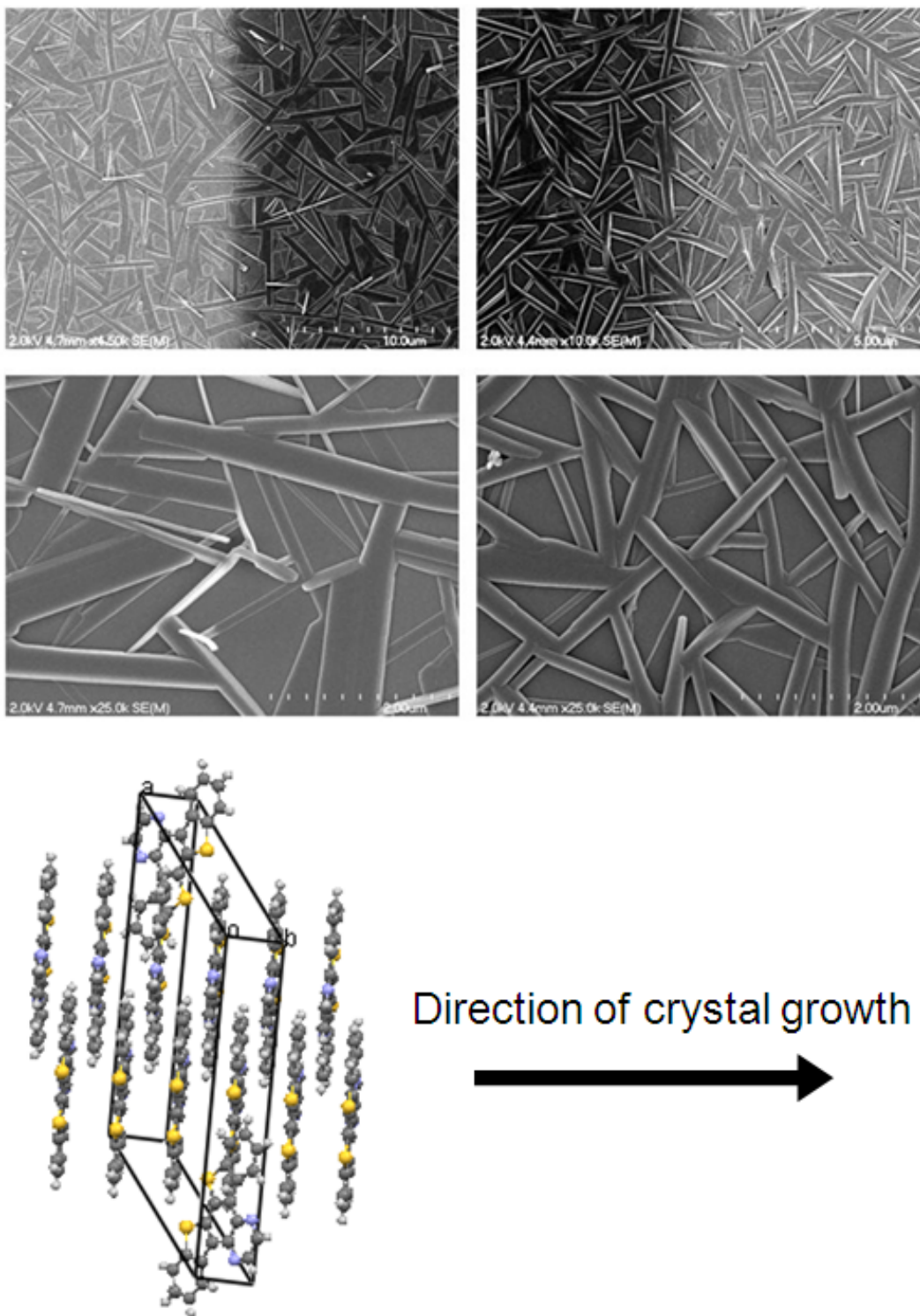


Figure 5.8 Top: SEM images of DTNN (left) and DTNQ (right) films. Lighter regions in top images are the gold source/drain electrodes. Bottom: Illustration of crystal growth along *b*-axis for DTNQ

behavior was reported for a sickle shaped thienoacene that possessed a similarly short *a*-axis (3.883 Å), as well as a similar molecular stacking distance (3.53 Å).¹⁰ The preferred growth along the *b*-axis, which occurs in the plane of the substrate, results in π -stacks within the direction of charge transport. However, the observed films show many grain boundaries, some of which join two crystallites at large angles close to 90°.

5.7 Field Effect Transistor Characterization

Top contact-bottom gate FET devices were fabricated in order to study the charge mobility of DTNN and DTNQ. P-type field effect behavior was observed for both compounds (Figure 5.9). Output characteristics show deviation from linearity at low V_{SD} for both compounds, indicating some contact resistance. This is likely due to significant charge injection barriers as a result of the large energy difference between the work function of gold and the HOMO levels of the semiconductors. This is most apparent for DTNQ which has a very large ΔE (> 1.0 eV). Theoretical work has shown that the work function of gold can be significantly altered by employing self-assembled monolayers.²⁰ This may be a useful strategy for improving charge injection barriers for DTNN and DTNQ.

Average hole mobilities for the two compounds were found to be identical at 3.0×10^{-3} cm²/Vs. Charge transport is therefore very similar within these two materials, a direct result of their similar HOMO orbital geometries, crystal structures, and thin film morphologies. These hole mobilities are relatively modest compared to other thienoacenes.⁸ However, we note that the obtained thin film morphologies are not ideal for charge transport, and likely restrict mobility due to limited surface coverage and large angle grain boundaries. On/off currents for devices were between 10^5 - 10^6 while

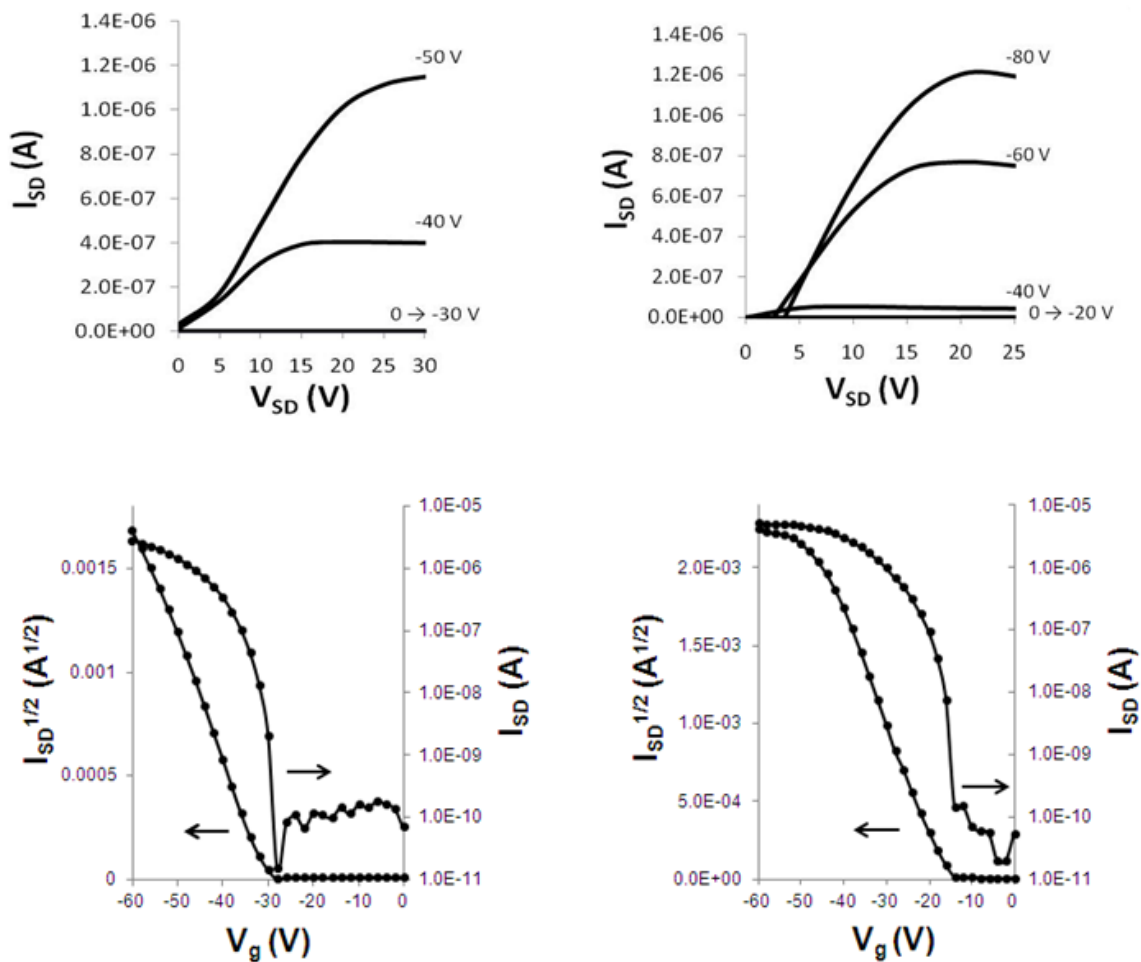


Figure 5.9 Output (top) and transfer (bottom) characteristics of DTNN (left) and DTNQ (right)

threshold voltages were not stable, shifting to larger values from scan to scan. The low HOMO levels of DTNN and DTNQ are expected to result in very stable materials, and the instability of V_T is likely due to adsorption of H_2O/O_2 on the exposed dielectric.

Significant improvements in the device characteristics are likely possible by further optimization of the device fabrication process. The primary factors that require improvement are 1) contact resistance at the Au/semiconductor interface and 2) the discontinuous morphology. Both of these problems could be addressed by further experimentation with self-assembled monolayers, both on the source/drain electrodes and on the dielectric. In addition, the film morphology could likely be improved by

controlling the evaporation rate as well as the substrate temperature during the organic deposition.

5.8 Conclusion

In conclusion, two new thienoacene semiconductors with two-dimensional ring connectivity were synthesized. The compounds crystallize into the common herringbone motif and exhibit exceptional π - π overlap. Strong π - π interactions in the solid leads to self-assembly into well-defined one-dimensional microcrystals upon sublimation. Similar FET properties were observed for both compounds with hole mobilities of $3.0 \times 10^{-3} \text{ cm}^2/\text{Vs}$ and $I_{\text{on/off}}$ of 10^5 - 10^6 . We expect that improvements in charge mobilities for these compounds will be possible through further optimization of the thin film morphology and device geometry. In particular, fabrication of single crystal field effect transistors are of interest in order to probe the intrinsic charge transport properties of the new semiconductors.

5.9 Experimental

Materials. All chemicals and reagents were used as received unless otherwise noted. Tetrahydrofuran was distilled over sodium prior to use. The starting material 3-(trimethylstannyl)-benzothiophene was synthesized according to the reported procedure.²¹

Instrumentation and OFET device fabrication. UV/vis spectra were acquired using a Varian Cary 50 UV/Vis spectrometer. Melting points and thermal transitions were analyzed using a TA instruments Q200 differential scanning calorimeter. Cyclic voltammetry was performed using a Bioanalytical Systems (BAS) Epsilon potentiostat equipped with a standard three-electrode configuration. Scans were performed on

oligomer films evaporated onto a glassy carbon electrode which served as the working electrode. A Pt wire was used as counter electrode and an Ag/AgNO₃ (0.01 M in anhydrous acetonitrile) was used as the reference electrode. Measurements were performed in anhydrous acetonitrile with tetrabutylammonium hexafluorophosphate (0.1 M) as supporting electrolyte under nitrogen at a scan rate of 100 mV/s. Internal calibration of the reference potential was achieved using the ferrocene/ferrocenium redox couple. HOMO levels were calculated using the following equation.

$$HOMO = -(E^{\text{ox}} + 4.8) \text{ (eV)}$$

Top Contact OFETs were fabricated on heavily *p*-doped Si (B, $\rho = 1\text{-}30 \text{ Ohm cm}$), with a 100 nm thermal oxide as dielectric ($C_i = 3.45 \times 10^{-8} \text{ F/cm}^2$). Wafers were first cleaned by UV/ozone, then submerged into a 0.1 M toluene solution of octyltrichlorosilane at 70 °C for 30 min to form the hydrophobic self-assembled monolayer. Prior to device fabrication DTNN was purified by recrystallizing from toluene three times. DTNQ was purified by sublimating the compound twice. Vacuum deposition of the organic semiconductors was performed using a homemade evaporation system (schlenk line, < 0.1 torr). During deposition the FET substrate was heated to a temperature of $\approx 75 \text{ }^\circ\text{C}$ ($\pm 10 \text{ }^\circ\text{C}$) by conduction from the base heat source. Film thicknesses were measured after deposition via profilometry. Devices were completed by sputtering a 20 nm thick gold film through a shadow mask to define the source and drain electrodes. Sputtering was done using a Kurt Lesker PVD 75 magnetron sputtering system. The substrates were kept still while the gold was sputtered at 0.5 Å/s. SEM images were taken from devices that had an additional 2.0 nm Au/Pd film sputtered over

the entire substrate. Images were obtained using a Hitachi S-4700 cold cathode field emission microscope.

Synthesis.

1,2-bis(benzo[b]thiophen-3-yl)benzene (8). To a round bottom flask was added 3-(trimethylstannyl)-benzothiophene (6.08 g, 20.5 mmol), 1,2-diiodobenzene (2.93 g, 8.90 mmol), Pd(PPh₃)₄ (0.95 g, 0.82 mmol), CuI (0.156 g, 0.82 mmol), CsF (5.4 g, 35.6 mmol), and 50 mL DMF. The mixture was purged with argon for 30 min, brought to 100 °C and stirred overnight. The reaction was cooled to rt, H₂O (50 mL) and diethyl ether (50 mL) were added to the flask, and the two layers were poured into a separatory funnel. The aqueous layer was extracted with ether (2 x 30 mL), and the combined organics were washed with H₂O (4 x 30 mL) and brine (1 x 30 mL). The organic layer was dried with MgSO₄, filtered, and concentrated under reduced pressure. The crude product was precipitated by addition of ether/hexanes (1:2, 15 mL), then collected and washed with methanol. Recrystallization from CH₂Cl₂/MeOH afforded the pure product as a white solid (1.36 g, 45%). M.p. = 121-122 °C. ¹H NMR (300 MHz, CDCl₃): δ (ppm) 7.81 (2H, d, *J* = 7.5 Hz), 7.57-7.70 (6H, m), 7.22-7.33 (4H, m), 7.04 (2H, s). ¹³C NMR (300 MHz, CDCl₃): δ (ppm) 139.6, 138.5, 136.4, 135.4 131.0, 127.7, 124.5, 124.0, 123.9, 122.6, 122.5. IR (neat) ν 1453 cm⁻¹. Elemental analysis calculated for C₂₂H₁₄S₂: C, 77.15, H, 4.12%. Found: C, 77.27, H, 4.21%.

Synthesis of 2,3-bis(benzo[b]thiophen-3-yl)pyrazine (9). To a round bottom flask was added 3-(trimethylstannyl)-benzothiophene (0.80 g, 2.70 mmol), 2,3-dichloropyrazine (0.17 g, 1.18 mmol), Pd(PPh₃)₂Cl₂ (0.050 g, 0.07 mmol), and 5 mL DMF. The mixture was purged with argon for 30 min, warmed to 120 °C and stirred for 3 hr. The reaction was cooled to rt and poured into a separatory funnel with 10 mL diethyl ether and 10 mL sat. NaHCO₃ (aq.). The aqueous layer was extracted with ether (2 x 15

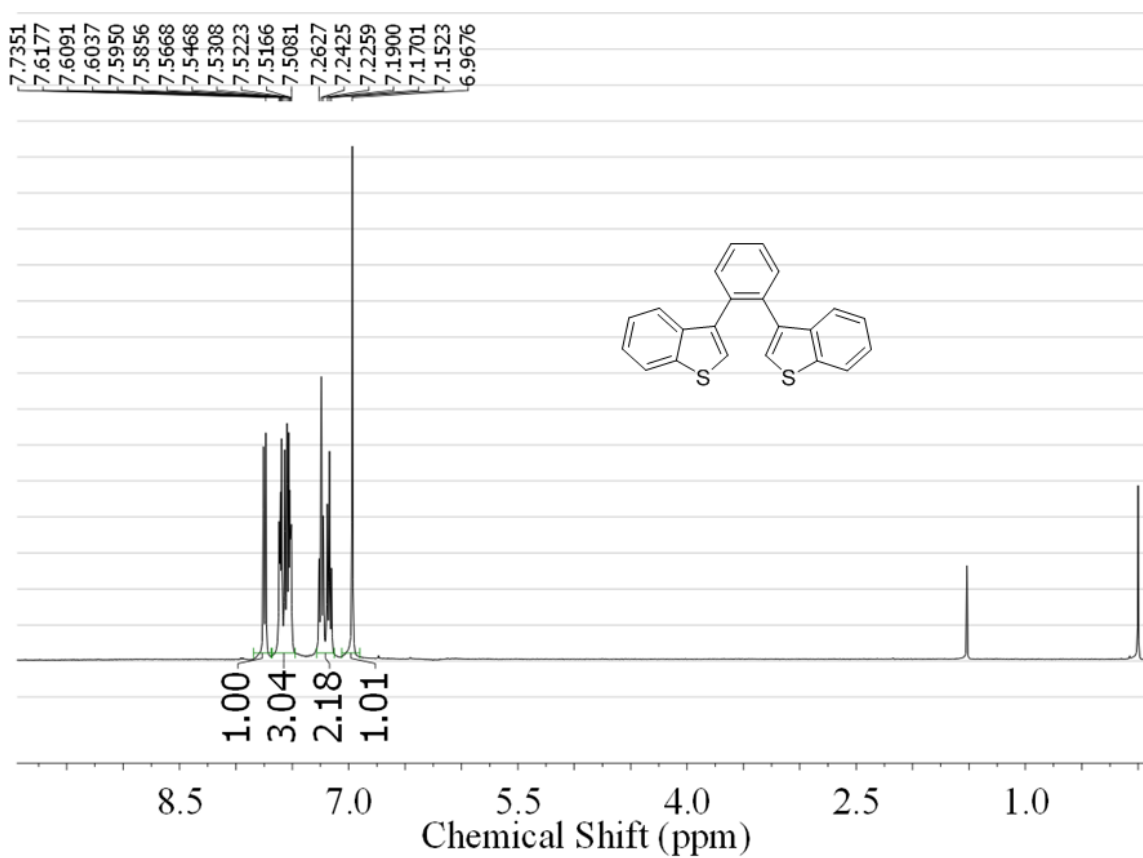
mL), and the combined organics were washed with H₂O (3 x 15 mL) and brine (1 x 15 mL). The organic layer was dried with MgSO₄, filtered, and concentrated under reduced pressure. Hexanes (10 mL) was added to precipitate the product. The light brown solid was collected and washed with hexanes to afford the pure product (0.22 g, 56%). M.p. = 136-138 °C. ¹H NMR (300 MHz, CDCl₃): δ (ppm) 8.71 (2H, s), 7.94 (2H, d, *J* = 7.2 Hz), 7.83 (2H, d, *J* = 7.2 Hz), 7.27-7.34 (6H, m). ¹³C NMR (300 MHz, CDCl₃): δ (ppm) 149.1, 142.0, 139.8, 137.5, 137.1, 133.5, 128.3, 124.5, 123.0, 122.4. IR (neat) ν 1427 cm⁻¹. Elemental analysis calculated for C₂₀H₁₂N₂S₂: C, 69.74, H, 3.51, N, 8.13%. Found: C, 69.41, H, 3.85, N, 7.89%.

Naphtho[2,1-b:3,4-b']bis[1]benzothiophene (DTNN). To a dry round bottom flask was added compound **1** (0.10 g, 0.29 mmol) with 8 mL THF. The solution was cooled to -78 °C, and *n*-BuLi (2.5 M in hexanes, 0.30 mL, 0.73 mmol) was added dropwise via syringe. The reaction was stirred at -78 °C for 10 min, then warmed to rt and stirred for 1.5 hr. CuCl₂ (0.20 g, 1.46 mmol) was added in one portion, and the reaction was allowed to stir for 1.5 hr. The precipitate was collected on a Buchner funnel and washed with methanol to afford the pure product as a white solid (0.034 g, 34%). M.p. = 272 °C. ¹H NMR (500 MHz, C₂D₂Cl₄, 80 °C): δ (ppm) 8.58 (2H, s), 8.28 (2H, d, *J* = 7.9 Hz), 7.45 (2H, d, *J* = 7.6 Hz), 7.22 (2H, s), 7.05 (2H, t, *J* = 6.7 Hz), 6.94 (2H, t, *J* = 6.9 Hz). IR (neat) ν 1510 cm⁻¹. Elemental analysis calculated for C₂₂H₁₂S₂: C, 77.61, H, 3.55%. Found: C, 77.31, 3.52%.

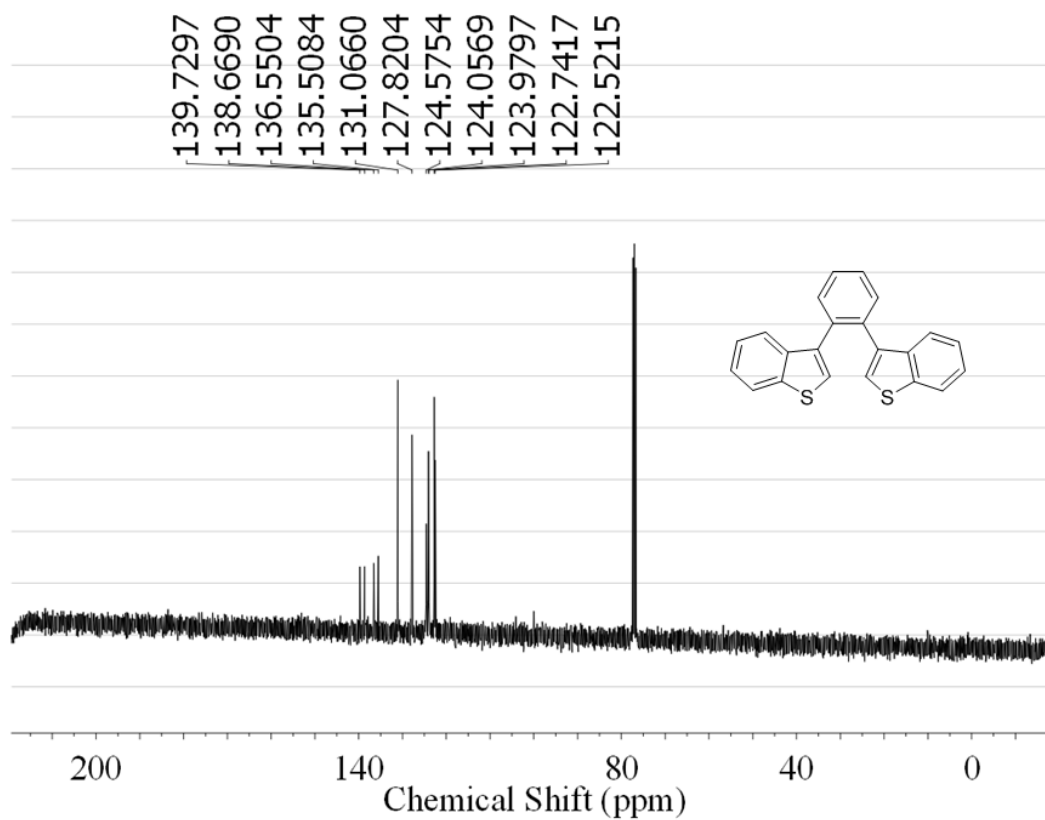
Quinoxalo[6,5-b:7,8-b']bis[1]benzothiophene (DTNQ). To a test tube was added compound **2** (0.52 g, 1.52 mmol), I₂ (0.05 g, 0.20 mmol) and toluene (250 mL). Air was bubbled through the mixture while the reaction was irradiated by a 200 W mercury lamp for 12 hr. The reaction was then poured into a separatory funnel and washed with sat. Na₂S₂O₃ (aq.) (3 x 50 mL). The toluene layer was then dried with MgSO₄, filtered, and

concentrated to 20 mL. The solution was then cooled to 0 °C, the precipitate was collected and washed with methanol to afford the pure product as a yellow solid (0.26 g, 51%). Additional purification could be achieved via sublimation. M.p. = 296 °C. ¹H NMR (500 MHz, C₂D₂Cl₄, 80 °C): δ (ppm) 9.12 (2H, d, *J* = 8.2 Hz), 8.49 (2H, s), 7.43 (2H, d, *J* = 8.0 Hz), 7.07 (2H, t, *J* = 8.1 Hz), 6.98 (2H, t, *J* = 8.0 Hz). IR (neat) ν 1489 cm⁻¹. Elemental analysis calculated for C₂₂H₁₀N₂S₂: C, 70.15, H, 2.94, N, 8.18%. Found: C, 69.82, H, 3.02, N, 8.08%.

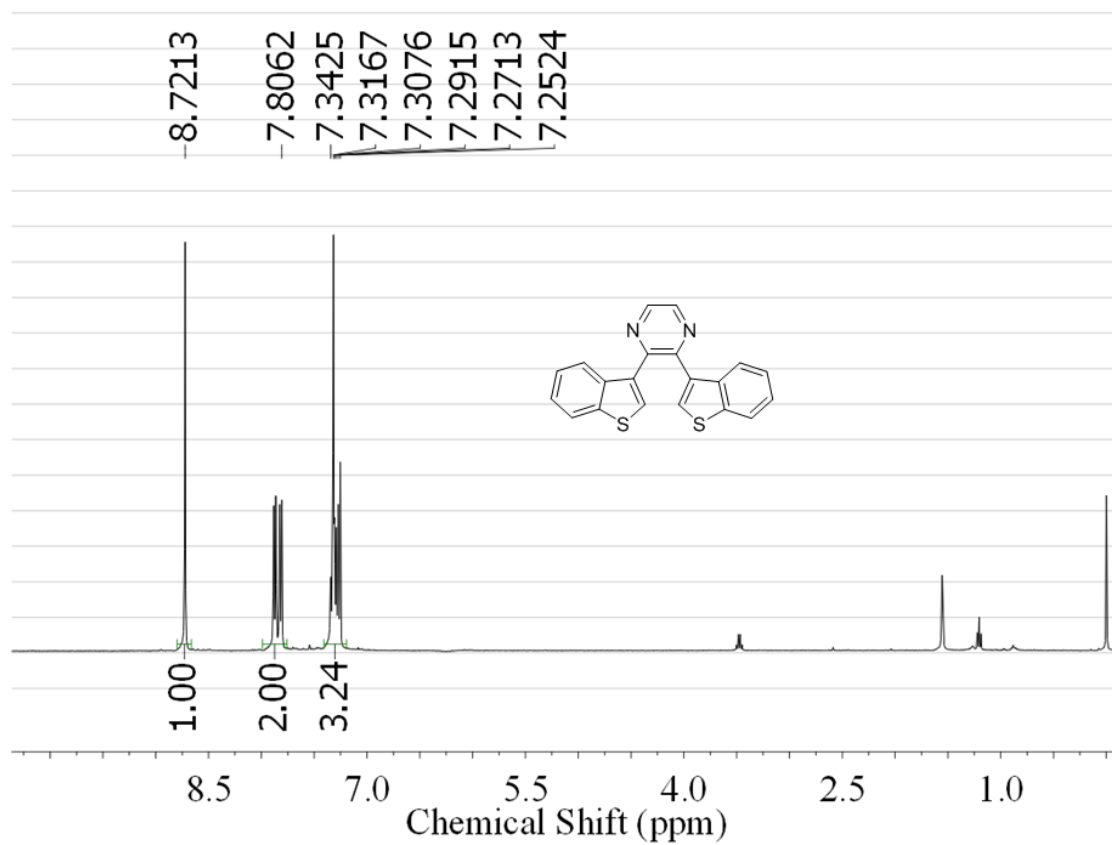
Appendix



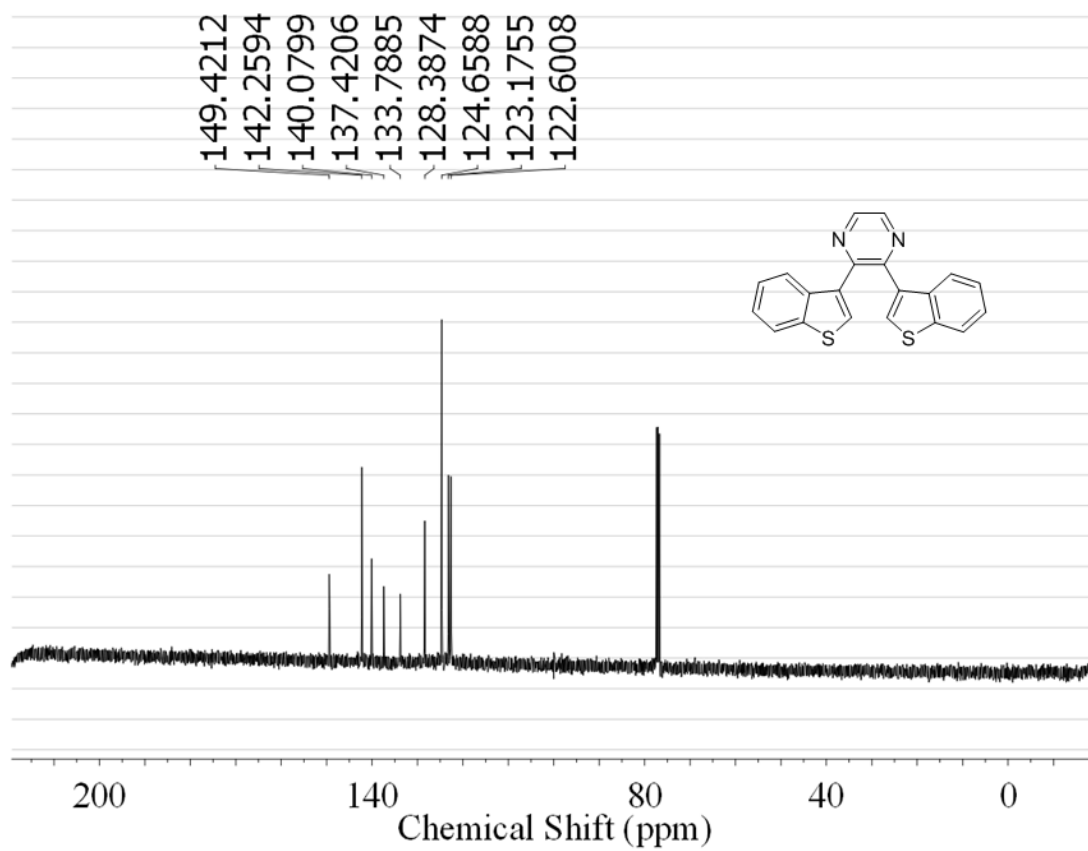
¹H NMR Spectrum of precursor to DTNN (300 MHz, CDCl₃)



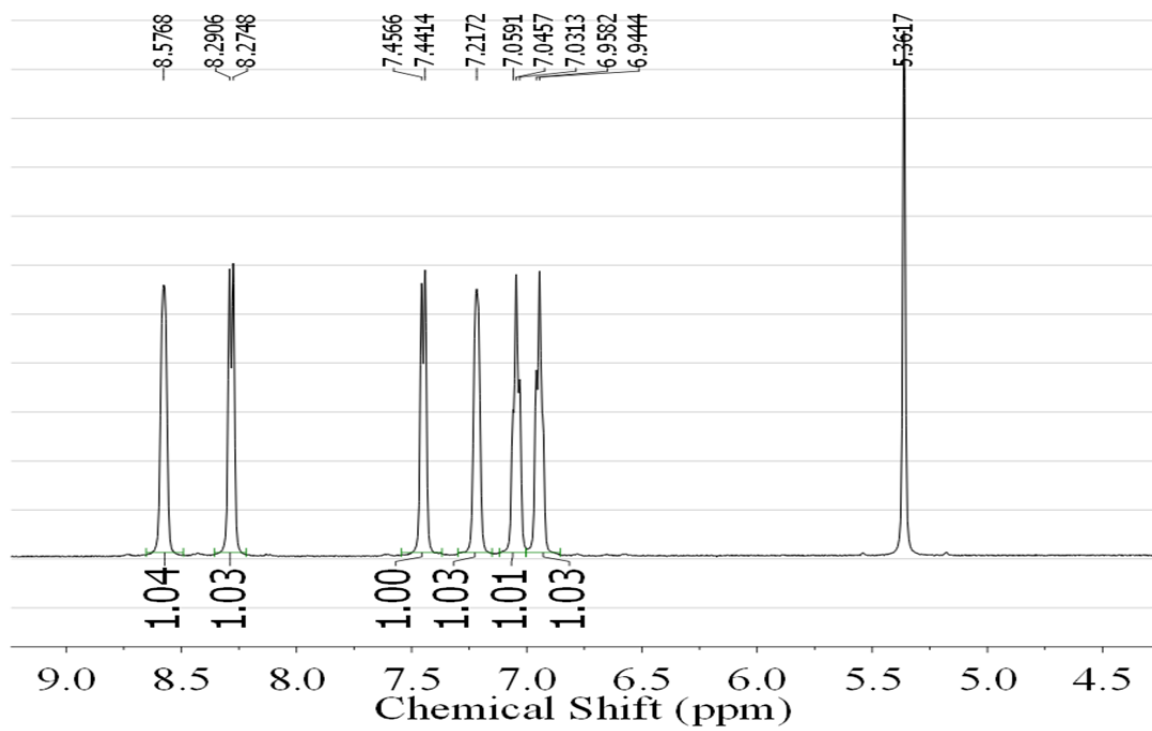
^{13}C NMR Spectrum of precursor to DTNN (300 MHz, CDCl_3)



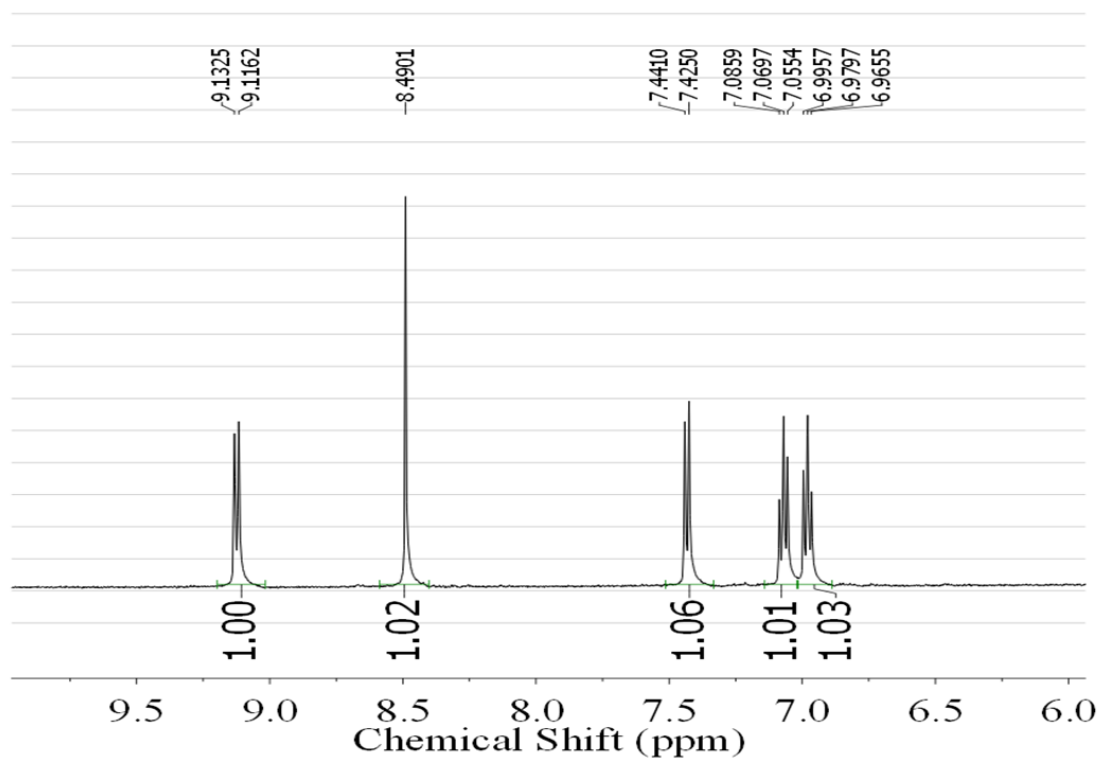
^1H NMR Spectrum of precursor to DTNQ (300 MHz, CDCl_3)



¹³C NMR Spectrum of precursor to DTNQ (300 MHz, CDCl₃)



¹H NMR of **DTNN** (C₂D₂Cl₄, 80 °C)



¹H NMR of **DTNQ** (C₂D₂Cl₄, 80 °C)

References

- 1) Jurchescu, O. D.; Baas, J.; Palstra, T. T. M. *Appl. Phys. Lett.* **2004**, 84, 3061
- 2) Hasegawa, T.; Takeya, J. *Sci. technol. Adv. Mater.* **2009**, 10, 024314
- 3) Takimiya, K.; Ebata, H.; Sakamoto, K.; Izawa, T.; Otsubo, T.; Kunugi, Y. *J. Am. Chem. Soc.* **2009**, 128, 12604
- 4) Ebata, H.; Izawa, T.; Miyazaki, E.; Takimiya, K.; Ikeda, M.; Kuwabara, H.; Yui, T. *J. Am. Chem. Soc.* **2007**, 129, 15732
- 5) Yamamoto, T.; Takimiya, K. *J. Am. Chem. Soc.* **2007**, 129, 2224
- 6) Shinamura, S.; Osaka, I.; Miyazaki, E.; Nakao, A.; Yamagishi, M.; Takeya, J.; Takimiya, K. *J. Am. Chem. Soc.* **2011**, 133, 5024
- 7) Zschieschang, U.; Ante, F.; Yamamoto, T.; Takimiya, K.; Kuwabara, H.; Ikeda, M.; Sekitani, T.; Someya, T.; Kern, K.; Klauk, H. *Adv. Mater.* **2010**, 22, 982
- 8) Takimiya, K.; Shinamura, S.; Osaka, I.; Miyazaki, E. *Adv. Mater.* **2011**, doi: 10.1002/adma.201102007
- 9) Chang, Y.-C.; Chen, Y.-D.; Wen, Y.-S.; Lin, J.-T.; Chen, H.-Y.; Kuo, M.-Y.; Chao, I. *J. Org. Chem.* **2008**, 73, 4608
- 10) Li, R.; Dong, H.; Zhan, X.; He, Y.; Li, H.; Hu, W. *J. Mater. Chem.* **2010**, 20, 6014
- 11) Brusso, J. L.; Hirst, O. D.; Dadvand, A.; Ganesan, S.; Cicoira, F.; Robertson, C. M.; Oakley, R. T.; Rosei, F.; Perepichka, D. F. *Chem. Mater.* **2008**, 20, 2484
- 12) Tang, X.-Q.; Harvey, R. G. *J. Org. Chem.* 1995, 60, 3568
- 13) Gao, B.; Wang, M.; Cheng, Y.; Wang, L.; Jing, X.; Wang, F. *J. Am. Chem. Soc.* **2008**, 130, 8297
- 14) Richards, G. J.; Hill, J. P.; Subbaiyan, N. K.; D'Souza, F.; Karr, P. A.; Elsegood, M. R. J.; Teat, S. J.; Mori, T.; Ariga, K. *J. Org. Chem.* **2009**, 74, 8914
- 15) Nagao, I.; Shimizu, M.; Hiayama, T. *Angew. Chem. Int. Ed.* **2009**, 48, 7573
- 16) Chang, Y.-C.; Chen, Y.-D.; Wen, Y.-S.; Lin, J.-T.; Chen, H.-Y.; Kuo, M.-Y.; Chao, I. *J. Org. Chem.* **2008**, 73, 4608
- 17) Suresh, C. H.; Gadre, S.R. *J. Org. Chem.* **1999**, 64, 2505
- 18) Laquindanum, J. G.; Katz, H. E.; Lovinger, A. J. *J. Am. Chem. Soc.* **1998**, 120, 664
- 19) Izawa, T.; Miyazaki, E.; Takimiya, K. *Adv. Mater.* **2008**, 20, 3388
- 20) Heimel, G.; Romaner, L.; Zojer, E.; Brédas, J.-L. *Nano Lett.* **2007**, 7, 932
- 21) Bianchini, C.; Gatteschi, D.; Giambastiani, G.; Rios, I. G.; Lenco, A.; Laschi, F.; Mealli, C.; Meli, A.; Sorace, L.; Toti, A.; Vizza, F. *Organometallics* **2007**, 26, 726

CHAPTER 6

General Conclusions and Future Work

6.1 Conclusions

Control of the morphology in organic thin films is of significant interest for a variety of electronic applications including field-effect transistors. For example, reducing the effects of grain boundaries is known to significantly improve charge transport in semiconducting polymers.¹ The findings presented in chapters 2 and 3 demonstrate the utility of perfluoroalkyl chemistry for controlling material properties and ultimately manipulating thin film morphology. End-perfluoroalkylation of P3HT was not found to affect charge transport in thin films; however, the end-group resulted in unique self-assembly of the conjugated polymer. Supramolecular structures such as the vesicles observed for F-P3HT could potentially be used for constructing unique blend morphologies.

When perfluoroalkyl end-groups were incorporated onto the soluble octithiophene DFH-DD8T the perfluoro chains led to a mesophase that could be used for controlling film morphology. After annealing through the mesophase thin films of DFH-DD8T showed exceptional long range order. However, no field effect behavior was observed as a result of the perturbed molecular orbital energies. This finding demonstrates the interplay between the two primary effects that perfluoroalkyl substitution has on oligothiophene semiconductors: 1) fluorophilic intermolecular interactions and 2) reduction of the HOMO and LUMO energies. The latter effect was

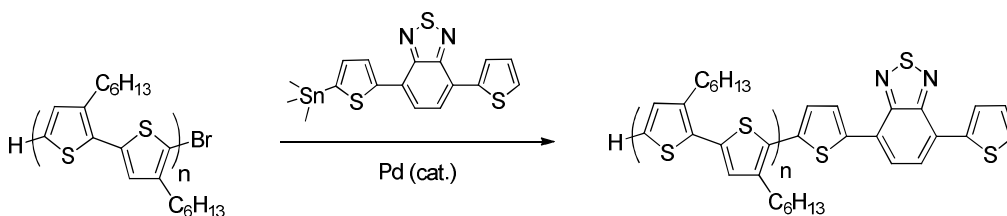
utilized in chapter 4 in order to explore materials with low lying LUMO levels for n-type transistors. The combination of σ -electron withdrawing perfluoroalkyl groups and the π -electron deficient benzothiadiazole unit effectively lowered the LUMO of compound DFH-4T-BTD to -3.42 eV, allowing for efficient electron injection from Au electrodes. However, further stabilization of the LUMO is necessary in order to observe air stable n-type OFETs. This remains a challenge for material scientists as only a handful of air stable n-type semiconductors are known today.

Discovering organic materials with higher charge mobilities is an ongoing pursuit and will likely be an area of research for many years. The charge mobility of the semiconductor within an OFET is a limiting factor for the switching speed of the device, and therefore limits the potential applications of OFETs. Recently there have been several reports of thin film transistors utilizing small molecule semiconductors with mobilities higher than 5 cm²/Vs.² Mobilities this high have mainly been achieved using highly crystalline thienoacene compounds which are paving the way for high performance p-type OFETs. The thienoacenes presented in chapter 5 showed exceptional π -stacking in the crystal structure and are therefore candidates for high performance OFETs. The mobilities that were determined for compounds DTNN and DTNQ were certainly far from record breaking; however, this is most likely a result of the non-ideal morphology that was observed for their thin films. This again demonstrates the importance of thin film morphology in organic devices. Interestingly, thienoacenes with low lying LUMO levels have not been pursued to date. Comparison between DTNN and DTNQ demonstrated the ability to significantly lower the LUMO of thienoacenes through incorporation of nitrogen containing heterocycles. This may be an effective strategy for the development of high performance n-type materials.

6.2 Future Work

Further experimentation with end-modified conjugated polymers could provide significant benefits within the field of organic photovoltaics. In addition to supramolecular p-n junctions such as that described in section 2.9, end-group modification could be a useful strategy for controlling the optical absorption of conjugated polymers without significantly affecting the charge transport properties.

In photovoltaic devices the power conversion efficiency is dependent on the I-V characteristics of the p-n junction under illumination. The maximum current density of the device will depend on the efficiency of exciton formation, exciton dissociation, and charge percolation. The conversion of incident light to excitons is crucial, and requires good overlap between the incident solar energy and the π - π^* transition of the p-type semiconductor. Furthermore, the charge mobility of the p-type semiconductor will affect hole collection at the anode. Therefore, the p-type semiconductor should have high hole mobility as well as good absorption overlap with the solar spectrum. Many conjugated polymers with high hole mobilities such as poly(3-hexylthiophene) and poly(2,5-bis(3-alkylthiophen-2-yl)thieno[3,2-*b*]thiophene) have poor overlap with the solar spectrum. An interesting method for improving the absorption properties of these and similar conjugated polymers is to conjugate a chromophore to the end of the polymer chain. For example, a benzothiadiazole end-group could be conjugated to the end of P3HT using the Stille coupling reaction presented in chapter 2 (scheme 6.1). This would likely induce a red-shift of the UV/vis absorption and improve the efficiency of exciton formation. Based off the OFET studies presented in chapter 2, it is not likely that the benzothiadiazole end group would significantly impact the hole mobility of P3HT. Therefore, this method would allow control over the absorption properties of P3HT while preserving the high hole mobility of the polymer.



Scheme 6.1 End-modification of P3HT with red-absorbing chromophore

In addition to these studies, other future work will focus on novel fused aromatic systems. The exceptional π - π stacking observed for the thienoacene compounds presented in chapter 5 indicates the potential for very high charge mobilities in related

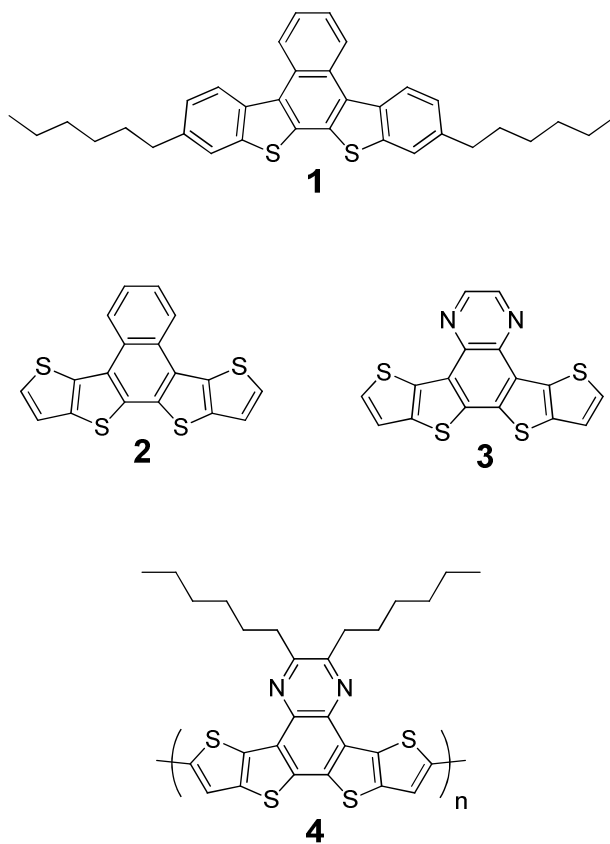


Figure 6.1 Alkylated analog of DTNN for improved solubility

systems. First, single-crystal transistors of DTNN and DTNQ are of interest in order to probe the intrinsic hole mobilities for these compounds. Afterward, new compounds that retain the same aromatic structure but incorporate alkyl chains for solubility are of interest. For example, compound **1** in Figure 6.1 shows an alkylated analog of DTNN which is expected to have improved solubility and could therefore be used for solution processable FET devices. In addition, substitution of the benzothiophene units in DTNN and DTNQ for thieno[3,2-*b*]thiophene rings could lead to interesting new semiconductors. Furthermore, the reactive two-positions of the exterior thiophene rings in compounds **2** and **3** could be utilized for further reactions including polymerization. For example, polymer **4** could be prepared from polymerization of the alkylated analog of **3**. This could be a useful strategy for low band-gap materials with good π - π stacking and high charge mobilities.

References

- 1) Zhang, X.; Hudson, S. D.; DeLongchamp, D. M.; Gundlach, D. J.; Heeney, M.; McCulloch, I. *Adv. Funct. Mater.* **2010**, 20, 4098
- 2) Takimiya, K.; Shinamura, S.; Osaka, I.; Miyazaki, E. *Adv. Mater.* **2011**, 23, 4347